Université du Québec
Institut National de la Recherche Scientifique
Énergie Matériaux Télécommunications

Denoising Amplification of Arbitrary Coherent Signals Using the Talbot Effect

Par

Benjamin Crockett

Mémoire présenté pour l'obtention du grade de
Maître en Sciences, M.Sc.
en Sciences de l'énergie et des matériaux

Jury d'évaluation

Examinateur externe	Hossein Asghari Loyola Marymount University
Examinateur interne	François Légaré Insitut National de la Recherche Scientifique
Codirecteur de recherche	Andreas Peter Ruediger Insitut National de la Recherche Scientifique
Directeur de recherche	José Azaña Insitut National de la Recherche Scientifique

©Benjamin Crockett, 2019

Remerciements

It is quite remarkable how unpredictable life may be sometimes. During my undergraduate studies in Physics, I could not have foreseen that I would turn out pursuing a Master's degree in optical signal processing, particularly with such an important aspect of my work relating to telecommunications. However, I simply went for the things that inspired me and for what I enjoyed most, and I am now deeply grateful for everything that has happened, leading me to work in this exciting and dynamic field. As it may often happens in science, my adventure all started by a simple "hmm, that's neat!" as a reaction to a presentation on the Talbot effect by Dr. Reza Maram, who was a PhD student with Prof. José Azaña at the time. Little did I know back then how this event would impact my life and career. And now, here I stand, pursuing work I like to describe as "Making music with light," merging both my passions for science and music into my daily work. There are many people who contributed to this project in different ways; here I do a modest attempt to recognize some of them who helped me achieve the work presented here– without whom none of this would have been possible.

First, I would like to give my sincere gratitude to my supervisor, Prof. José Azaña, for his support and guidance throughout my degree. His ability to encourage me to find new ways to tackle a problem and to challenge my understanding has shaped me to become the researcher I am today. I always appreciated his genuine consideration for the various ideas I would bring. These are qualities I will continue to cultivate both professionally and personally. I am also grateful to my co-supervisor, Prof. Andreas Ruediger, for accepting me as a master's candidate for the challenging problem I first proposed. Our fruitful discussions about condensed matter, academia, and the industry gave me a new perspective on working with science. I would like to thank Dr. Maurizio Burla for giving me the chance to work in the ultrafast optical processing group at INRS as an undergraduate intern in the first place, opening the door for me towards this exciting field. I am glad we have kept in touch, and it is always a great pleasure to meet him in various conferences around the world. I would also like to thank Dr. Reza Maram for inspiring me with interesting work in the field of the temporal Talbot effect that motivated me to join this group for my master's degree. Furthermore, I want to thank the examiners Prof. Hossein Asghari from Loyola Marymount University and Prof. François Légaré from INRS for taking the time to review this thesis and giving insightful feedbacks. I also thank the Fond de Recherche du Québec - Nature et Technologies for Financial support, along with Mehdi Chbihi from Keysight and Richard Duhamel from Tektronix for lending part of the equipment used in the experiments.

I am deeply indebted to my friend and colleague Dr. Luis Romero Cortés for his essential support through my master's degree. Without his generous help and guidance, this project would not have been able to grow as much as it did. Teaching the rudiments of experimental work in optical signal processing is not an easy task, yet he proved to be a great mentor, even at a distance. I also want to thank the other members of the UOP group for the nice moments we have shared together, both inside and outside of the lab; Saikrishna Reddy Konatham, Dr. Daniel Onori, Saket Kaushal, Xinyi Zhu, Dr. Jeonghyun Huh, Dr. Xiao-Zhou Li, Dr. Mohamed Seghilani and Dr. Hamed Pishvai Bazargani. I want to thank Prof. James van Howe from Augustana College for insightful discussions that contributed towards me continuing my research at the PhD level. I also want to give special thanks to Robin Helsten for his assistance in the lab that helped me build confidence for performing the various experiments shown in this thesis.

De plus, je dois un remerciement spécial à tout mon entourage pour leur support au cours de ces années. Ceci inclut tous mes amis, dont j'ai le plaisir de continuer à côtoyer, malgré que nous aimerions se voir plus souvent, comme c'était dans le temps!

Je remercie aussi ma soeur Élise Crockett pour sa présence et les moments simples que l'on passe ensemble, ainsi que pour son aide à entretenir notre chère site web.

Je tiens à remercier Irina Segovia, avec qui j'ai le plaisir de partager ma vie. Son amour et son support soutenu au cours de ces années m'ont aidés à passer à travers les bons et moins bons moments. Ce fut un plaisir de travailler, rire et aimer à ses côtés, de façon à rendre chaque moments de mes études plus agréables.

Finalement, je dois une reconnaissance inestimable pour mes parents, France Brabant et John Crockett, pour leurs encouragements sans limites au travers de mes études, ainsi que pour leur support inébranlable. Ils ont su stimuler ma curiosité dès mon jeune âge, formant ainsi l'esprit scientifique que j'ai développé au fil du temps. C'est en grande partie grâce à leur amour et leur motivation que j'ai pu en arriver où je suis.

Résumé

L'optique et la photonique ont été au coeur d'une panoplie d'avancements scientifiques et technologiques depuis quelques décennies. En particulier depuis l'avénement du laser, des approches basées sur l'optique ont été capitales au déploiement d'une multitudes d'applications, notamment en spectroscopie, imagerie, métrologie, télécommunication, pour le traitement d'informations, etc.. Malgré le progrès formidable des technologies photoniques, certains développements névralgiques dans ces divers domaines demandent une sensibilité et une tolérance au bruit accrues afin de pouvoir fructueusement extraire l'information requise d'un signal optique donné. Le problème est d'autant plus important lorsque le signal d'intérêt est faible, car dans ce cas, de l'énergie externe est habituellement injectée afin que la forme d'onde atteigne suffisamment de puissance pour être détectée. Cependant, toute forme d'amplification dégrade nécessairement la qualité d'un signal, de sorte qu'il est possible que la forme d'onde soit corrompue par le bruit à un point tel que l'information contenue soit totalement perdue.

En fait, le problème du bruit est omniprésent, car pratiquement tous les signaux requièrent une forme ou une autre d'atténuation de bruit due à l'intrusion inévitable de bruit qui peut affecter les différents procédés d'un mécanisme de traitement de signal, soit dès lors qu'un signal est généré, durant sa propagation, où au moment de la détection. La méthode la plus répandue pour atténuer le bruit est d'utiliser un filtre de bande passante, qui élimine toute l'énergie à l'extérieur d'une plage de fréquences données. Néanmoins, cette approche est mal adapté aux signaux qui consiste en une gamme de fréquences très restreintes, ainsi que ceux qui consiste en une gamme très large de fréquences. En particulier, les signaux à bande étroite sont difficiles à traiter car il est complexe de concevoir un filtre optique efficace avec une bande passante très étroite, tout en maintenant une perte d'insertion basse. D'autre part, l'atténuation du bruit par filtre à bande passante est inefficace pour traiter les signaux à large bande, car une quantité importante du bruit est contenue à même la bande du signal. Des méthodes alternatives afin de contrer ce bruit interbande sont très rares, et sont le sujet de recherches actives depuis longtemps. Les quelques solutions existantes se basent sur des post-traitements digitales qui ne peuvent pas être appliquées aux signaux optiques.

Ce mémoire présente la nouvelle solution que j'ai développée pour le rétablissement de signaux optiques noyés sous le bruit. Le concept est basé sur la théorie de l'effet Talbot, et consiste à redistribuer l'énergie d'un signal en une série de pointes dont l'enveloppe suit une forme amplifiée du signal initial. Ce procédé est physiquement implanté exclusivement par des manipulations de phases, afin de réaliser un échantillonnage sans perte menant à une amplification sans bruit du signal. La méthode proposée offre le rétablissement du signal en temps réel et à la volée, sans avoir recours à un post-traitement digital, agissant directement sur le support physique de l'onde. Elle peut être instaurée soit pour les signaux à bande étroite ou à large bande, visant les problèmes mentionnés quant à l'atténuation de bruit pour chaque type de signal. Le concept apporte donc une approche opportune et universelle pour la détection de signaux considérablement différents, qui pourrait permettre le rétablissement d'information précédemment inaccessible, accordant potentiellement de nouvelles avancées pour des domaines variant de la radioastronomie, aux télécommunications, et à la biologie.

Mots-clés: Atténuation du bruit, Détection de signaux faibles, Amplification sans bruit, Effet Talbot.

Abstract

Optics and photonics have been at the heart of a plethora of scientific and technological advancements in the last decades. Particularly since the advent of the laser, optical approaches have been key to numerous scientific and technological applications, namely in spectroscopy, imaging, metrology, telecommunication, and information processing, amongst many others. Despite tremendous advancements in photonic technologies, successful key applications in these diverse fields require higher sensitivity and tolerance against noise to be able to extract the needed information from a given optical signal. This is particularly problematic when the waveform of interest is weak, since in this case, energy is typically injected in the signal in order for it to have sufficient power to be detected, but any form of active amplification will necessarily degrade the quality of a signal, in such a way that the information can get completely corrupted by noise in the amplification process.

In fact, the problem of noise is ubiquitous, as practically all signals require some form of noise mitigation due the unavoidable intrusion of noise that can affect a signal processing scheme, which may happen when the signal is generated, during its propagation or at the time of detection. The most common method to mitigate noise is to use a bandpass filter, which eliminates all the energy outside of a given bandwidth. However, this approach is ill-suited for signals which consists of a very narrow band of frequency components as well as those that consist of a very broad range of frequency components. In particular, narrowband optical signals are difficult to process because it is difficult to design effective optical filters with very narrow pass bands and low loss. On the other hand, noise mitigation by bandpass filtering is ineffective for broadband signals since a large amount of noise is contained within the bandwidth of the signal itself, and as such, is unaffected by bandpass filtering. Alternative methods to mitigate this so-called in-band noise are scarce and have been the subject of much research these past decades. Current solutions typical relying on digital post processing methods that are ill-suited for broadband optical signals.

In this thesis, I present a novel solution I developed for the recovery of optical signals buried under noise. The concept is based on the theory of the Talbot effect, and consist of redistributing the energy of the signal into discrete bins using phase-only manipulations, simultaneously implementing lossless sampling and noiseless amplification of the signal. The proposed method provides signal recovery on the fly and in real-time, directly on the physical wave domain, thus avoiding the need for digitalization and post-processing. It can be implemented for either narrowband or broadband signals, targeting the aforementioned difficulties in noise reduction associated with each kind of signals. It thus brings a timely, universal approach for the detection of vastly different signals, and could enable the recovery of previously unattainable information, allowing for new advances in fields ranging from radio-astronomy to telecommunications and biology.

Keywords: Noise mitigation, Weak signal detection, Noiseless amplification, Talbot effect.

Sommaire Récapitulatif

Cette section fournit un bref résumé des motivations de ce projet de maitrise. Ceci vise à introduire l'importance des recherches effectuées sur le développement de nouvelles techniques pour la détection d'ondes optiques à faible énergie, noyées sous une quantité de bruit qui rend leur détection difficile. Le problème de la détection d'onde optique est traité, ainsi que les solutions actuelles et les problèmes qui y sont associés. Ceci est suivi d'une présentation des concepts utilisés pour le déploiement d'une technique novatrice afin de répondre aux problèmes soulevés. Ce résumé termine avec la présentation de résultats expérimentaux ainsi que d'une brève conclusion décrivant les avantages des techniques proposées.

0.1 Procédés d'amplification et d'atténuation de bruit en optique

Toute connaissance que nous obtenons provient ultimement d'une mesure du monde extérieur. Ce processus de mesure consiste généralement à transférer l'information d'un système à l'un que nous pouvons consciemment interpréter. Veuillez noter qu'ici, le therme information ne se limite pas simplement à son usage habituel dans le domaine de la télécommunication ou de l'informatique, mais réfère plutôt à la description d'une entité dans le sens général du terme. Cette information pourrait donc être quelque chose d'aussi anodin que la distance entre deux villes, la couleur d'une feuille d'automne, la vitesse à laquelle un véhicule se déplace, ou encore la signification de mots énoncés. En revanche, l'obtention de certaines connaissances requiert parfois des instruments hautement sophistiqués afin d'accéder à l'information désirée. Par exemple, on envoi dans l'espace des satellites pour mesurer une radiation provenant de la formation de notre univers, le rayonnement de fond cosmologique (*Cosmic Microwave Background*, CMB). Le CMB est alors détecté avec un niveau de bruit extrêmement bas et une sensibilité à la fine pointe de la technologie par des antennes hautement spécialisées [sr1]. Il existe évidement une myriade d'entités qui doivent être mesurée de diverses façons. Cette composante expérimentale pour accéder à l'information est centrale à l'avancement de la science.

Dans virtuellement tous les cas, l'information est supportée par une forme de système d'onde, habituellement d'origine mécanique ou électro-magnétique. De plus, le processus de mesure ne consiste habituellement pas seulement que de l'étape de la détection; la forme d'onde contenant l'information d'intérêt doit habituellement propager de l'entité sous investigation jusqu'à l'appareil de détection, et dans certain cas, l'onde elle-même doit être générée extérieurement afin de sonder l'entité sous investigation. Le domaine de l'optique et de la photonique, qui concerne la manipulation et le traitement d'onde électro-magnétique dans les régimes visuels, ultraviolet et infrarouge, est particulièrement bien adapté pour les systèmes de mesures. Plusieurs raisons expliquent cela, telles que la sensibilité unique offerte par ce médium pour sonder divers entités d'une façon non-intrusive, ainsi que son habilité à transmettre de l'information sur de longues distances. En effet, les approches basées sur la photonique permettent de mesurer une foule de phénomènes scientifiques, de l'investigation du très grand, tel que des événements astronomiques ayant lieu à des années lumières de la terre [sr2], jusqu'au microscopique, pour sonder les dynamiques de réactions chimiques et biologiques [sr3]. La photonique est aussi centrale à l'avénement d'une myriade de développements technologiques, par exemple en permettant la transmission massive de données par l'internet, possible par la haute capacité d'information de la fibre optique [sr4]. Ou encore, par les avancements en imagerie qui permettent une qualité photographique phénoménale aux caméras de téléphones portables. Les progrès en photonique ont certainement eu un impact immense sur l'humanité, non seulement d'un point de vue scientifique, mais aussi technologique et social. Cependant, il y a un problème central à tout processus de mesure qui affecte aussi les applications potentielles des approches optiques, notamment l'enjeu omniprésent du bruit.

Dans le domaine du traitement de signal, le bruit est définit un peu différemment de son usage habituel dans la vie de tous les jours, ou le terme peut référer au son produit par un moteur de voiture, ou encore celui provenant d'un champ de construction. Plusieurs définitions ont été proposées, mais dans le contexte d'une mesure, le bruit peut généralement être défini comme une perturbation stochastique indésirable qui tend à obstruer la communication ou la mesure d'un autre signal [sr5]. Dans la présente thèse, le terme est donc réservé à la partie indésirable d'un signal qui est de nature stochastique, non corrélé, et caractérisé par des fluctuations rapides. Notez que le fait d'être aléatoire n'est pas un critère en soit pour qu'un signal soit du bruit. En effet, si l'on prend par exemple un signal de télécommunication portant de l'information encodée sous forme de bits, du point de vue d'un observateur externe, ce signal varie de façon aléatoire. Pourtant nous serions tous d'accord pour dire que ce signal ne correspond pas à ce que nous appellerions du bruit. Effectivement, la nature imprévisible du bruit est souvent plutôt d'origine physique, tel que l'agitation thermique des électrons dans un courant électrique à faible intensité, ou le temps d'arrivée aléatoire de particules individuelles qui donne lieu au bruit de grenaille (*shot noise*). En revanche, dans certaines disciplines, tout signal indésirable peut être considéré comme du bruit, sans regard vis-à-vis d'un critère stochastique. Par exemple, deux canaux de communication peuvent causer de l'inter-modulation (*cross-talk*), de sorte qu'un signal indésirable s'ajoute à un canal adjacent par couplage parasitique. Sans perte de généralité, ce type de distorsion ne sera pas inclus dans notre définition de bruit. Nous réservons donc ce terme pour des signaux indésirables qui sont incohérents et de nature stochastique, comportant de rapides fluctuations en amplitude et en phase de façon totalement imprévisible.

Bien que l'optique et la photonique offrent des avantages déterminants par rapport à d'autres approches pour prendre des mesures, ainsi que pour la transmission et le traitement d'information, la présence de bruit incohérent limite leur sensibilité pour mesurer des phénomènes dans plusieurs domaines différents, tel qu'en biologie [sr6], en physique fondamentale [sr7] et en chimie [sr8]. Cette problématique limite aussi la distance de rendement des liens de transmission d'information [sr9], ainsi que de l'implantation de la communication satellite optique [sr10], donnant lieu à de vastes recherches dans les récentes décennies. Le développement de nouvelles méthodes pour subvenir aux problèmes relatifs au bruit est donc le point central de cette thèse, orienté particulièrement au domaine de l'optique et de la photonique due à leur importance en science et technologie moderne.

L'enjeu du bruit est particulièrement sérieux dans le cas où le signal d'intérêt est de basse énergie. Si un signal optique est faible, il est typiquement amplifié en y injectant de l'énergie externe. Par contre, les mécanismes d'amplification active n'agissent pas seulement sur le signal d'intérêt, mais aussi sur tous signaux indésirables, tel que le bruit, contenu dans un champ électro-magnétique donné. De plus, tout amplificateur linéaire, qui est un amplificateur dont le signal de sortie est linéairement relié à celui d'entrée, va injecter un montant supplémentaire de bruit dans le signal, due à des lois fondamentales de la physique quantique [sr11]. Le travail pionnier de Carlton M. Caves sur le sujet a démontré que ce type d'amplificateur, qui inclus les amplificateurs à fibre dopée à l'erbium (*Erbium-Doped Fiber Amplifier*, EDFA) et les amplificateurs paramétriques insensibles à la phase (*Phase-Insensitive Parametric Amplifiers*, PIA) vont nécessairement dégrader le ratio de signal sur bruit (*Signal-to-Noise Ratio*, SNR) par 3 dB [sr12]. Le fait qu'un tel amplificateur dégrade le SNR d'un signal donné est relié au théorème de non-clonage de la physique quantique, qui peut heuristiquement être expliqué par le fait qu'il est impossible de parfaitement répliquer un état quantique sans violer le principe d'incertitude. Un effort important a été effectué ces dernières années vers la conception d'un amplificateur sans bruit, qui n'injecterait donc pas de bruit supplémentaire dans le système. En principe, ce serait possible de concevoir un tel amplificateur qui agirait de façon non-déterministe [sr13]. De tels amplificateurs ont bel et bien été démontrés, mais ils atteignent un niveau d'amplification très bas et ne sont pas adaptés pour une implantation pratique à l'extérieur de certaines applications nichées en optique quantique. D'autre part, la recherche vers l'amplification sans bruit basée sur les amplificateurs paramétriques sensibles à la phase (*Phase-Sensitive Amplifiers*, PSA) s'est grandement améliorée au courant des dernières années, avec une dégradation du SNR de seulement 1.1 dB démontrée récemment [sr14]. Cependant, de tels amplificateurs ne sont pas bien adaptés pour l'amplification de signaux en général, particulièrement pour le cas des signaux de télécommunication qui emploient une modulation complexe. De plus, ils demeurent difficiles à implanter dans un contexte pratique, et ultimement, même un PSA qui serait en mesure de ne pas détériorer le SNR amplifierait tout de même le bruit déjà contenu dans un signal, de sorte que des méthodes d'atténuation de bruit demeurent nécessaires. En général, la méthode appropriée pour éliminer le bruit dépend de la nature du signal, qui peut être catégorisé en fonction de l'étendue des fréquences de leur représentation spectrale, soit à bande étroite ou à large bande.

Les signaux qui consistent en une plage de fréquences restreintee δ_{ν_0} sont décrits comme étant de bande étroite (voir Fig. 1), et sont caractérisés par une variation lente dans le temps qui s'étend sur une longue durée temporelle. D'autre part, les signaux qui varient rapidement dans le temps auront une représentation spectrale donnée par une très large gamme de fréquences, et sont donc appelés signaux à large bande (voir Fig. 1). La transition entre ces deux régimes dépend naturellement du champ spécifique (onde acoustique, radio, micro-onde, etc.). Heuristiquement, dans le cas des ondes optiques, des signaux avec une gamme de fréquence moindre à 10 GHz seraient considérés comme bande étroite, tandis que des signaux avec une gamme de fréquence supérieure à 50 GHz serait considérés large bande; ceux entre ces deux régions seraient dans un régime intermédiaire.

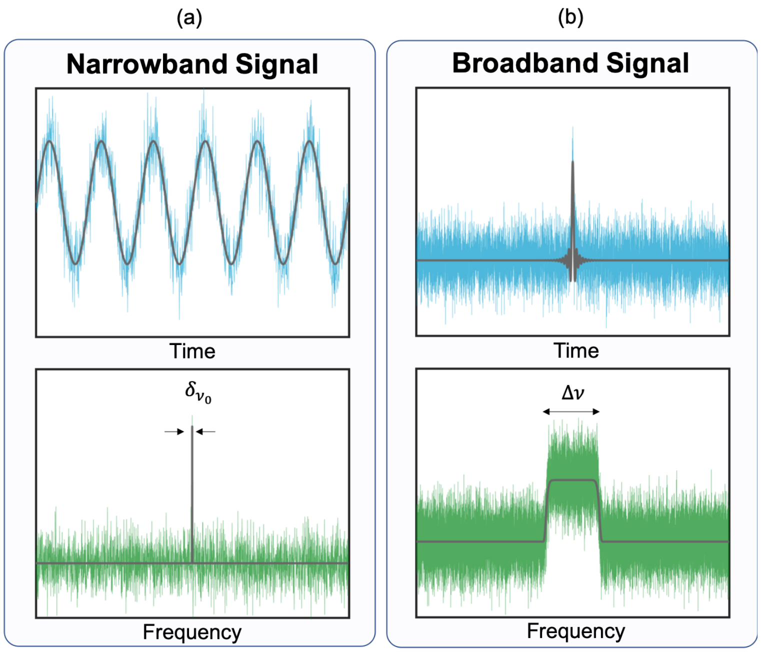

Fig. 1 – Défis reliés à l'atténuation du bruit pour les signaux à bande étroite et à large bande. (a) Les signaux à bande étroite consistent en un mince étendu de fréquences δ_{ν_0}. Il est compliqué d'atténuer le bruit contenue dans ces signaux efficacement car il est difficile de manipuler un signal optique avec une résolution spectrale très fine, en déça de 5-10 GHz. (b) En revanche, les signaux à large bande consistent en un vaste étendu de fréquences Δ_ν, de sorte qu'une grande quantité de bruit est contenu à même la bande de fréquence du signal. Ce bruit inter-bande est très complexe à atténuer sans causer de distorsions au signal d'intérêt, et est un sujet de recherche actif depuis de nombreuses années.

Les signaux optiques à bande étroite sont utilisés dans plusieurs domaines, particulièrement pour interagir avec des systèmes plus lent, qui comprennent habituellement des procédés basés sur des fonctions électroniques ou mécaniques. Par exemple, ils sont utilisés pour traiter et transmettre des signaux de données destinés à interagir avec des composantes électroniques, tel que des canaux micro-ondes et radios. Les signaux de type onde continue (*Continuous Wave*, CW) sont aussi considérés comme étant des signaux à bande étroite, et sont souvent utilisés dans des structures interférométriques pour mesurer de petites différences dans la longueur du trajet optique. Ils sont utilisés par exemple en surveillance d'intégrité structurelle mécanique ou pour la détection d'ondes gravitationnelles, parmi plusieurs autres champs d'applications. Afin d'atténuer le bruit de tels signaux, l'approche la plus commune est d'atténuer toutes les composantes spectrales en dehors de la gamme de fréquences du signal d'intérêt en utilisant un filtre optique [sr15]. Dans le domaine optique, des instruments communément utilisés inclus les réseaux de diffraction Bragg en fibre (*Fiber Bragg Grating*, FBG), les cavités Fabry-Perot et les cavités en anneaux. Quoique ces techniques ont démontré des performances remarquables au courant des dernières années, il demeure difficile de concevoir des filtres optiques avec des bandes passantes sous l'ordre des quelques GHz. En effet, il est généralement complexe de manipuler un signal optique avec une grande résolution spectrale tout en maintenant une perte d'insertion basse, de sorte que les filtres à bande étroite de haute performance disponible commercialement ont généralement une bande passante d'au moins 5 GHz. Quoi qu'il en soit, même si un filtre avec une bande passante ultra-étroite est bel et bien conçu, un autre problème se présentera alors; celui de s'assurer que le filtre reste bien aligné avec la fréquence centrale du signal. Effectivement, une forme de stabilisation est alors requise afin de garantir que le signal ne dérive pas à l'extérieur de la bande passante du filtre, ce qui mènera à une distorsion ou même une perte totale du signal d'intérêt. Récemment, des solutions basées sur l'effet non linéaire de l'éparpillement stimulé de Brillouin (*Stimulated Brillouin Scattering*, SBS) ont été proposées, et suivent intrinsèquement la fréquence centrale du signal d'intérêt avec une bande passante effective de l'ordre des MHz [sr16]. Par contre, cette approche nécessite un accès privilégié au signal porteur, ce qui limite grandement son application générale pour des signaux de sources inconnues.

De l'autre côté, les signaux à large bande sont accompagnés d'une collection de défis qui leur sont propres. Ces signaux sont communément utilisés pour les mesures temporelles à haute résolution, par exemple pour l'imagerie de la lumière en vol, ainsi que pour examiner les procédés ultra-rapides qui prennent place dans les réactions chimiques et biologiques. Les signaux à large bande sont aussi essentiels pour la télécommunication à haut débit, en radioastronomie, et aussi pour sonder les tissus biologiques. Pour atténuer le bruit dans de tels signaux, un filtre peut évidemment être employé pour éliminer le bruit à l'extérieur de la bande du signal. Par contre, le problème principal pour de tels signaux est qu'une grande quantité de bruit est contenue à même la bande du signal. Ce bruit interbande est en fait très difficile à atténuer sans affecter le signal d'intérêt, et est le sujet de recherches approfondies depuis de nombreuses années. Les solutions proposées sont rares, et se basent souvent sur des procédés de post-traitements digitaux. Plusieurs approches de ce genre ont été développées par des chercheurs dans le domaine du traitement de signaux d'électroencéphalogramme (EEG) [sr17], en reconnaissance vocale [sr18], dans le traitement d'image [sr19], ainsi qu'en surveillance de santé structurelle mécanique [sr20]. Néanmoins, ces méthodes de post-traitements digitaux ne sont pas bien adaptés à des signaux non périodiques, et ne sont pas adéquats pour les signaux optiques ultra-rapides, où l'étape de digitalisation cause un véritable obstacle [sr21]. Récemment, d'autres méthodes agissant directement sur le domaine physique de l'onde ont été proposés (c'est-à-dire, la forme analogue et non digitale) [sr22, sr23, sr24], mais ils demandent de l'information précise sur le signal d'intérêt, tel que la fréquence centrale, la bande passante et la forme spectrale, des paramètres auxquels le dispositif de détection doit être soigneusement calibré. Ces méthodes ne sont pas appropriées pour la détection d'onde arbitraire, de propriété inconnue, de sorte que l'atténuation du bruit interbande demeure une question ouverte.

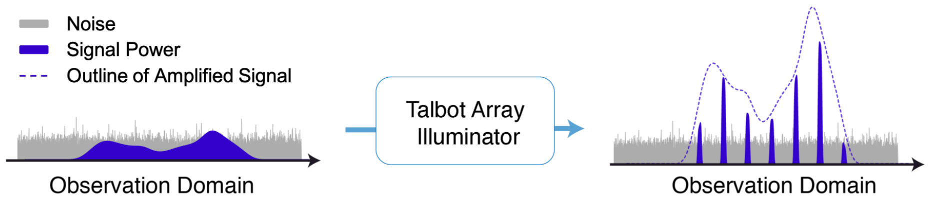

Fig. 2 – Concept de l'amplificateur débruitant.

0.2 Présentation des objectifs du mémoire

Si nous prenons le cas où nous voudrions extraire de l'information d'un signal à basse énergie noyé sous une quantité importante de bruit, avec des propriétés inconnues, un amplificateur qui agirait seulement sur le signal d'intérêt, en baissant la présence relative du bruit, serait un dispositif extrêmement utile. Une tel amplificateur débruitant fonctionnerait donc simultanément comme amplificateur et atténuateur de bruit, augmentant du fait le SNR. De plus, un tel appareil devrait opérer en temps réel et à la volée, sans avoir recours à un post-traitement digital, et devrait pouvoir traiter convenablement un signal à bande étroite ou à large bande, en tenant compte des particularités d'atténuation de bruit de chaque type de signal.

Le développement d'un tel système est l'objectif de mon projet de maitrise. Le concept que nous avons développé est basé sur des opérations d'ondes linéaires, comprenant la dispersion et la modulation de phase temporal. Ces manipulations sont donc applicables à tous les systèmes d'ondes, et peuvent être décrites par des opérations de Fourier élémentaires. La méthode est basée sur l'illumination matricielle Talbot (*Talbot Array Illuminator*, TAI) [sr25], un cas particulier du phénomène d'imagerie de l'effet Talbot [sr26, sr27]. L'idée consiste à recentrer l'énergie du signal en une série de pointes, de sorte à réaliser un processus d'échantillonnage sans perte, tel qu'illustré à la Fig. 2. Vu que le processus conserve l'énergie du signal initial, l'envelope des pointes correspond à une version amplifiée du signal d'entrée. Il est donc important de noter que l'énergie de la forme d'onde de sortie est la même que celle d'entrée (c'est-à-dire, l'intégrale du signal reste la même). C'est pour cette raison que nous référons à cette technique comme une amplification passive, plutôt qu'une amplification active où de l'énergie externe est injectée dans le signal. De plus, vu que le processus compte sur une relation de phases spécifiques, seulement la partie cohérente, est affectée, (c'est-à-dire, la partie avec une phase stable), tandis que le bruit incohérent est laissé intact. Effectivement, la distinction par la nature de la phase entre un signal d'intérêt comparé au bruit est fondamental au concept d'atténuation de bruit présenté. Lorsqu'il est appliqué de façon à agir dans le temps, le dispositif permet d'atténuer le bruit efficacement dans les signaux à bande étroite, en évitant tous les problèmes relatifs au débruitage nommés plus haut pour ce type de signal. Autrement, le système peut être facilement reconfiguré de façon à agir dans le domaine spectral, où le spectre de l'onde est redistribué en une série de pointes dont l'enveloppe suit la forme du spectre du signal initial.

Le concept est démontré ici sur des ondes optiques, dans le régime infrarouge consistant de longueur d'onde près de 1550 nm, en employant des composantes utilisées en télécommunication optique. Il est par contre d'une importance cruciale de se rappeler que le procédé n'est constitué que de manipulations d'ondes décrites par la théorie de Fourier, le concept peut théoriquement être appliqué à tout système d'onde où les phénomènes de dispersion et de modulation de phase temporelle sont accessible. La méthode ici démontrée pourrait donc potentiellement être appliqué à toute plateforme de mesure, comme les régimes du spectre électro-magnétique, ainsi que les systèmes plus exotiques, tel que les ondes de matière quantique, plasmonique, acoustique, etc.

Une brève description de la théorie derrière le concept développé est donnée à la section 0.3, suivit des résultats pour les signaux à bande étroite à la section 0.4 et pour ceux à large bande à la section 0.5. Finalement, ce sommaire récapitulatif se termine avec une courte conclusion en section 0.6. Notez que chacune de ces parties est traitée en plus amples détails dans le texte principal.

0.3 Théorie de base

0.3.1 L'effet Talbot temporel et spectral

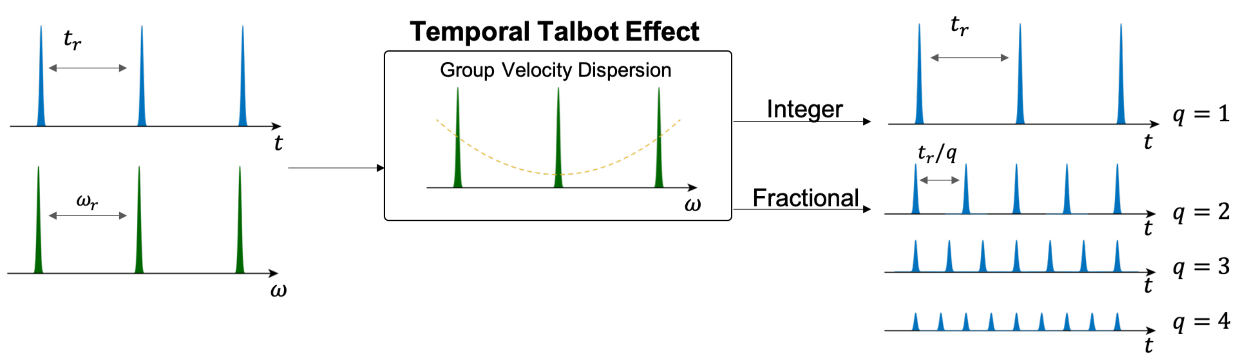

Fig. 3 – Effet Talbot temporel.

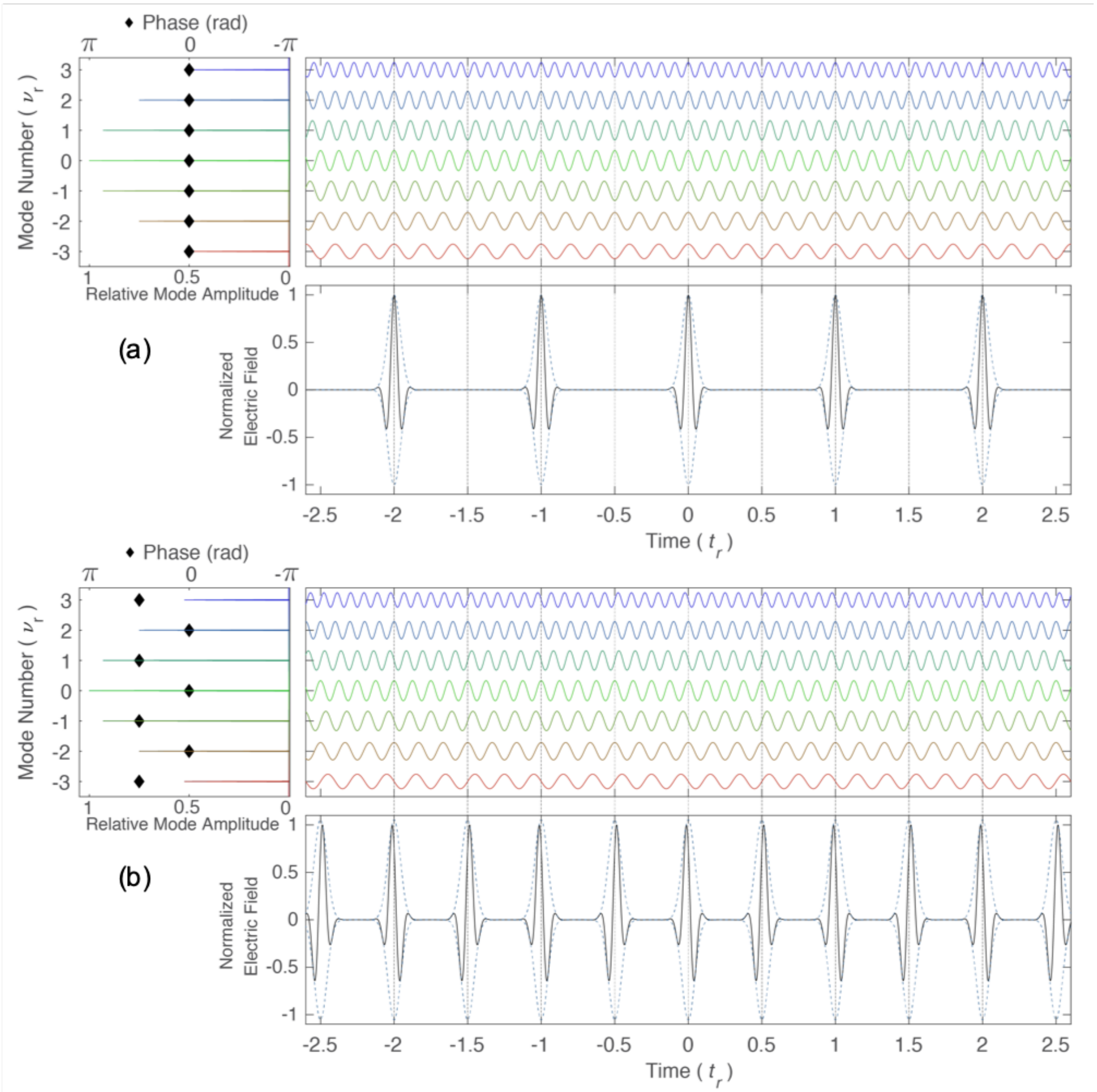

Fig. 4 – Variation de phase dans l'effet Talbot. (a) Quand les modes spectrales sont en phase, la période spectrale est donnée par l'inverse de la période temporelle, $\omega_r = 2\pi/t_r$. (b) Lorsque la variation de phases spectrales acquise par une propagation dispersive satisfait une condition de Talbot pour les chiffres entiers co-prime p et q, les modes spectraux sont alignés de sorte à divisé la période temporelle d'un facteur q. Les pulses démontrent alors une variation de phase périodique après q pulses.

L'effet Talbot a été observé pour la première fois dans le domaine spatial en 1837 [sr28]. Le scientifique Britannique William Henry Fox Talbot a remarqué qu'un réseau de fente illuminé réapparaissait périodiquement lorsqu'un écran était déplacé. Le phénomène a éventuellement été décrit par l'effet de la diffraction, et plus récemment, un phénomène analogue a été décrit dans le domaine temporel [sr26]. En effet, il existe une dualité espace-temps entre l'effet de diffraction et celui de dispersion, de sorte que ces deux phénomènes sont mathématiquement équivalent.

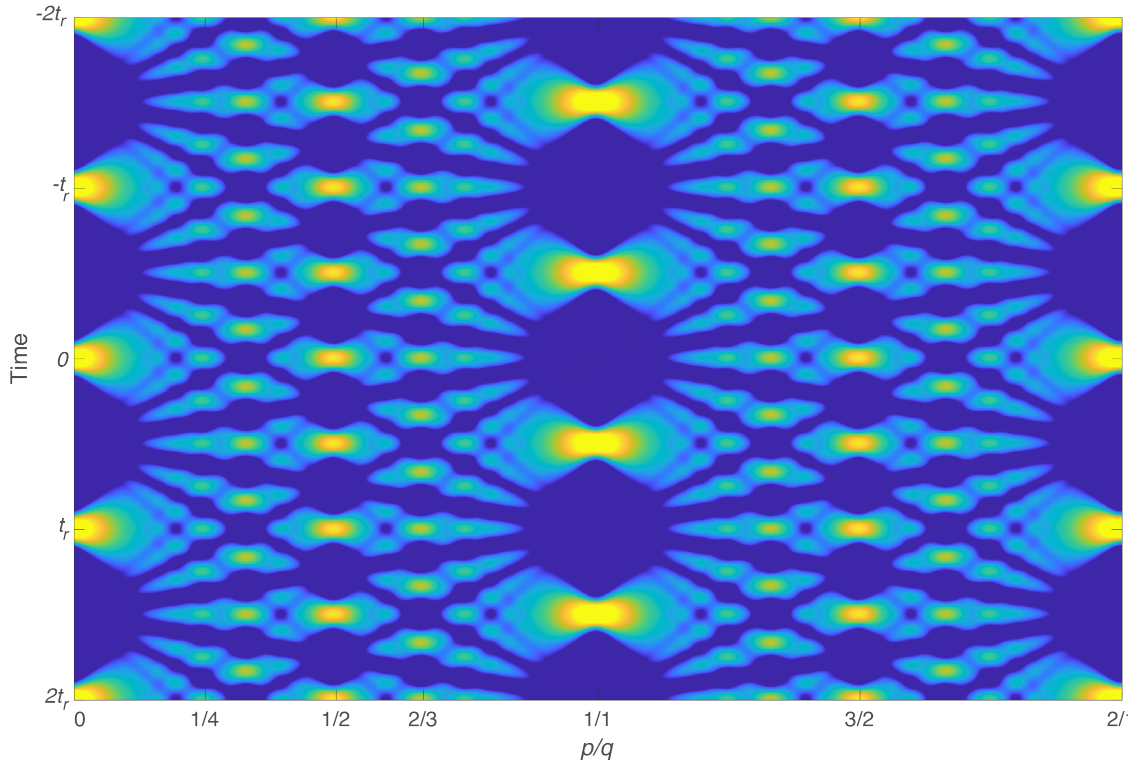

Fig. 5 – Tapis de Talbot. Le tapis de Talbot démontre l'évolution d'un signal temporel pour une valeur grandissante de dispersion, $\ddot{\phi}$. On peut observer qu'un signal avec une période initiale donné par t_r réapparaîtra avec une période égale (effet de Talbot entier) ou une période réduite (effet de Talbot fractionnaire) à différentes valeurs de $\ddot{\phi}$.

Pour les exemples suivants, considérons un signal répétitif qui consiste de plusieurs copies d'une fonction arbitraire $f(t)$ qui répète avec une période temporel t_r:

$$I(t) = \sum_{n=-\infty}^{+\infty} f(t - nt_r). \tag{1}$$

Par des principes de Fourier élémentaire, cette fonction aura une représentation spectrale donnée par une série de lignes infiniment étroites, séparées par une période spectrale ω_r, et avec une enveloppe donnée par le transformé de Fourier de la fonction $f(t)$. Nous rappelons brièvement que pour une dispersion totale $\ddot{\phi}$ (*Group Velocity Dispersion*, GVD) [sr29], l'opérateur de dispersion agit sur le domaine spectral et est écrit comme:

$$\mathcal{H}_{\mathrm{GVD}} = e^{-i\frac{\ddot{\phi}\omega^2}{2}}. \tag{2}$$

L'effet Talbot décrit la formation d'images identique à celui d'entré (voir Fig. 3), mais où la période est divisée par un facteur entier q [sr26], quand la dispersion totale donne:

$$\ddot{\phi}_{p,q} = \frac{2\pi}{\omega_r^2}\frac{p}{q}, \tag{3}$$

où le facteur p dictera la forme exacte de la variation de phase du signal de sortie [sr30, sr31]. En effet, lorsque le signal de sortie a une période moindre que celui d'entrée (c'est-à-dire, $q > 1$), les pulses qui composent le signal de sortie auront une variation de phase, avec une période donnée par le facteur q, tel que démontré à la Fig. 4. Lorsque $q = 1$, l'image est appelée image de Talbot entière (*integer Talbot image*), et lorsque $q > 1$, l'image est appelée image de Talbot fractionnaire (*fractional Talbot image*). En collectant toutes les images produites au long d'une dispersion variant de $\ddot{\phi}_{p,q} = \ddot{\phi}_0$ à $\ddot{\phi}_{p,q} = \ddot{\phi}_{2,1}$, il est possible d'avoir le cycle complet des images Talbot, produisant le tapis de Talbot, tel qu'indiqué à la Fig. 5.

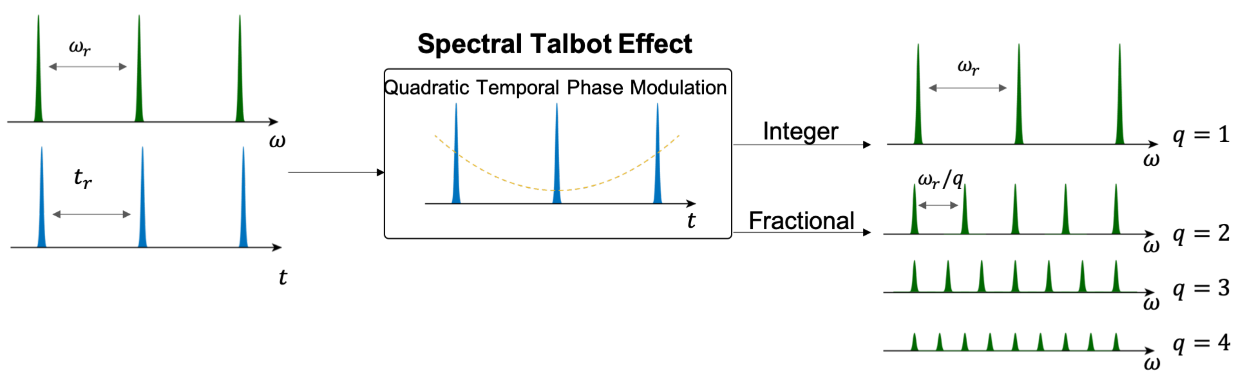

Fig. 6 – Effet de Talbot spectral.

L'effet Talbot peut aussi avoir lieu dans le domaine spectral [sr27], tel d'illustré à la Fig. 6. Dans ce cas, c'est la période spectrale qui est divisé par un facteur q. Ceci est réalisé par l'action d'un propagateur de phase temporel quadratique, décrit comme:

$$h_{\mathrm{TL}} = e^{i\frac{\varphi_0}{2}t^2}. \tag{4}$$

La condition de Talbot pour diviser la période spectrale par q est alors donné par:

$$\varphi_0 = \frac{2\pi}{t_r^2}\frac{s}{q}. \tag{5}$$

où le facteur entier s a un rôle similaire au facteur p donné plus haut, c'est-à-dire qu'il dictera la forme exacte de la séquence de phase qui sera induite dans le domaine spectral.

0.3.2 L'amplification de Talbot

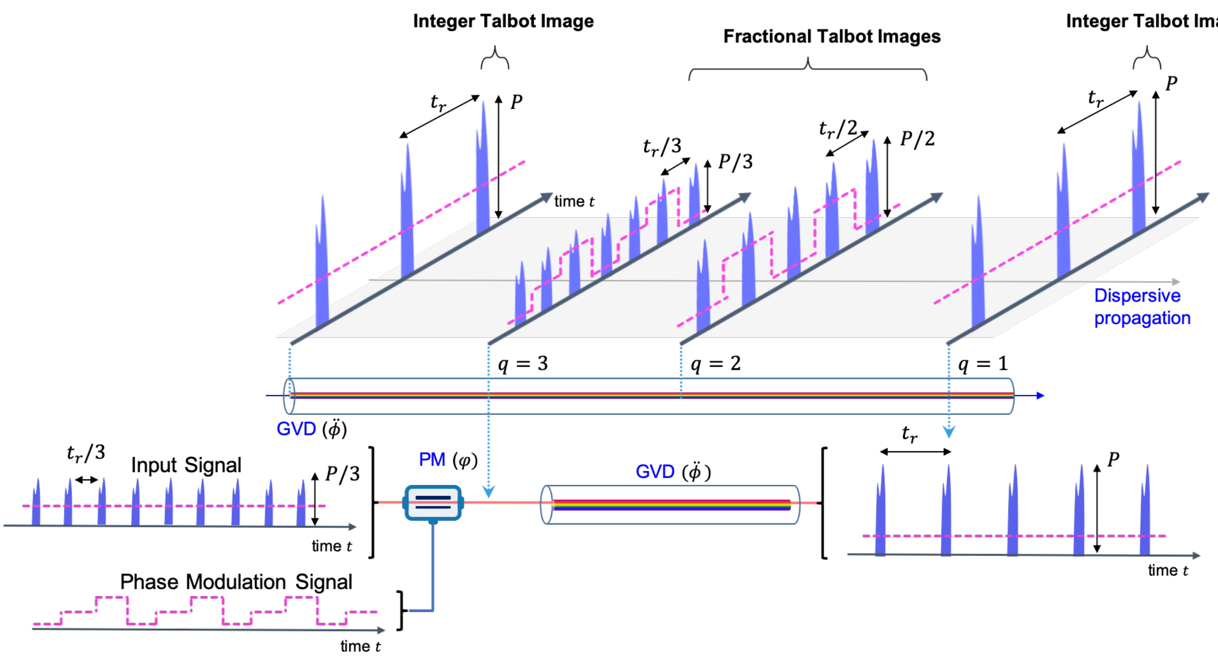

Fig. 7 – Amplification Talbot d'un signal périodique. L'idée consiste à imposer la variation de phase d'une image fractionnaire de Talbot sur le signal d'entré. En faisant ensuite propagé le signal à travers une certaine quantité de dispersion, il est possible d'atteindre la prochaine image Talbot entière. Ceci mène à la sommation de q pulses.

Tel qu'indiqué à la Fig. 4, les images de Talbot fractionnaire ont la particularité d'être rattachées à une variation de phase particulière [sr30, sr31]. La connaissance de ces phases est la clef afin d'implanter un amplificateur Talbot [sr32, sr33]. L'idée derrière l'amplification de Talbot périodique est démontrée à la Fig. 7. Si nous prenons un signal d'entrée qui possède une phase constante, le processus d'amplification de Talbot consiste à imposer la phase d'une image fractionnaire sur le signal d'entré. Ce signal est ensuite propagé dans une quantité de dispersion de sorte à ce que q pulses seront additionnés de façon cohérente. Le signal de sortie correspondra donc à une copie du signal d'entrée, avec un période augmentée du facteur q, et où chaque fonction individuelle sera amplifiée d'un facteur q.

Malgré l'importance des signaux périodiques en science et en technologie, cette nécessité pour le signal d'être périodique limite grandement l'application potentiel de l'amplification périodique de Talbot, particulièrement pour la détection de signaux faibles aux propriétés inconnues. Le

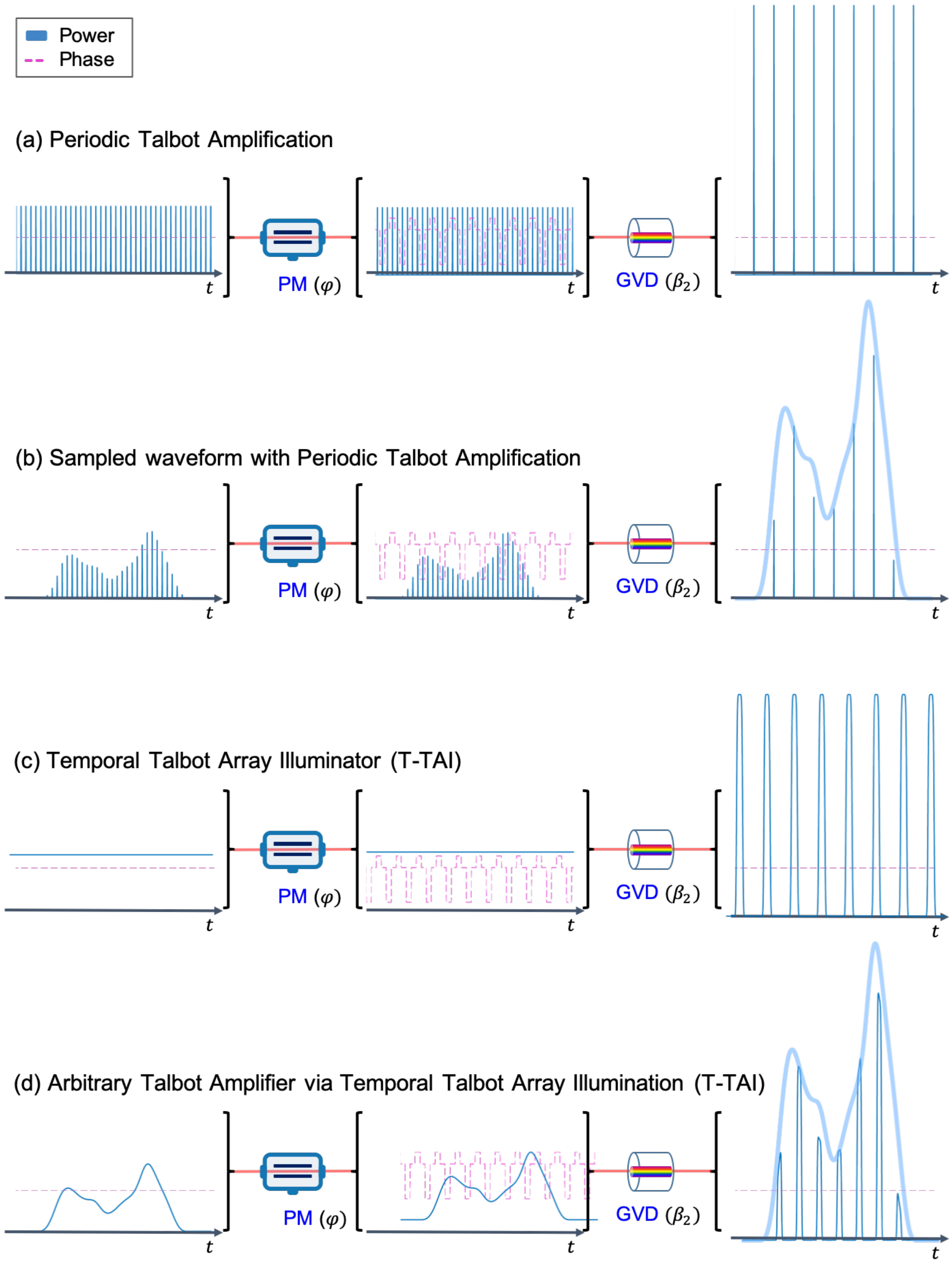

Fig. 8 – Principe d'amplification sans bruit de formes d'ondes arbitraires. (a) Amplification périodique. (b) Amplification périodique sur un signal échantillonnée. (c) l'illumination matricielle Talbot (*Talbot Array Illuminator*, TAI) transforme un signal continue en une série de pointes. (d) Le TAI permet l'amplification de signaux arbitraires de façon efficace, sans perte d'énergie.

but principal de mon projet de maitrise consiste donc à adapter l'idée derrière cette technique pour pouvoir l'appliquer à des signaux non périodiques, ce qui a comme résultat de grandement augmenter le potentiel d'application.

Fig. 9 – Principe d'atténuation de bruit du TAI.

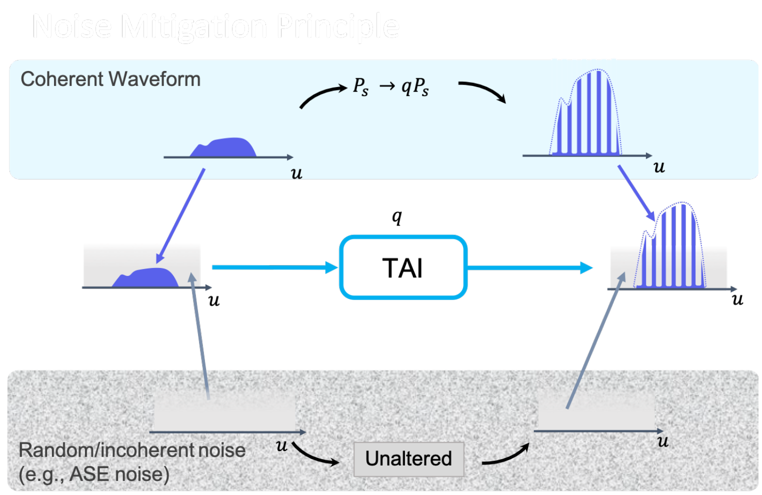

Tel qu'indiqué à la Fig. 8 (b), une approche pourrait être de seulement appliquer l'amplification périodique de Talbot sur un signal échantillonné. Cependant, cette démarche est très inefficace car une large partie du signal doit être rejetée. En revanche, la périodicité du signal de phase est elle-même suffisante pour créer l'effet voulu. Il est donc possible de transformer un signal continue en une série de pointes, sans aucune perte d'énergie (voir Fig. 8). Expérimentalement, le signal de modulation temporel est composé de q niveaux, chacun d'une durée t_s, produisant un signal périodique d'une durée $t_q = qt_s$. En propageant ce signal à travers une quantité particulière de dispersion, l'énergie est donc redistribuée en pique d'une largeur t_s, séparés d'une durée $t_q = qt_s$.

Il s'avère qu'une idée similaire avait été mise de l'avant dans les années 80 dans le domaine spatial, afin de transformer un front d'onde en une série de point lumineux [sr25]. Ce phénomène était alors appelé illumination matricielle Talbot (*Talbot Array Illuminator*, TAI) et était utilisé pour, par exemple, alimenter en énergie des processeurs lumineux, mais jamais pour le traitement d'image. La contribution principale de cette thèse est donc de démontrer que la théorie derrière l'illumination matricielle Talbot peut soit être appliquée dans le domaine temporel pour résoudre le problème du bruit dans les signaux à bande étroite (T-TAI) [AC1, AC2, AC3], ainsi que dans le domaine spectral afin de résoudre le problème du bruit dans les signaux à large bande (S-TAI) [AC4, AC5, AC6].

Le concept de débruitage est illustré à la Fig. 9. Tel que discuté plus haut, l'amplification de Talbot ne consiste que de manipulations de phase. Le procédé dépend donc fortement du comportement de la phase du signal. Vu que le bruit comporte de violentes fluctuations de phase, la condition de Talbot n'est pas satisfaite, donc aucune amplification prend lieu. En revanche, le signal cohérent composé d'une phase stable sera amplifié en piques, avec une enveloppe qui correspond au signal d'entrée.

Comme tout processus d'échantillonnage, les échantillons doivent respecter le critère d'échantillonnage de Nyquist. Ceci mène à la limitation de la méthode; pour un échantillonnage serré dans le temps, nécessaire pour un signal qui varient très rapidement dans le temps, un signal très rapide est nécessaire pour imposer la modulation de phase requise sur le signal. Le T-TAI rencontre donc habituellement sa limitation pour des signaux ultra-rapides. De l'autre côté, pour un échantillonnage dans le domaine spectral, une grande résolution spectrale nécessite une grande quantité de dispersion. Le S-TAI est donc habituellement limité par la durée temporelle maximale qu'un signal traitable peut avoir.

0.4 Résultats expérimentaux pour le traitement de signaux à bande étroite

L'installation expérimentale du T-TAI pour démontrer le concept de débruitage pour les signaux à bande étroite est illustrée à la Fig. 10. Un laser à onde continue génère un signal CW à une longueur d'onde de 1551 nm, puis ce signal est modulé en intensité par un modulateur Mach-Zender (*Intensity Modulator*, IM) commandé par un générateur d'onde arbitraire (*Arbitrary Waveform Generator*, AWG) à fréquences radios. Ce signal est ensuite combiné au bruit généré par un EDFA (*Erbium-Doped Fiber Amplifier*) pour les expériences de débruitage, afin de baisser le SNR du signal d'entré. Le signal est ensuite rétabli par le T-TAI, comprenant un modulateur de phase (*phase modulator*, PM), dirigé par un second AWG, suivit d'un réseaux de diffraction Bragg en fibre à variation linéaire (*Linearly Chirped Fiber Bragg Grating*, LCFBG) pour la dispersion. Le signal de sortie est ensuite enregistré par un détecteur optique et un oscilloscope à haute vitesse. Les résultats présentés dans cette section ont été rapportés dans [AC1, AC2, AC3].

La Fig. 11 démontre une amplification par un facteur $q = 28.5$, avec des pointes d'une largeur $t_s = 47$ ps, séparées d'une durée moyenne $t_q = 1.53$ ns. Compte tenu des valeurs de conceptions de $q = 30$, $t_s = 51.5$ ps et $t_q = 1.56$ ns, l'expérience a donnée des résultats près de ceux attendus. Notez bien que la valeur de 28.5 est obtenue en mesurant le signal de sortie avec le PM activé et le comparant ensuite au signal mesuré au même endroit avec le PM désactivé. De cette façon, il est possible de prendre en compte seulement l'amplification produite. Pour mesurer l'amplification

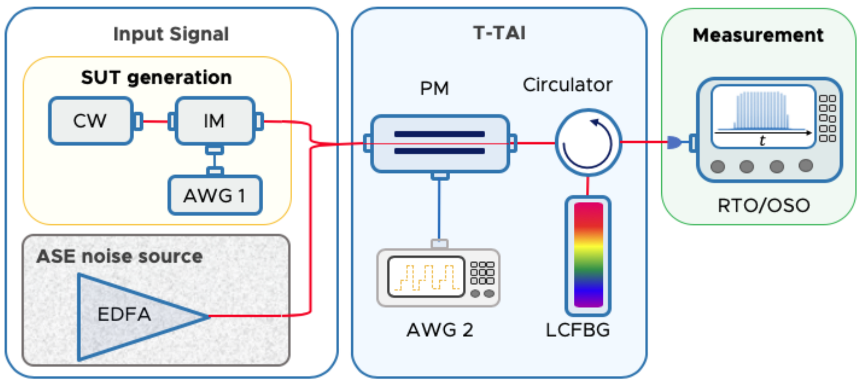

Fig. 10 – Installation expérimentale pour le T-TAI. CW: *Continuous Wave*, IM: *Intensity Modulator*, AWG: *Arbitrary Waveform Generator*, EDFA: *Erbium-Doped Fiber Amplifier*, PM: *Phase Modulator*, LCFBG: *Linearly Chirped Fiber Bragg Grating*, RTO: *Real-Time Oscilloscope*, OSO: *Optical Sampling Oscilloscope*.

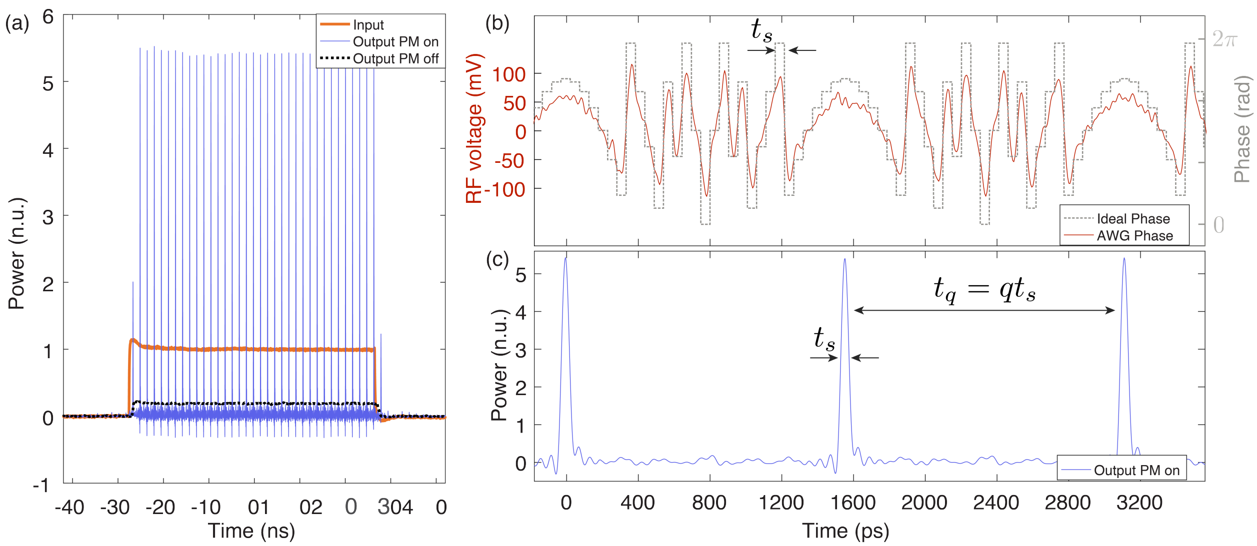

Fig. 11 – Démonstration expérimentale du T-TAI. (a) le signal d'entrée est montré en orange. Le signal de sortie avec la modulation de phase désactivée est montré en noir, indiquant la perte d'insertion. Le signal de sortie avec le PM activé (c'est-à-dire, le T-TAI) est illustré en bleu, démontrant une amplification de 28.5 (amplification nette de 5.42). (b) Voltage du signal généré par le AWG (rouge), comparée à la valeur idéal (gris). (b) Largeur des pointes t_s du T-TAI leur séparation t_q.

nette, nous avons mesuré le signal au point d'entré du T-TAI. Dans ce cas, nous mesurons une amplification d'un facteur de 5.42 dû à la perte d'insertion d'environ 7.3 dB. Il est important de noter que la perte d'insertion pourrait être baissé à environ 3 dB.

L'amplificateur Talbot avec les même paramètres de conception a par la suite été utilisé pour rétablir un signal en rampe noyé sous une importante quantité de bruit (voir Fig. 12). Le signal a bel et bien été rétabli, et la performance du T-TAI surpasse celle d'un filtre à bande étroite.

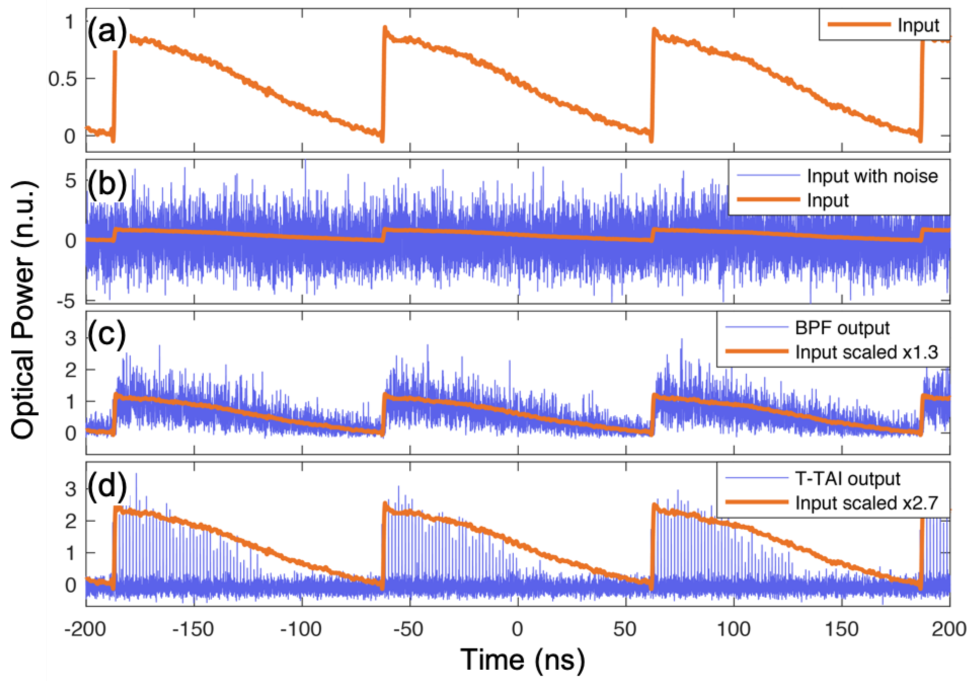

Fig. 12 – Rétablissement d'un signal couvert sous bruit par le T-TAI.

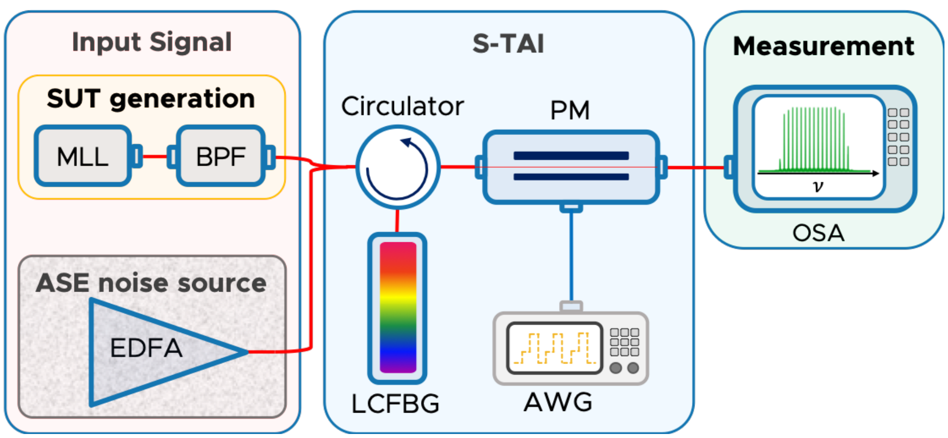

Fig. 13 – Installation expérimentale pour le S-TAI. MLL: *Mode Locked Laser*, BPF: *BandPass Filter*, AWG: *Arbitrary Waveform Generator*, EDFA: *Erbium-Doped Fiber Amplifier*, PM: *Phase Modulator*, LCFBG: *Linearly Chirped Fiber Bragg Grating*, OSA: *Optical Spectrum Analyzer*.

0.5 Résultats expérimentaux pour le traitement de signaux à large bande

L'installation expérimentale utilisée pour démontrer le S-TAI est illustrée à la Fig. 13. Le signal est généré par un laser à modes verrouillées (*Mode Locked Laser*, MLL), avec une fréquence de répétition de 10 MHz, filtré à une gamme spectrale donnée. Pour les expériences de débruitage, le signal est combiné avec le bruit généré par un EDFA (*Erbium-Doped Fiber Amplifier*), de sorte à complètement noyer le signal sous du bruit interbande. Ce signal à bas SNR est ensuite récupéré par le dispositif S-TAI, qui consiste d'un LCFBG (*Linearly Chirped Fiber Bragg Grating*) suivit d'un PM (*Phase Modulator*) commandé par un AWG (*Arbitrary Waveform Generator*). Le signal de sortie est mesuré par un analyseur de spectre optique (*Optical Spectrum Analyzer*, OSA). Les résultats présentés dans cette section ont été rapportés dans [AC4, AC5, AC6]

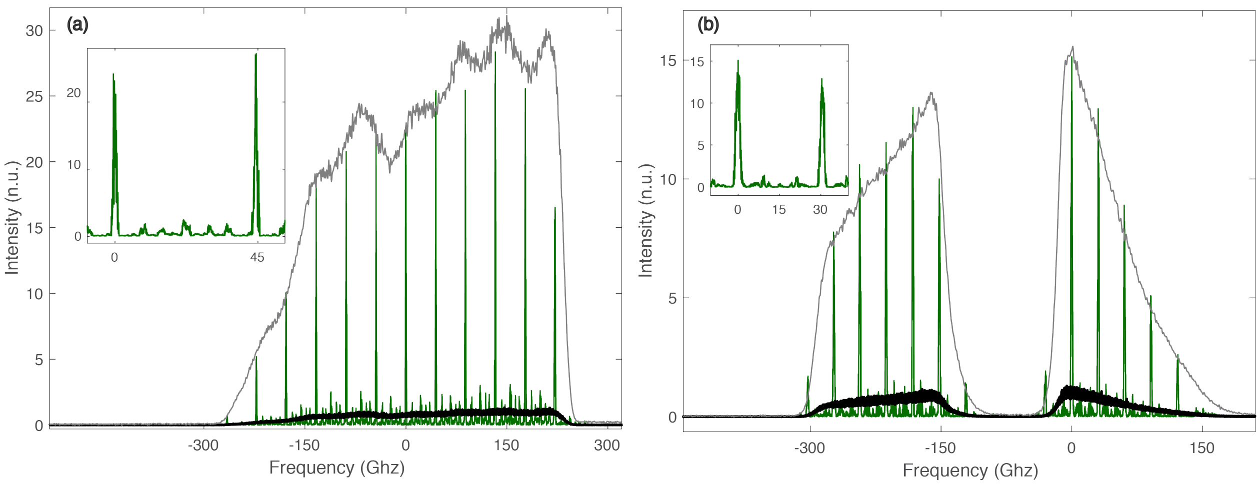

Fig. 14 – Démonstration de base du S-TAI, pour (a) une amplification élevée d'une valeur de 28.8 et (b) résolution spectrale reconfigurable.

Le potentiel du S-TAI pour atteindre de hauts facteurs d'amplification est démontré à la Fig. 14 (a). La valeur mesurée est de $q = 29.1$, pour une valeur de conception de $q = 32$. Dans ce cas, les pointes étaient conçues pour avoir une largeur de $\omega_s = 1.4$ GHz, séparées par $\omega_q = 44.8$

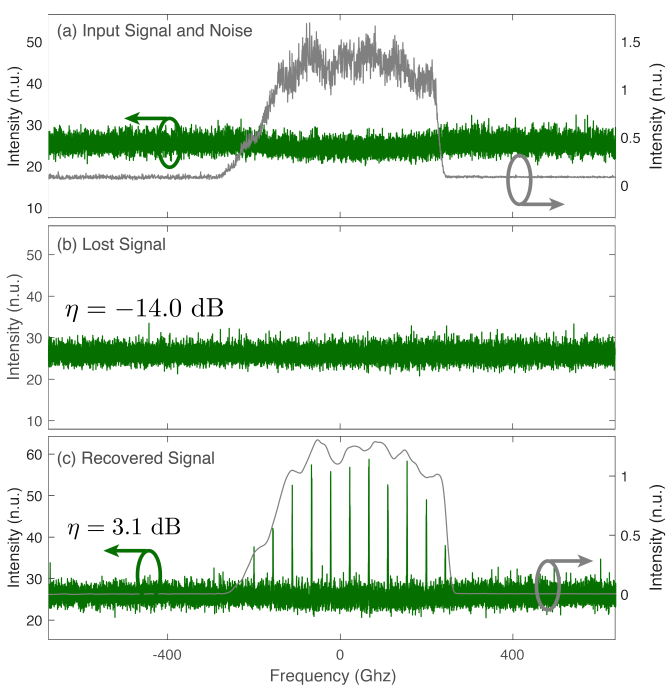

Fig. 15 – Rétablissement d'un signal couvert sous bruit interbande par le S-TAI.

GHz. Les valeurs mesurées était de $\omega_s = 1.6$ GHz et $\omega_q = 44.4$ GHz, près des valeurs attendues. Afin d'amplifier un spectre plus compliqué, la valeur pour la distance entre les pointes fut réduite à $\omega_q = 30.3$ GHz afin de respecter le critère d'échantillonnage (voir 14 (b)). Il est important de noter que contrairement à l'habitude, où le critère d'échantillonnage est appliqué pour la version temporelle du signal, ici c'est la forme du spectre qui doit être échantillonnée. Donc le critère d'échantillonnage s'applique à la forme de la représentation spectrale de la forme d'onde. De plus, vu que les deux configurations utilisaient le même LCFBG pour la dispersion, il était possible de simplement reconfigurer le AWG pour changer entre ces deux configurations.

Finalement, nous démontrons le rétablissement d'une onde totalement couverte sous du bruit interbande en utilisant le S-TAI conçu à la Fig. 14 (a). Tel qu'indiqué à la Fig. 15 (a), le signal d'entrée avait une puissance de 1 unité normalisée. (*Normalized Unit*, n.u.). Ce signal fut ensuite combiné à 25 n.u. de bruit, de sorte à noyé le signal sous le bruit. Tel qu'indiqué à la Fig. 15 (c), le faible signal d'entrée peut être rétablie en activant le S-TAI.

0.6 Conclusion

En conclusion, nous avons présenté une méthode novatrice pour le rétablissement de signaux couverts sous une grande quantité de bruit. Le concept permet d'amplifier des signaux à bande étroite ainsi que ceux à large bande. Le tout s'effectue sans affecter le bruit, de sorte à permettre le rétablissement de signaux cohérents totalement noyés sous le bruit. Nous prévoyons que cette technique pourrait permettre la détection de signaux présentement inaccessible, non seulement en optique mais aussi pour d'autres supports physiques, ce qui pourrait avoir un impact important dans plusieurs secteurs scientifiques et technologiques.

Références

[sr1] A. R. Liddle and M. Cortês, “Cosmic Microwave Background Anomalies in an Open Universe,” Physical Review Letters **111** (2013).

[sr2] A. J. Levan, N. R. Tanvir, S. B. Cenko *et al.*, “An Extremely Luminous Panchromatic Outburst from the Nucleus of a Distant Galaxy,” Science **333**, 199–202 (2011).

[sr3] D. Brinks, R. Hildner, E. M. H. P. van Dijk *et al.*, “Ultrafast dynamics of single molecules,” Chem. Soc. Rev. **43**, 2476–2491 (2014).

[sr4] C. DeCusatis, *Handbook of Fiber Optic Data Communication: A Practical Guide to Optical Networking* (Elsevier Science, 2013).

[sr5] S. V.Vaseghi, *Advanced Digital Signal Processing and Noise Reduction* (2000), john wiley & sons ltd ed.

[sr6] S. Weiss, “Fluorescence Spectroscopy of Single Biomolecules,” Science **283**, 1676–1683 (1999).

[sr7] A. Raman, “On the Signal Processing Operations in LIGO signals,” 2018 IEEE Global Conference on Signal and Information Processing (GlobalSIP) 1086–1090 (2018).

[sr8] V. A. Galievsky, A. S. Stasheuski, and S. N. Krylov, “Improvement of LOD in Fluorescence Detection with Spectrally Nonuniform Background by Optimization of Emission Filtering,” Analytical Chemistry **89**, 11122–11128 (2017).

[sr9] A. Demir, “Noise analysis for optical fiber communication systems,” in *ICCAD-2003. International Conference on Computer Aided Design (IEEE Cat. No.03CH37486)* (IEEE, San Jose, CA, USA, 2003), 441–445.

[sr10] M. Mazalkova, “The Laser Satellites Communications and Laser Noises,” **7**, 10 (2008).

[sr11] W. K. Wootters and W. H. Zurek, “A single quantum cannot be cloned,” Nature **299**, 802–803 (1982).

[sr12] C. M. Caves, “Quantum limits on noise in linear amplifiers,” Physical Review D **26**, 1817–1839 (1982).

[sr13] A. Zavatta, J. Fiurášek, and M. Bellini, “A high-fidelity noiseless amplifier for quantum light states,” Nature Photonics **5**, 52–60 (2010).

[sr14] Z. Tong, C. Lundström, P. A. Andrekson *et al.*, “Towards ultrasensitive optical links enabled by low-noise phase-sensitive amplifiers,” Nature Photonics **5**, 430–436 (2011).

[sr15] J. Capmany, B. Ortega, and D. Pastor, “Fibre optic bandpass filter with subpicometre bandwidth using a fibre grating and two fibre Fabry-Perot filters,” Electronics Letters **33**, 1970–1972 (1997).

[sr16] W. T. Wang, J. G. Liu, W. H. Sun *et al.*, “Widely tunable single bandpass microwave photonic filter based on Brillouin-assisted optical carrier recovery,” Optics Express **22**, 29304 (2014).

[sr17] H. Maki, T. Toda, S. Sakti, G. Neubig, and S. Nakamura, “EEG signal enhancement using multi-channel wiener filter with a spatial correlation prior,” in *2015 IEEE International Conference on Acoustics, Speech and Signal Processing (ICASSP)* (IEEE, South Brisbane, Queensland, Australia, 2015), 2639–2643.

[sr18] J. Benesty, *Noise Reduction in Speech Processing*, no. v. 2 in Springer Topics in Signal Processing (Springer, Dordrecht ; London ; New York, 2009).

[sr19] B. Ergen, “Signal and Image Denoising Using Wavelet Transform,” in *Advances in Wavelet Theory and Their Applications in Engineering, Physics and Technology*, D. Baleanu, ed. (InTech, 2012).

[sr20] I. S. Bozchalooi and M. Liang, “A joint resonance frequency estimation and in-band noise reduction method for enhancing the detectability of bearing fault signals,” Mechanical Systems and Signal Processing **22**, 915–933 (2008).

[sr21] R. Walden, “Analog-to-digital converter survey and analysis,” IEEE Journal on Selected Areas in Communications **17**, 539–550 (1999).

[sr22] J. Wang, J. Ma, P. Yuan *et al.*, “In-Band Noise Filtering via Spatio-Spectral Coupling,” Laser & Photonics Reviews **12**, 1700316 (2018).

[sr23] V. Ataie, D. Esman, B. P.-P. Kuo, N. Alic, and S. Radic, “Subnoise detection of a fast random event,” Science **350**, 1343–1346 (2015).

[sr24] M. Vasilyev, “Matched filtering of ultrashort pulses,” Science **350**, 1314–1315 (2015).

[sr25] A. W. Lohmann, “An array illuminator based on the Talbot-effect,” Optik **79**, 41–45 (1988).

[sr26] J. Azana and M. Muriel, “Temporal self-imaging effects: Theory and application for multiplying pulse repetition rates,” IEEE Journal of Selected Topics in Quantum Electronics **7**, 728–744 (July-Sept./2001).

[sr27] J. Azaña, “Spectral Talbot phenomena of frequency combs induced by cross-phase modulation in optical fibers,” Optics Letters **30**, 227 (2005).

[sr28] H. Talbot, “LXXVI. Facts relating to optical science. No. IV,” The London, Edinburgh, and Dublin Philosophical Magazine and Journal of Science **9**, 401–407 (1836).

[sr29] G. Agrawal, *Nonlinear Fiber Optics*, Optics and Photonics (Elsevier Science, 2013).

[sr30] L. Romero Cortés, H. Guillet de Chatellus, and J. Azaña, “On the generality of the Talbot condition for inducing self-imaging effects on periodic objects,” Optics Letters **41**, 340 (2016).

[sr31] C. R. Fernández-Pousa, “On the structure of quadratic Gauss sums in the Talbot effect,” Journal of the Optical Society of America A **34**, 732 (2017).

[sr32] R. Maram, J. Van Howe, M. Li, and J. Azaña, "Noiseless intensity amplification of repetitive signals by coherent addition using the temporal Talbot effect," Nature Communications **5** (2014).

[sr33] L. Romero Cortés, R. Maram, H. Guillet de Chatellus, and J. Azaña, "Subnoise Detection and Passive Amplification of Frequency Combs through Customized Coherent Spectral Energy Redistribution," Physical Review Applied **9** (2018).

Contents

List of Figures

List of Tables

Nomenclature

Accronyms and abbreviations

ASE	Amplified Spontaneous Emission
AWG	Arbitrary Waveform Generator
BPF	BandPass Filter
CMB	Cosmic Microwave Background
CV	Coefficient of Variation
CW	Continuous Wave
DFT	Discrete Fourier Transform
DSP	Digital Signal Processing
EDFA	Erbium-Doped Fiber Amplifier
EEG	ElectroEncephaloGram
EM	ElectroMagnetic
EOPM	Electro-Optic Phase Modulator
FBG	Fiber Bragg Grating
FSR	Free Spectral Range
GVD	Group Velocity Dispersion
IM	Intensity Modulator
LCFBG	Linear-Chirped Fiber Bragg Grating
LiDAR	Light Detection And Ranging
n.u.	Normalized Unit
NF	Noise Figure
OSA	Optical Spectrum Analyzer
OSNR	Optical Signal to Noise Ratio
OSO	Optical Sampling Oscilloscope
PIA	Phase Insensitive Amplifier
PM	Phase Modulator
PSA	Phase Sensitive Amplifier
RF	Radio Frequency
RTO	Real-Time Oscilloscope
S-TAI	Spectral Talbot Array Illuminator
SBS	Stimulated Brillouin Scattering
SMF	Single Mode Fiber
SNR	Signal to Noise Ratio
SPCC	Square Pearson Correlation Coefficient
SUT	Signal Under Test
T-TAI	Temporal Talbot Array Illuminator
TAI	Talbot Array Illuminator
VRF	Variation Reduction Factor
XPM	Cross-Phase Modulation

Talbot parameters

ω_q	Angular frequency width of a total phase cycle, $\omega_q = q\omega_s$
ω_s	Angular frequency width of a single phase level
σ_ϕ	Phase modulation sign ($\sigma_\phi = \pm 1$)
p	Primary phase factor
q	Amplification factor
s	Secondary phase factor
t_q	Temporal duration of a total phase cycle, $t_q = qt_s$
t_s	Temporal duration of a single phase level

Other Symbols

β	Propagation constant
β_2	Second-order dispersion coefficient (units ps^2/km)
$\ddot{\phi}$	Total dispersion (units ps^2)
$\ddot{\phi}_{p,q}$	Total dispersion for Talbot image of order $\{p, q\}$
Δ_ν	Broad frequency band
δ_{ν_0}	Narrow frequency band centered at ν_0
λ	Wavelength
$\mathcal{E}$	Photon energy
$\mathcal{H}_{\mathrm{GVD}}(\omega)$	GVD propagator
$\mathscr{F}\{\cdot\}$	Fourier transform
$\mathscr{F}^{-1}\{\cdot\}$	Inverse Fourier transform
μ	Mean
ν	Linear frequency
ω	Angular frequency
ω_r	Angular frequency spectral period of a transform limited periodic function (fundamental Talbot image)
ρ	Pearson correlation coefficient
σ	Standard deviation
$\tau_g(\omega)$	Group delay
φ	Temporal phase
c	Speed of light
D	Dispersion coefficient (units ps/nm/km)
e_q	Parity of q; $e_q = 0$ for even q and $e_q = 1$ for odd q
h	Planck's constant
$h_{\mathrm{TL}}(t)$	Quadratic temporal phase propagator
$n(\omega)$	Index of refraction
T	Electric field period
t	time
t_r	Temporal period of a transform limited periodic function (fundamental Talbot image)
U	Fourier-dual domain variable
u	Observation domain variable
U_r	Period of Fourier-dual domain signal
u_r	Period of observation domain signal
z	Spatial propagation variable

Chapter 1

Introduction

This chapter introduces the idea of an ideal denoising amplifier. A general introduction on the subject of amplification and noise mitigation of optical signals is given, followed by a description of the objectives of this thesis.

1.1 Amplification and noise mitigation of optical signals

Any knowledge we obtain ultimately relies on our ability to perform a measurement. This measurement process generally consists of transferring information from a system to one that we can consciously interpret. Let me stress that generally, the term information is not restricted to its typical use in telecommunication or computer science; rather, it may broadly refer to any description of what an entity is. Information can be as ordinary as the distance between two cities, the colour of an autumn leaf, the velocity at which a vehicle is travelling, or the meaning behind the sound of spoken words, such that the measurement process may require a simple tool or simply our human senses. On the other hand, the process required to infer about the state of an entity may in some cases require highly specialized instruments to be able to extract the relevant information from a given system. For example, to measure the cosmic microwave background (CMB), radiation left over from the formation of the universe, sophisticated satellites with highly sensitivity antennas are sent out in space. This obtained information in turn allows scientist to hypothesize about the shape and expansion of the universe [1], or to confirm predictions of the standard model of particle physics

[2]. There is of course a plethora of entities that may be measured by different methods, and this measurable, experimental component of information is central to the development of science.

In virtually all cases, the information is supported by some form of wave system, either mechanical or electromagnetic in nature. Furthermore, a measurement process typically not only relies on a detection stage; the information bearing waveform usually needs to propagate over some distance, from the entity being investigated to the detection apparatus. In some cases, the measurement process also consists of producing the waveform to be detected by probing the investigated entity externally. Optics and photonics, the field dealing with the manipulation and processing of electromagnetic waves from the X-ray to infrared regimes, have turned out to be particularly well suited for measurement systems due to various key advantages, such as its unique sensitivity interacting with matter in a non-intrusive manner, as well as its ability to convey information over long distances effectively. Photonic approaches are now key for the measurement of various phenomena, from the investigation of astronomical events billions of light-years away in the cosmos [3, 4, 5], to enabling investigation of the microscopic world by probing the dynamics of chemical and biological reactions [6, 7]. Photonics have also been central to a plethora of technological advancements, for example by permitting the transfer of massive amounts of data across the Internet, enabled by the high information capacity offered by fiber technologies and its near-instantaneous transmission worldwide [8], or yet also by the development of imaging technologies that allow small cellphone cameras to take pictures of an incredibly high resolution and quality [9]. Photonic advancements have certainly had an immense impact on humankind, not only scientifically, but also technologically and socially. However, there is a key issue central to any measurement process which also limits the potential application of optical approaches, namely the ubiquitous problem of noise.

In the context of signal processing, noise is defined slightly differently than how it is typically used in every day life to describe, for example, the sound coming from a car engine or from a loud construction site. Many definitions have been proposed, but when dealing with measurements, noise can generally be defined as an unwanted, stochastic disturbance which may interfere with the communication or measurement of another signal, tending to obscure its content [10, 11]. Here, we stress that we will reserve the term noise to refer to the part of a signal which is stochastic, uncorrelated and rapidly fluctuating. Note that randomness in its own is not a criteria for noise, since for example, a data signal would appear to be random from an outside observer, yet one would agree that such a signal does not qualify as noise. In fact, noise often finds its root in physical phenomena, such as the thermal noise in electronic circuits that arises from the random thermal motion of electrons, or the shot noise resulting from the random passage of individual particles across a potential barrier. Conversely, there are fields where noise can refer to any unwanted signal, regardless of if it is random in nature. An example of this would be the intrusion of an external signal due to undesirable crosstalk resulting from parasitic coupling between nearby channels [11]. Without loss of generality, the term noise employed here does not refer to such distortions as noise, reserving it to undesirable signals which are incoherent and stochastic in nature, with unpredictable rapid amplitude and phase variations.

Although optics and photonics have proven to offer key advantages over other media for measurement, metrology as well as information processing and transmission, the presence of incoherent noise ultimately limits the sensitivity of a measurement, restricting further developments in a range of different fields, such as biology [12, 13], fundamental physics [14] and chemistry [15]. It also limits the reach of information transmission links [16, 17], and implementation of satellite communications [18], and as such, has been the subject of much research in the past few decades [19, 20]. The development of new methods to tackle this important problem of noise is the central point of this thesis, with the specific aim of targeting the issues associated with noise mitigation in the optical domain, due to the importance of optics and photonics in modern science and technology.

The problem of noise is particularly pervasive in the case of low energy waveforms. If an optical signal of interest is weak, it is typically amplified by injecting external energy into it. However, active amplification schemes do not only act on the signal of interest in a given electromagnetic radiation, but also on any other undesired signal (e.g., noise) contained within. Furthermore, any linear amplifier, which is an amplifier whose output is linearly related to its input signal, will inject further amounts of noise, as dictated by fundamental laws of quantum mechanics [21]. The pioneering work by Carlton M. Caves on this subject showed that this type of amplifier, which includes Erbium-Doped Fiber Amplifier (EDFA) and Phase-Insensitive parametric Amplifiers (PIA), will necessarily degrade the signal-to-noise ratio (SNR) by at least 3 dB [22]. The fact that an amplifier must degrade the SNR of a given signal is related to the no-cloning theorem of quantum mechanics [21], which may heuristically be understood by the impossibility to perfectly replicate a given quantum state due to the uncertainty principle. There has been significant work in the direction of noiseless amplification, which in principle, can be realized in a non-deterministic way [23] or by phase-sensitive parametric amplification (PSA) [22, 24]. The former solution however suffers from low success probability and is not practical for typical implementation outside of niche quantum optics applications. On the other hand, the performance of PSA has improved significantly since the first demonstration of a sub-3dB SNR degradation in 1999 [25, 26]. SNR degradation as low as 1.1 dB have been demonstrated in 2011 [24], and PSA has also displayed interesting properties against nonlinearity induced distortion [27]. The principle behind PSA is related to that of optical squeezing, which have allowed scientists to perform sensitive measurements at noise levels below the fluctuations of the vacuum. Squeezing consists of attenuating a quadrature of the electric field while amplifying the other quadrature. This is done directly on the fluctuations of the vacuum, such that the attenuated quadrature has a lower noise level than the amplitude of the vacuum fluctuations. This is possible due the fact that the noise is simultaneously amplified in the conjugated quadrature, such that the overall noise is constant, thus maintaining the uncertainty relation in the complex plain [28, 29, 30]. In PSA, the signal is injected in the amplified quadrature, and since the other quadrature is attenuated, the total amount of noise can theoretically be kept constant for a given amplification [31]. However, the signal must be maintained in-phase with the PSA, requiring sophisticated phase stabilization schemes to avoid any attenuation of the signal from being in the attenuated quadrature. Furthermore, due to the inherent phase squeezing process in PSA, further phase compensation is required to amplify data signal with complex modulation in order to avoid any signal distortion [24]. Furthermore, PSA demands for very high phase matching over large bandwidths and stable phase locking, making them difficult to implement in practice. Ultimately however, even an ideal 0 NF amplifier would still act on the noise already contained within a signal before it is amplified, such that noise mitigation methods would still be needed in this case. In general, the appropriate method for noise mitigation depends on the nature of the signal, which may be categorized by the frequency extent of its spectral representation, either narrowband or broadband.

Signals that consist of very few frequency components are called narrowband signal, and are characteristically relatively slow, and extend over long time durations. On the other hand, if a signal changes rapidly over time, it will have a spectral representation given by a very large amount of frequency components, and is thus referred to as a broadband signal (see Fig. 1.1). The transition between these two regimes naturally depends on the specific field (i.e., acoustic waves, radio waves, microwaves, optical, etc.). Heuristically, in the case of optical signal processing, signals with bandwidths of less than about 10 GHz would be considered as narrowband, whereas signals

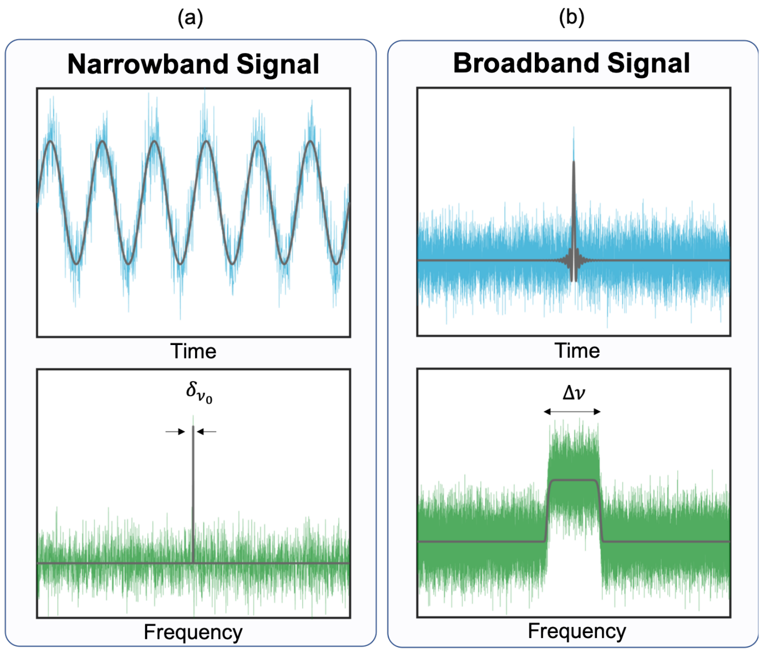

Fig. 1.1 – Challenges with noise mitigation for narrowband and broadband signals. (a) Narrowband signals consists of a very narrow range of frequencies δ_{ν_0}. It is hard to mitigate the noise contained in these signals effectively since it is difficult to efficiently manipulate signals with a very fine spectral resolution. (b) On the other hand, broadband signals are composed of a large range of frequency components Δ_ν. In this case, solutions to mitigate noise contained within the frequency range of a signal, so-called in-band noise, are severely limited, and this specific issue has been a long-standing hurdle in the field of signal processing.

with bandwidths above 50 GHz would be considered as broadband; those in between being in some intermediate regime.

Narrowband optical signals are present in a wide range of fields, particularly to interact with relatively low speed systems consisting of electrical or mechanical processes. For example, they are used in information and communication technologies to process and transfer data signals meant to interact with lower frequency electronics, such as microwave and radio-over fiber communication channels [32, 33, 34, 35, 36, 37]. Narrowband signals also include continuous-wave (CW)-like signals, such as those used in interferometric structures to measure small changes in path lengths, used for example in sensing for structural health monitoring [38, 39, 40] and gravitational wave detection [14, 41]. Other areas using narrowband signal are in biosensing [42, 43] and light detection and ranging (LiDAR) [44, 45]. To denoise a narrowband optical signal, the most common approach consists in attenuating all frequency components outside of the spectral bandwidth of the signal using a filtering device. In the optical domain, commonly used instruments for this purpose include Fiber Bragg Gratings (FBG), Fabry-Perot cavities and ring resonators, which may also be used in a cascaded configuration to reach narrower pass-bands [32, 46, 47, 48, 49, 50, 51]. Although these techniques have shown impressive results, reaching sub-GHz passbands in narrowband optical filtering schemes remains a challenge. Indeed, it is very challenging to manipulate the frequency content of a signal with a high frequency resolution and low loss, as required in this case to separate the signal frequency components from the noise content (bandpass filtering), limiting the passband of state-of-the-art commercial optical filters to about 5 GHz. Secondly, even if an ultra-narrow filter is successfully conceived, one then has to ensure that the filter can somehow track any drift in the carrier frequency of the signal. Indeed, some form of active stabilization is required in order to ensure that the signal does not drift outside of the passband, which would result in distortion or overall loss of the signal. Alternatively, effective filtering of narrowband optical signals with resolutions down to the MHz level has been demonstrated using Stimulated Brillouin Scattering (SBS). This nonlinear effect consists of amplifying a very narrow spectral range, ideally matching the bandwidth of the signal under test (SUT) [52, 53, 54, 55, 56], and this method has also been shown in combination with narrowband filtering from a ring resonator [57]. With SBS-based approaches, the problem associated with the carrier signal drifting out of the passband is fundamentally circumvented by the principle behind SBS, which employs a seed laser from the initial signal as a pump for the amplification stage. Thus, problems with central frequency drifts are avoided since the pump signal should theoretically undergo the same drifts as the SUT. This however raises the important issue that such a seed signal might not be available, particularly concerning the general problem of weak signal detection from an unknown source.

Broadband signals, on the other hand, come with their own different set of challenges. These signals are commonly used in high-resolution temporal measurements, such as for light-in-flight imaging [58] and for the investigation of the ultra-fast processes that take place in chemical and biochemical processes [6, 7]. Broadband signals are also essential in high-bandwidth telecommunications [59, 60, 61, 62], radio-astronomy [63, 64, 65, 66, 67], spectroscopy [68],and has found novel applications in probing biological tissues [13, 69]. A bandpass filter can still be used to eliminate noise outside the bandwidth of the SUT, but the main hurdle for noise mitigation of broadband waveforms is due to an important presence of noise contained within the bandwidth of the SUT, the so-called in-band noise. Methods to mitigate this type of noise are scarce, mostly relying on digital signal processing methods (DSP) that were developed through research in electroencephalogram (EEG) signal processing [70], speech recognition [71, 72], image processing [73], and mechanical monitoring [74, 75]. However these solutions rely on post-processing methods which are ill-suited for aperiodic, non-repetitive waveforms, and which are particularly not suitable for ultra-fast waveforms, where the digitalization step is an important obstacle for this approach [76]. Recently, there

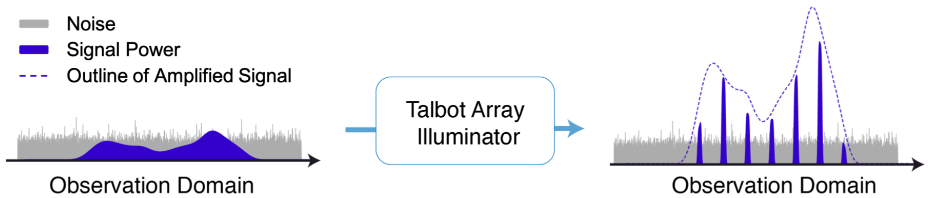

Fig. 1.2 – Denoising amplifier concept.

has been efforts to mitigate in-band noise directly in the analog domain, employing methods such as spatio-spectral filtering [77] and matched filter [78], however these methods require key information about the signal, such as its central frequency, bandwidth and shape, to which the apparatus must be carefully calibrated to. Another method based on spectral cloning has also been proposed [19, 79, 80] to detect the presence of a signal, but it is ultimately unable to reconstruct the waveform to extract information about it. In conclusion, there is currently neither method suited for the detection of ultrafast waveforms buried under in-band noise, nor ways to improve the quality of a signal corrupted with in-band noise in the analog domain which does not require key information about the signal, such as central frequency or spectral distribution.

1.2 Presentation of thesis objectives

Thus, when faced with a weak, noisy signal of unknown properties, an amplifier that would act only on the signal of interest while leaving the noise untouched would be a very useful signal processing apparatus. Such a denoising amplifier would function simultaneously as an amplifier and a noise suppressor, thereby increasing the SNR of a signal. Furthermore, it should function on-the-fly, directly in the analog wave domain, avoiding the requirement for post-processing, and should be able to handle either narrowband or broadband signals, which each have their own particularities.

The development of such a system has been the objective of my degree. The concept we developed is based on linear wave manipulations, dispersion and phase modulation, such that it can be described by simple Fourier operations applicable to general wave systems, here demonstrated in the optical domain. In particular, it is based on the Talbot Array Illuminator (TAI), a special case of the broader self-imaging phenomenon known as the Talbot effect. The idea presented here consists of focusing the energy of a signal into a series of peaks following the input waveform, effectively implementing a lossless sampling process, see Fig. 1.2. Thus, since the energy is conserved in the process, the output peaks outline an amplified version of the input signal. It is important to note that the energy of the output waveform is the same as that of the input (i.e., the integral remains unchanged). This is why we refer to this process as passive amplification, in contrast to active amplification where external energy is injected into the signal. Furthermore, since this focusing phenomenon relies on specific phase relations, only the coherent (or 'phase stable') part of the waveform will undergo this process, while the noise is left untouched. Indeed, the distinction of the phase behaviour of the SUT compared to the noise is the key idea behind the noise mitigation process. By performing this focusing effect in the time domain, a phenomenon analogous to lossless sampling occurs, enabling efficient denoising amplification for narrowband signals. Alternatively, the system can easily be reconfigured to instead work in the spectral domain, where instead it is the spectrum of a waveform that is transformed into a series of peaks. This approach allows for in-band noise mitigation and is suited to broadband, ultrafast waveforms. This concept is demonstrated here on optical waves in the infrared region near 1550 nm, using telecommunication components. It is important however to note that, since this method simply consists of wave manipulations described by Fourier theory, it could potentially be translated to any wave system where the operations of dispersion and phase modulation are possible. Thus, the proposed scheme could potentially be applied to any measurement platform, which includes the entire electromagnetic spectrum [81], along with more exotic systems, such as in quantum matter waves [82, 83, 84, 85, 86], plasmonics [87, 88] and acoustics [89].

The outline of this thesis is as follows; in Chapter 2, I will give a description of the background concepts used in this dissertation. I will first review the mathematical description of wave dynamics, including dispersion and phase modulation, which serve as the basic tools in the field of temporal imaging. The basic concept behind the Talbot effect is then covered, both in the temporal and spectral domains. This Chapter finishes with an important theoretical discussion on the phase relations that occur in the Talbot effect. Chapter 3 then uses these concepts to describe a Talbot amplifier for periodic waveform. These ideas are then extended for amplification of aperiodic waveforms, the central concept of this thesis, using a technique based on the Talbot Array Illuminator (TAI). The specific implementation of the TAI in both domains is then discussed in details, allowing for either narrowband or broadband signal processing. In chapter 4 and 5, experimental results are given for the retrieval of narrowband and broadband signals buried under noise, respectively. This thesis then concludes with chapter 6, with additional recent conceptual extensions of the ideas presented in this thesis.

Chapter 2

Background Concepts

Basic aspects of light propagation are considered, leading to a description of the physical mechanisms behind the phase manipulations that give rise to the Talbot effect, namely dispersion and temporal phase modulation.

2.1 Light and basic wave dynamics

A beam of light is a radiating electromagnetic (EM) wave produced by moving electrically charged objects, such as electrons or protons [81]. This radiation may be modelled quantum mechanically in terms of particles called photons, or classically in terms of wave mechanics. In the later approach, much of the theory describing a harmonic oscillator also accurately describes the dynamics of EM waves. Combined with Fourier theory, light has proven to be a very versatile medium for signal processing.

Fundamentally, the energy $\mathcal{E}$ of a photon is closely related to its frequency, by the famous law

$$\mathcal{E} = h\nu, \tag{2.1}$$

where h is Planck's constant and ν is the linear frequency (or simply frequency) of the wave, describing the number of cycles per second at which the EM waves oscillate. In accordance with

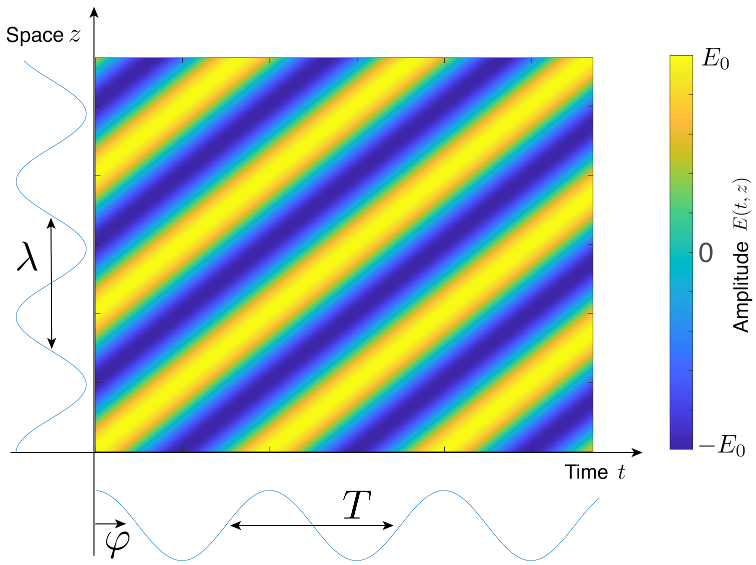

Fig. 2.1 – 2D depiction of a wave in space and time. The slope of the points of equal amplitudes corresponds to the phase velocity of the wave, $c = \lambda/T = \omega/\beta$.

the phasor representation of oscillatory motion, the frequency is often instead expressed in radian per second, giving the angular frequency $\omega = 2\pi\nu$. When considered in the temporal domain, such a wave represents an oscillation in time with a duration given by the period, $T = 2\pi/\omega$ (see Fig. 2.1). Considering an ideal 1D monochromatic EM wave (i.e., a single frequency plane wave) propagating in the z direction, it will travel through vacuum at a velocity $c_0 = 299792458$ m/s, and is mathematically denoted as

$$\begin{aligned} E(t,z) &= E_0 \mathrm{Re}\left\{e^{i(\omega t - \beta z + \varphi)}\right\} \\ &= E_0 \cos(\omega t - \beta z + \varphi), \end{aligned} \tag{2.2}$$

where E_0 is the amplitude of the wave, φ is its phase, simply corresponding to an overall temporal shift of the wave, and β is the propagation constant, related to the wavelength by $\beta = 2\pi/\lambda$[1] (see Fig. 2.1). Thus, the period and frequency describe the oscillations of the wave through time, while the wavelength and propagation constant describe the oscillations through space. These quantities are then related to each other by the dispersion relation of the wave, $\beta(\omega)$.

[1]Note that the wavenumber k is typically used for the propagation constant in general, in 3D. Here, since we will restrict ourselves to waveguide propagation, we use the variable β, in accordance with convention for waveguide propagation, and will restrict any spatial consideration to 1D, in the direction of propagation

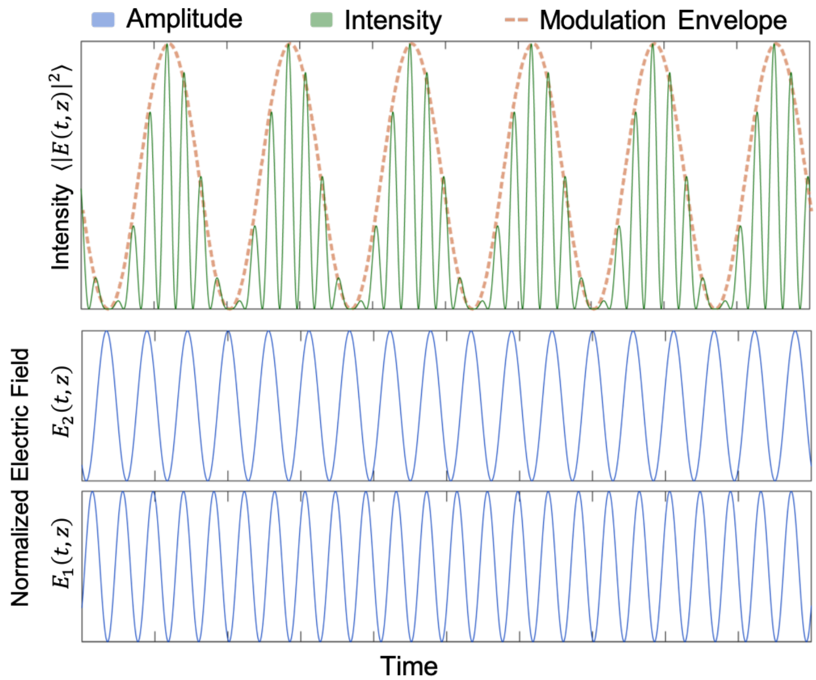

Fig. 2.2 – Phase velocity and group velocity. The harmonics propagate at the phase velocity, while the modulation travels at the group velocity.

$$\begin{aligned} T &\overset{1/2\pi}{\longleftrightarrow} \omega && \text{Time variables} \\ \lambda &\overset{1/2\pi}{\longleftrightarrow} \beta && \text{Space variables} \\ \lambda &= \frac{2\pi}{\beta(\omega)} && \text{Dispersion relation} \end{aligned} \tag{2.3}$$

In vacuum, the dispersion relation is linear and all frequencies travel at the speed of light, $c_0 = \omega/\beta_0 = \omega\lambda_0/2\pi$. In any material however, the phase velocity is reduced and varies as a function of the frequency. The propagation variables are thus scaled by the index of refraction $n(\omega)$;

$$c = c_0/n(\omega), \quad \lambda = \lambda_0/n(\omega), \quad \beta = \beta_0 n(\omega). \tag{2.4}$$

Indeed, it is important to note that the frequency ν of a wave is not altered by propagating in a given medium. Rather, its wavelength is shortened, meaning that within an optical cycle, it travels less distance, such that the wave propagates slower than in vacuum.

An important aspect of propagation through media is that the phase velocity of a wave depends on the frequency of the different components. Given a wave packet composed of several harmonics, it is of interest to know how different harmonics of an electromagnetic wave will travel compared to the propagation speed of the wave energy.

To this end, consider an electric field $E(t, z)$ composed of two harmonic waves of unity amplitude $E_1(t, z)$ and $E_2(t, z)$, with frequencies ω_1 and ω_2 and propagation constants $\beta_{0,1}$ and $\beta_{0,2}$. The propagation of such an electric field is described by

$$\begin{aligned} E(t, z) &= E_1(t, z) + E_2(t, z) \\ &= \cos(\omega_1 t - \beta_{0,1} z) + \cos(\omega_2 t - \beta_{0,2} z) \end{aligned}$$

By equating the argument of each cosine to zero and solving for z/t, we find both phase velocities,

$$c_1 = \omega_1/\beta_{0,1}, \quad c_2 = \omega_2/\beta_{0,2}. \tag{2.5}$$

If instead we calculate the power of the EM wave, which is proportional to $|E(t, z)|^2$, we find

$$\begin{aligned} |E(t, z)|^2 &= \cos^2(\omega_1 t - \beta_{0,1} z) + \cos^2(\omega_2 t - \beta_{0,2} z) + 2\cos(\omega_1 t - \beta_{0,1} z)\cos(\omega_2 t - \beta_{0,2} z) \\ &= \cos^2(\omega_1 t - \beta_{0,1} z) + \cos^2(\omega_2 t - \beta_{0,2} z) + \\ &\qquad \cos[(\omega_2 - \omega_1)t - (\beta_{0,2} - \beta_{0,1})z] + \cos[(\omega_2 + \omega_1)t - (\beta_{0,2} + \beta_{0,1})z], \end{aligned}$$

where we have used the trigonometric identity $\cos u \cos v = 1/2[\cos(u - v) + \cos(u + v)]$. By taking the average, we can take the high frequency components as going to 1, such that the low frequency component comes out as a slow modulation

$$\langle |E(t, z)|^2 \rangle = 1 + cos[(\omega_2 - \omega_1)t - (\beta_{0,2} - \beta_{0,1})z]. \tag{2.6}$$

This corresponds to an envelope traveling at a velocity

$$c_{1,2} = (\omega_2 - \omega_1)/(\beta_{0,2} - \beta_{0,1}) \tag{2.7}$$

Thus, the speed of light is equivalent to the phase velocity of a single harmonic in vacuum since it describes the velocity of a particular point of the sinusoid, or phase, as it propagates through space. As multiple frequency components are combined, this leads to the formation of an envelope function (see Fig. 2.2). These wave packets travel at this different velocity, called the group velocity since it is composed of a group of waves [90]. Formally, we can generalize the group velocity to a continuum of frequencies, as it is usually defined. We may define the group velocity by considering a function $a(t)$, consisting of a complex envelope $w(t)$ multiplied by a carrier signal at frequency ω_0,

$$a(t) = w(t)e^{i\omega_0 t}, \tag{2.8}$$

where from here and thereafter, we drop the spatial dependence of the signals, restricting us to the case of temporally varying signals measured at a single point in space, as it is typically the case in signal processing. In the spectral domain, this waveform consists of a continuum of frequencies centered at ω_0, with an envelope given by the Fourier transform, $W(\omega) = \mathscr{F}\{w(t)\}$, and it is defined as

$$A(\omega) = W(\omega) * \delta(\omega - \omega_0), \tag{2.9}$$

where $*$ denotes a convolution and δ is the Dirac delta function. This wave packet will thus propagate at the group velocity $c_g(\omega)$ defined as

$$c_g(\omega) = \frac{d\omega}{d\beta}, \tag{2.10}$$

whose inverse, multiplied by the distance travelled z_0, gives the group delay, $\tau_g(\omega) = z_0/c_g(\omega) = z_0\frac{d\beta}{d\omega}$ [91, 92]. As a rule of thumb, it is useful practically to know that the speed of light of a

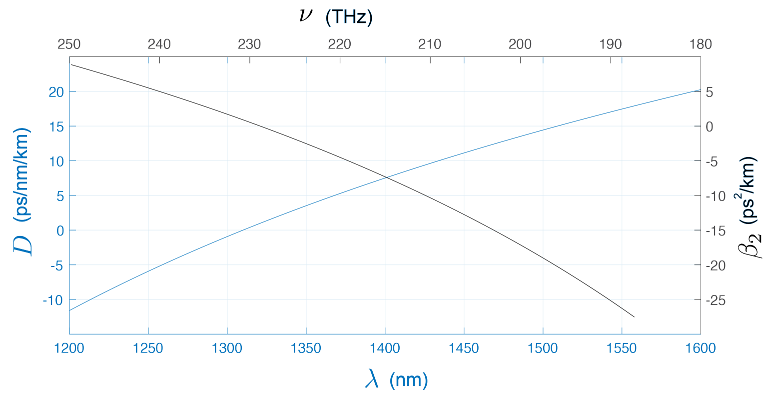

Fig. 2.3 – Dispersion characteristics of SMF fiber.

waveform centered at 1550 nm, in single mode optical fiber ($n = 1.46$), is approximately equal to 205,337,300 m/s$\approx 2 \times 10^8$ m/s, such that it takes the light 5 ns to travel 1 m of fiber.

From here and thereafter, we note that all waveforms will be given on a time axis corresponding to the retarded time, t_{ret}, instead of some absolute time axis t_{abs}, which is defined as

$$t \leftarrow t_{ret} \tag{2.11}$$

$$t_{ret} = t_{abs} - \tau_g(\omega_0). \tag{2.12}$$

In other words, this means that all time axes are given with reference the group delay at the centre of the waveform, which depends on the central frequency ω_0 of the signal. This is done to simply consider changes in the shape of the waveform, regardless of its speed of propagation. In a way, we stay the frame of reference of the waveform itself, both in space and time.

2.1.1 Dispersive propagation

As mentioned above, the equation relating the frequency of a wave to its propagation constant is called the dispersion relation. If this equation is linear, such that $\omega \propto \beta$, then the group velocity and phase velocities are equal, and any waveform will travel through such medium undistorted since all frequency components travel at the same velocity. If the dispersion relation is instead quadratic, this indicates that the group velocity varies linearly with frequency. Physically, this effect is called Group Velocity Dispersion (GVD), and causes different spectral components of a given waveform to propagate at different velocities, typically resulting in broadening and distortion. This property of a material is characterized by the second order dispersion coefficient β_2

$$\beta_2 = \frac{d\tau_g}{d\omega}, \tag{2.13}$$

which characterizes the amount of dispersion accumulated per distance of propagation [93], is typically given in units of ps^2/km. Alternatively, this property may be denoted by the dispersion coefficient D, defined as

$$D = \frac{d\tau_g}{d\lambda}, \tag{2.14}$$

which has units of ps/nm/km, and is related to β_2 by

$$\beta_2 = -\frac{\lambda^2}{2\pi c} D. \tag{2.15}$$

To account for the overall effect caused by a dispersive propagation, we also define the total dispersion $\ddot{\phi} = \beta_2 z$ as the total amount of dispersion accumulated by a dispersive propagation. Dispersion occurs naturally in practically all dielectric materials. The dispersion characteristics of SMF-28 fiber optic cable, by Corning® [94], is shown in figure 2.3. Wavelengths below 1310 nm ($\sim$228.8 THz), where β_2 is positive ($D < 0$), are said to exhibit normal dispersion, such that slower frequencies (red) travel faster. Conversely, wavelengths above 1310 exhibit anomalous dispersion ($\beta_2 < 0$, $D > 0$), and higher frequencies travel faster. This is the case for signals in the C-band, the wavelength range from 1530 nm to 1565 nm which is used in optical telecommunications due to the low loss of fiber optic cable and high gain of EDFAs in this region. In particular, SMF fiber causes about 17 ps^2/km of dispersion around 1550 nm.

Dispersive effects may also be derived by a simple Taylor series expansion of the propagation constant about the frequency ω_0 at which the pulse spectrum is centered,

$$\beta_i = \left.\frac{d^i \beta(\omega)}{d\omega^i}\right|_{\omega=\omega_0}, \tag{2.16}$$

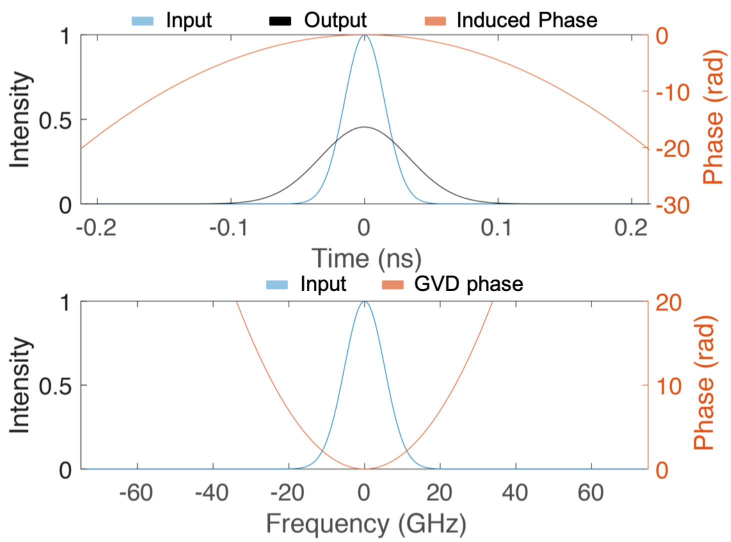

Fig. 2.4 – Temporal broadening caused by dispersive propagation.

where the zeroth term scales the phase velocity, the first term is related to the group delay, and the second term for group velocity dispersion[2]. Higher order dispersion coefficients $\beta_3, \beta_4, ...$ are relevant near the 0 dispersion point of the material, and are of interest in non-linear optics and for ultrafast pulse generation, where ultra-wide bandwidths waveforms and supercontinuums are generated. These are however out of the scope of the present thesis, and we employ the so-called narrowband approximation, such that all higher-order dispersion coefficients are neglected.

As will be further described in chapter 3, dispersion plays an important role in the Talbot effect. Since, in some case, high amounts of dispersion are required, specialized equipements such as Linearly Chirped Fiber Bragg Gratings (LCFBG) are employed to reach a specific amount of dispersion. Thus, dispersions equivalent to hundreds of kilometers of fiber, which would result in 100 dB of loss using standard SMF, may be reached with attenuations below 3 dB using LCFBG with lengths on the order of a few centimeters to meters long [95, 96, 97].

To conclude this section, let us explicitly investigate the effect of dispersion on a Gaussian pulse of the form

$$g(t) = \frac{1}{\sigma\sqrt{2\pi}} e^{\frac{t^2}{2\sigma^2}}, \tag{2.17}$$

[2] In the literature, the terms dispersion, second order dispersion, group velocity dispersion, group delay dispersion and chromatic dispersion are often used interchangeably.

where σ is the standard deviation, related to the full-width at half maximum (FWHM) by $\text{FWHM} = 2\sqrt{2\ln 2}\sigma$. Since dispersion is a unitary operation, because it preserves the amplitude of a waveform and only alters the phase, it acts as a transparent filter. Thus, as with any phase modulation for a given domain, chromatic dispersion effect is modeled by multiplication by a complex exponential with some argument $\phi(\omega)$;

$$\mathcal{H}(\omega) = e^{-i\phi(\omega)}. \tag{2.18}$$

In particular, group velocity dispersion (GVD) can be accounted by a quadratic spectral phase of the form

$$\mathcal{H}_{\text{GVD}}(\omega) = e^{-i\frac{\ddot{\phi}\omega^2}{2}}. \tag{2.19}$$

The Fourier transform of a Gaussian pulse is also a Gaussian in the spectral domain, $G(\omega) = e^{-\frac{\omega^2\sigma^2}{2}}$, so we can calculate the waveform after a dispersive propagation with total second order dispersion $\ddot{\phi}$ by multiplication of the dispersive propagator, eq. 2.19, in the associated Fourier domain, giving the dispersed waveform $\tilde{g}(t)$

$$\begin{aligned} \tilde{g}(t) &= \mathscr{F}^{-1}\left\{\mathcal{H}_{\text{GVD}}(\omega)G(\omega)\right\} \\ &= \mathscr{F}^{-1}\left\{e^{-i\frac{\ddot{\phi}\omega^2}{2}}e^{-\frac{\omega^2\sigma^2}{2}}\right\}, \end{aligned} \tag{2.20}$$

where $\mathscr{F}^{-1}$ denotes the inverse Fourier transform (see Fig.2.4). In this case, the resulting waveform can be analytically derived, as shown in [93]. However, the resulting waveform must often be solved numerically. The effect caused by dispersion is mathematically equivalent to that of paraxial diffraction, as formally described by the space-time duality [98]. In this approach, both paraxial diffraction and narrowband dispersion can be modelled as complex diffusion equations, sharing similarities with thermal diffusion, such that 'sharper' peaks spread out at a faster rate than 'smoother ones'.

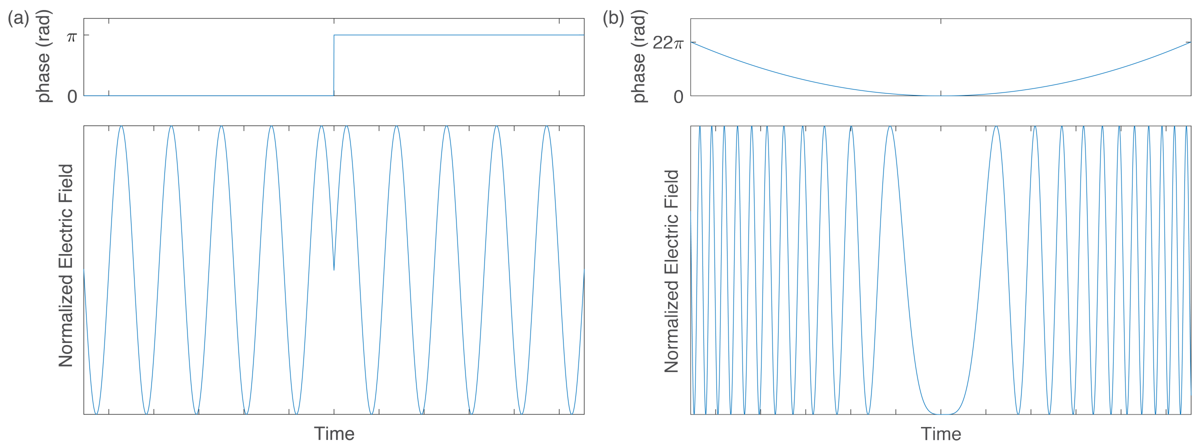

Fig. 2.5 – Temporal phase modulation. (a) a step in phase modulation will lead to a discontinuity in the field. (b) a quadratic phase modulation leads to the formation of a continuum of frequencies, as shown here in the temporal domain.

2.1.2 Temporal phase modulation

A similar phenomenon can also be realized in the temporal domain, and is referred to as a time lens [98, 99]. Whereas dispersion causes different frequency components to travel at different velocities as a result of a quadratic spectral phase modulation, a time lens is achieved by varying the temporal phase φ of a wave quadratically. Generally, temporal phase modulation according to $\varphi(t)$ is accounted for by a multiplication in the time domain by the propagator

$$h_{\mathrm{TPM}}(t) = e^{i\varphi(t)}. \tag{2.21}$$

Graphically, a wave that undergoes a sudden phase shift will simply appear to have a discontinuity in its carrier wave (see Fig. 2.5). Experimentally, this can be achieved using an electro-optic Phase Modulator (PM) based on the Pockel's effect [100, 101]. It is important to note that phase modulation can be achieved by other means, in particular with non-linear effects such as self-phase modulation or cross-phase modulation (XPM). With such approaches, it is usually possible to achieve larger phase swings and higher bandwidth phase modulation signals, but these methods are not as versatile and easy to implement as compared to an electro-optic PM.

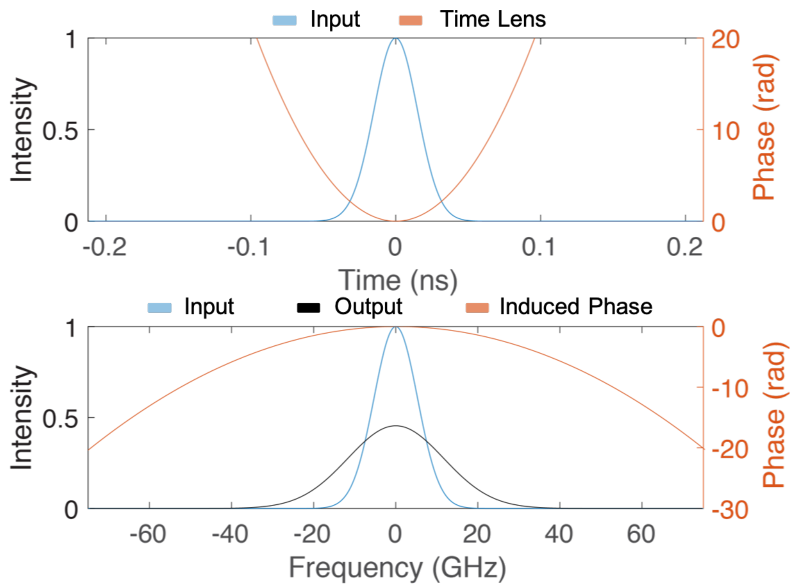

Fig. 2.6 – Spectral broadening caused by quadratic temporal phase modulation.

To illustrate its analogy with dispersion, let us once again consider a Gaussian function, described by equation 2.17. We can model a time lens with a propagator of the form

$$h_{\mathrm{TL}}(t) = e^{i\frac{\varphi_0}{2}t^2}, \tag{2.22}$$

where φ_0 is a constant that describes the strength of the modulation. Experimentally, in the context of electro-optic phase modulators, this parameter depends on the applied voltage and other characteristic of the modulator [101]. The resulting spectrum $\tilde{g}(\omega)$ following such quadratic phase modulation is calculated as [93]

$$\begin{aligned} \tilde{g}(\omega) &= \mathscr{F}\left\{h_{\mathrm{TPM}}(t)g(t)\right\} \\ &= \mathscr{F}\left\{e^{i\varphi_0 t^2}\frac{1}{\sigma\sqrt{2\pi}}e^{\frac{t^2}{2\sigma^2}}\right\}. \end{aligned} \tag{2.23}$$

The similarity in the operations of dispersion and time lensing is now apparent, graphically demonstrated with Fig 2.6.

This time-frequency duality (also called Fourier duality) allows for many interesting phenomena discovered in one domain to be directly carried out to the other. This duality appears for example, in the correspondence between pulse compression [99, 102] and bandwidth compression [103], time-to-frequency mapping [104, 105, 106, 107], frequency-to-time mapping [108, 109, 110], etc. As shown in the next section, the Talbot effect is no exception to this rule.

2.2 The Talbot effect

The Talbot effect was first observed by the British scientist William Henry Fox Talbot, in 1837 [111]. When examining diffraction gratings under white light illumination with a magnifying lens, he observed that images of the grating reappeared a specific distances, even when he moved the lens out of focus. The phenomena, also called self-imaging effect, was then described in the temporal domain by Jannson and Jannson in 1981 [112], and was found to be an efficient way to increase the repetition rate of pulse train [113, 114]. These concepts were then further extended to the spectral [115] and angular domains [116] by José Azaña. Since then, the Talbot effect has been carried out from optics to other wave systems, such as plasmonic waves [87], X-rays [117], and matter waves [85], amongst others.

Here I present the basic theory behind the Talbot effect for repetition rate multiplication in the time domain [113, 114], and for frequency comb division in the spectral domain [115]. I will then formalize the generality of this effect in section 2.2.3, and proceed with a description of the phase relation of the Talbot images in section 2.3, which allows for the realization of a Talbot amplifier for periodic waveforms, the main subject of Chapter 3. This lays the theory to describe the Talbot Array Illuminator (TAI), the concept employed for Talbot amplification of arbitrary waveforms.

2.2.1 Temporal Talbot effect

Consider the intensity profile $I(t)$ of a signal consisting of a repeating waveform $f(t)$ with period t_r,

$$I(t) = \sum_{n=-\infty}^{+\infty} f(t - nt_r), \tag{2.24}$$

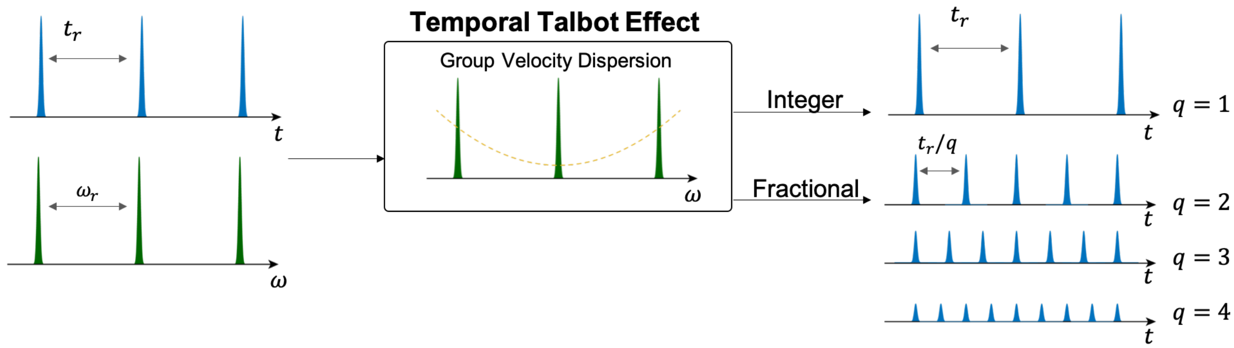

Fig. 2.7 – Temporal Talbot effect.

where $f(t)$ is centered around $t = 0$ and extends over a temporal duration $<< t_r$. Such a function will have a Fourier representation consisting of a series of lines, spaced by a spectral period $\omega_r = 2\pi/t_r$. The temporal Talbot effect occurs when this periodic waveform travels through a dispersive medium with a total second-order dispersion coefficient $\ddot{\phi}$ satisfying

$$\ddot{\phi}_{p,q} = \frac{2\pi}{\omega_r^2}\frac{p}{q}, \tag{2.25}$$

where p and q are mutually-prime natural numbers (i.e., p/q is an irreducible fraction). If $q = 1$, such the total dispersion satisfies the relation

$$\ddot{\phi}_{p,1} = \frac{2\pi}{\omega_r^2}\frac{p}{1}, \tag{2.26}$$

then the initial waveform is recovered exactly without distortion, as if it had not experienced any dispersion (see Fig. 2.7). Under these conditions, the recovered waveform is referred to as an integer Talbot image[3].

As depicted in Fig. 2.8, for even values of p (i.e., $\{p, q\} = \{2, 1\}$), the image is recovered exactly as in equation 2.24, whereas for odd values of p (i.e., $\{p, q\} = \{1, 1\}$), the obtained integer Talbot image is shifted by a half-period. These two cases are referred to as exact integer Talbot images

[3]The terms fundamental Talbot image and self-image are also used for this purpose.

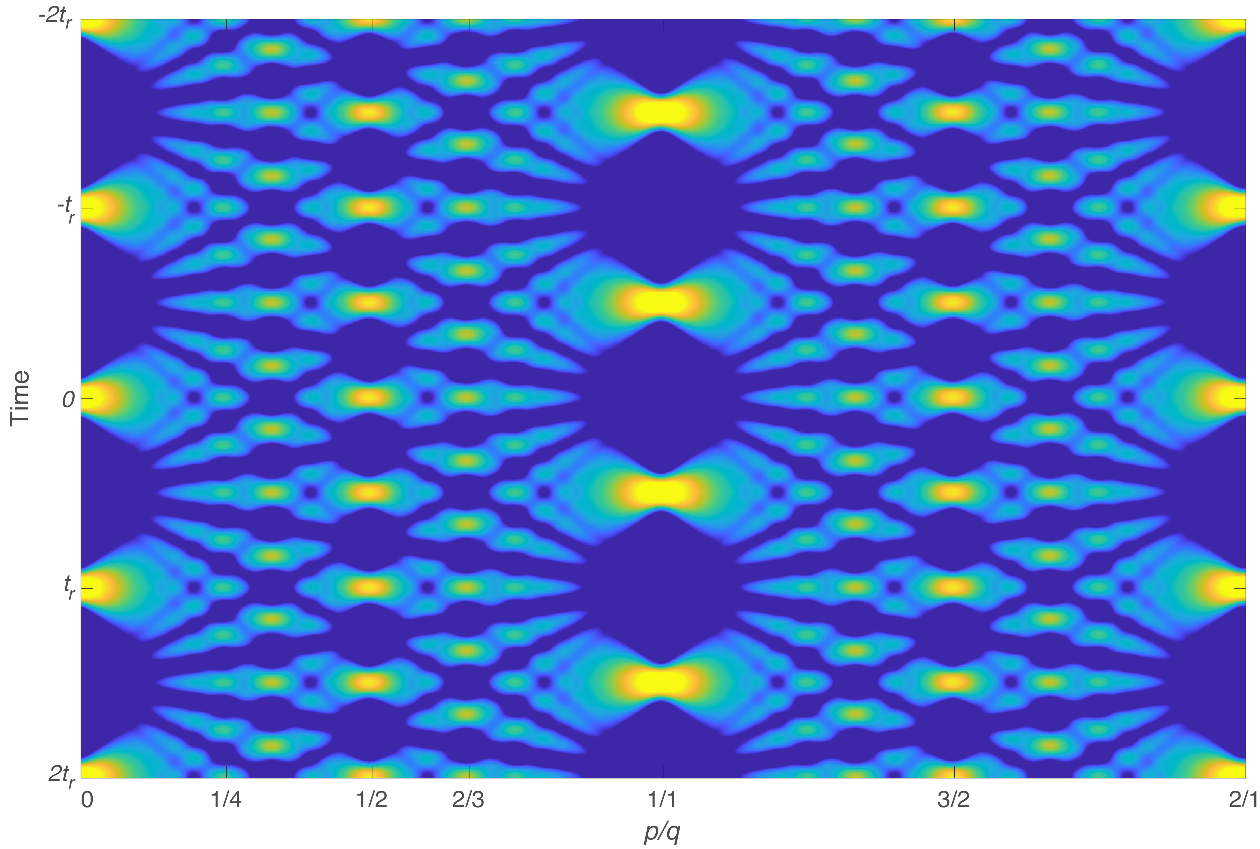

Fig. 2.8 – The Talbot carpet shows the evolution of a 1D temporal signal (y axis) as it propagates through increasing amounts of GVD, where $\ddot{\phi}$ is given in terms of the Talbot integers $p/q = 0, 1/4, 1/3, ..., 2/1$

and inverted integer Talbot images, respectively. In reference to the spatial effect, one may define the Talbot length,

$$\ddot{\phi}_{2,1} = \frac{4\pi}{\omega_r^2}, \tag{2.27}$$

which corresponds to the amount of dispersion between two exact fundamental Talbot images[4]. In the context of optics, the integer Talbot effect has found application for clock recovery [119] and has been shown to mitigate distortion from amplitude and timing jitter [120, 121, 122, 123, 124]. The integer Talbot effect has also been used to avoid the need for dispersion compensation modules for transoceanic transmission of pulse trains by having the total fiber length respect an integer Talbot condition [125].

[4]Note that in the literature, the Talbot length is sometimes given as half of this value. Here we follow the given convention so that the pattern repeats periodically with the Talbot length, with no phase or time shift difference [118].

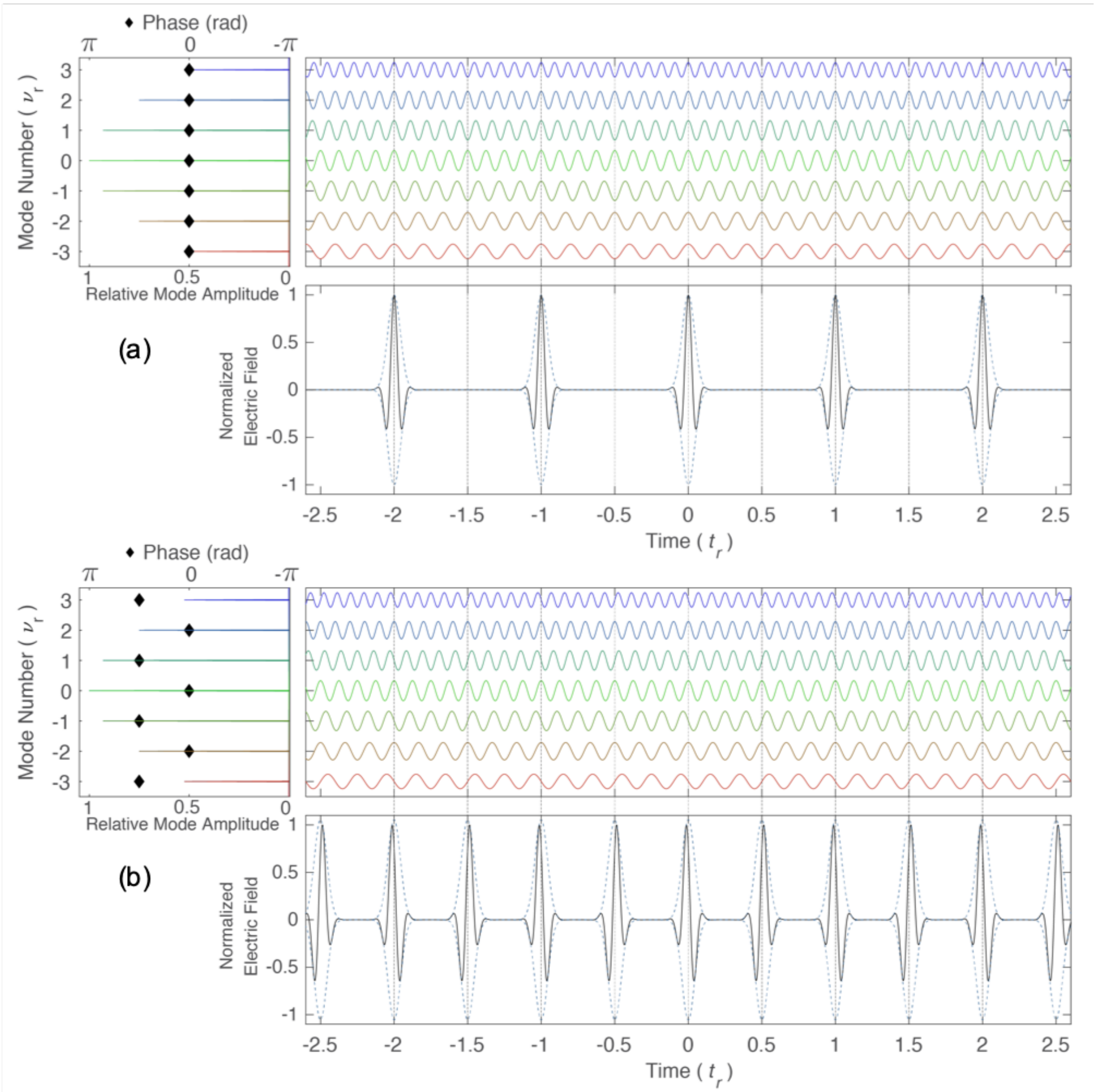

Fig. 2.9 – Phase variation of a fractional Talbot image. (a) When all the spectral modes are in phase, the spectral period is given exactly by the Fourier inverse of the temporal period, $\omega_r = 2\pi/t_r$. (b) When the spectral phases acquired through dispersive propagation satisfy a Talbot condition for given integers p and q, the spectral modes are realigned in such a way that the temporal period is divided by a factor q, and the exact form of the induced phase depends on the phase factor p. Note that both temporal signals are normalized to 1 to make the phase variation more visible. As mentioned above, the period-reduced signal has an intensity reduced by the same factor, $q = 2$ in this case.

On the other hand, if the total dispersion satisfies eq. 2.25 with $q > 1$, the pulse train will be recovered with a period reduced by a factor q [113, 114];

$$I_q(t) = \frac{1}{q} \sum_{n=-\infty}^{+\infty} f(t - n\frac{t_r}{q}). \tag{2.28}$$

These images can be observed in the Talbot carpet between the integer Talbot images (Fig. 2.8). This case is called fractional Talbot effect, and due to energy conservation, each pulse will also be decreased by a factor q, assuming loss-less propagation (See Fig. 2.7). The fractional Talbot effect has been shown as an efficient method to increase the repetition rate of pulse trains [113, 114]. One should also keep in mind that dispersion implies a phase-only operation in the spectral domain; thus, the intensity profile of the spectrum is unchanged.

A important aspect of fractional Talbot images is that the resulting waveform exhibits a deterministic phase variation. This can be explained by the mode decomposition, as shown in Fig 2.9. Alternatively, this phase variation may also be understood from the fact that the different output pulses occur at different path lengths with respect to the initial pulses[5]. These phases are primordial in the realization of a Talbot amplifier, and will be treated in further details in section 2.3.

2.2.2 Spectral Talbot effect

As discussed at the end of section 2.1.2, there exists a duality between dispersive propagation and quadratic temporal phase modulation (i.e., a time lens). This duality also extends to the Talbot effect, and was exploited by José Azaña to postulate the spectral Talbot effect in 2005 [115]. The experiment was done using frequency combs, which are waveforms characterized by a collection of equally-spaced discrete spectral lines, separated by a spectral period ν_r, called the free spectral range (FSR). The FSR is reciprocal to the period of the temporal waveform, $t_r = 1/\nu_r$. Although any periodic waveform could loosely be referred to as a frequency comb, since they consist of a collection of discrete spectral components in the Fourier domain, the term is reserved for signals where the repetition rate and absolute frequency offset are stabilized with a high degree of precision and with very low phase noise. Such signals are particularly useful in high precision metrology [128], atomic and molecular spectroscopy [129, 130], astronomical observation [131], signal processing [132], quantum optics [133] and a myriad of other specialized applications [134].

[5]Indeed, although most of the literature derives the Talbot effects from a Fourier decomposition approach, which relies on the wavy nature of the Talbot effect, it is possible to instead derive it using a path-integral formalism, which can be interpreted as the particle nature of the Talbot effect [126, 127].

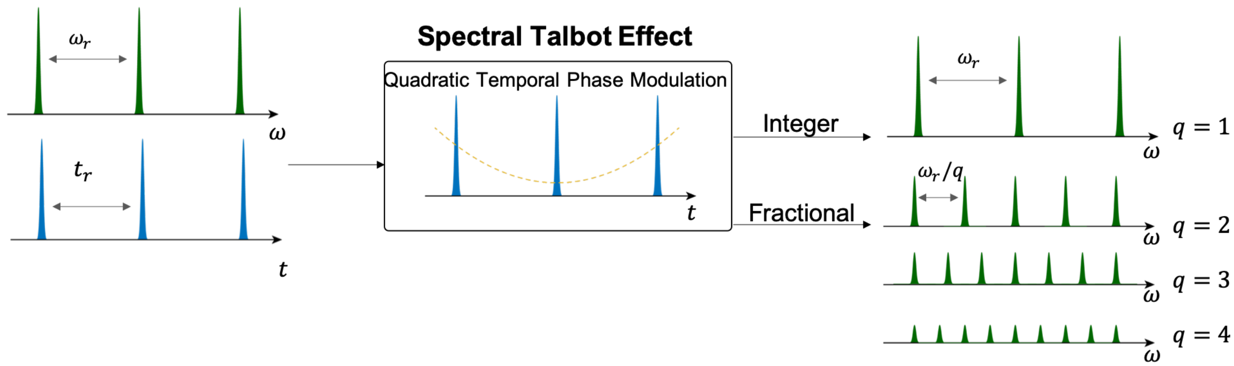

Fig. 2.10 – Spectral Talbot effect.

The spectral Talbot effect occurs when a periodic spectral waveform is affected by a temporal phase modulation operator of the form

$$h_{\mathrm{TL}}(t) = e^{i\frac{\varphi_0}{2}t^2}, \tag{2.29}$$

where the phase modulation coefficient φ_0 satisfies a relation of the form

$$\varphi_0 = \frac{2\pi}{t_r^2}\frac{s}{q} \tag{2.30}$$

where s and q are, again, two mutually-prime natural numbers [115, 135, 136]. Similarly to the temporal Talbot effect described above, Fig. 2.10 describes the effect of different values of the phase modulation coefficient on the input waveform, allowing for FSR division by the integer q. The spectral Talbot effect is evidently analogous to the temporal Talbot effect.

2.2.3 On the generality of the Talbot effect

The discussion at the beginning this chapter mentioned how the Talbot effect was brought from the spatial domain to the temporal domain through the space-time duality, which can be formally described as a mathematical isomorphism between the physics describing narrowband dispersion and paraxial diffraction. It should now be clear that there is also an evident duality between

Observation Domain		Fourier-dual Domain	Propagator	Talbot Condition
Time	t	ω	GVD $\mathcal{H}_{\mathrm{GVD}}(\omega) = e^{-i\frac{\ddot{\phi}\omega^2}{2}}$	$\ddot{\phi} = \frac{2\pi}{\omega_r^2}\frac{p}{q}$
Frequency	ω	t	Time Lens $h_{\mathrm{TL}}(t) = e^{i\frac{\varphi_0}{2}t^2}$	$\varphi_0 = \frac{2\pi}{t_r^2}\frac{s}{q}$
General	u	U	Quadratic Phase $X(U) = e^{i\frac{\Theta}{2}U^2}$	$\Theta = \frac{2\pi}{U_r^2}\frac{p}{q}$

Table 2.1 – Generalized Talbot variables.

time and frequency, two Fourier conjugate domains. This allows for abstraction of the phenomena, regardless of the specific domain of observation [137].

The generalized problem can be described by a representation variable u in any observation domain, which is related to its conjugate Fourier variable U. As usual with Fourier dual variables, a periodic function with period u_r in the Observation domain u has a related period $U_r = 2\pi/u_r$ in its Fourier conjugate domain U. As shown in table 2.1, we can generalize the Talbot effect to any domain of observation as resulting from a propagator in the Fourier-dual domain, $X(U)$, which performs a quadratic phase modulation according to the Talbot condition.

2.3 Discreteness of the Talbot effect and Gauss sums

In the examples shown above, it was implicitly assumed that the signal in the domain affected by the quadratic phase modulation (e.g., the Fourier-dual domain) consisted of a series of very narrow waveforms. Indeed, as shown in the sections 2.1.1 and 2.1.2 on dispersion and temporal phase modulation, if a single waveform is affected by a considerable amount of quadratic phase modulation, this will cause a broadening in the associated Fourier domain. Thus, for the Talbot effect, the phase variation between neighbouring waveforms is significant, but the phase variation within a single waveform must be negligible. Alternatively, to avoid distortions due to non-negligible phase variation within a single waveform, the phase modulation process can be performed in discrete steps [136, 138]. This is particularly useful for the spectral Talbot effect, since it is difficult in practice to achieve time lenses with a large phase swing. The discrete phase levels may easily be extracted from the continuous quadratic phase modulation by taking the values of the propagator at the center of each waveform. The extracted phase values can then be wrapped to a range of 2π, and a periodic phase sequence of q phase levels is recovered (see Fig. 2.11).

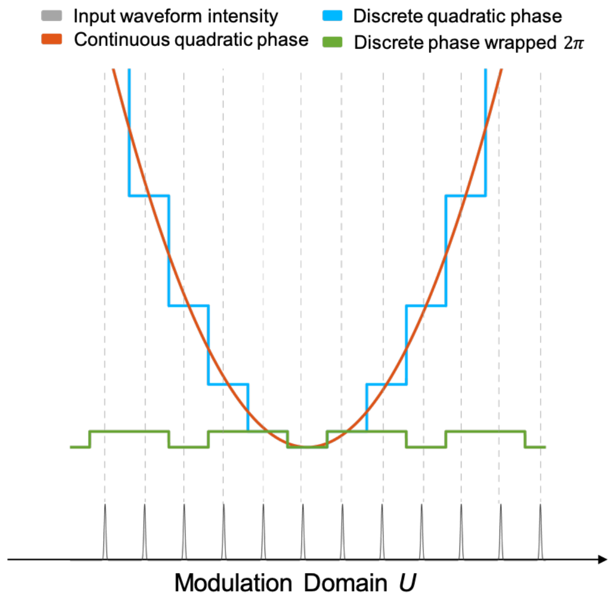

Fig. 2.11 – Continuous and discrete phase modulation equivalence, with $q = 3$.

Interestingly, this alludes to the fact that the Talbot effect is fundamentally a discrete phenomenon, and reduces the problem to one of number theory. Indeed, research on the nature of the Talbot effect has demonstrated that the phase sequences satisfying a Talbot conditions all have a common form, belonging to a family of equations known as Gauss Sums [126, 137, 139, 140, 141]. These sums are ubiquitous in number theory, and they were originally considered by Gauss to prove the law of quadratic reciprocity, a law that gives conditions for the solvability of quadratic equations modulo prime numbers. Gauss himself referred to this proof as the golden theorem [142, 143].

Thus, instead of analyzing the phase dynamics of the Talbot effect with continuous functions, we can instead investigate the phases that occur in the Talbot effect by using a discrete formalism, where each pulse in the observation domain is indexed by an integer n, and label those in the Fourier-dual domain with the integer m. We may then use the Discrete Fourier Transforms (DFT), combined with standard operations from number theory, to derive the induced phase sequence in the observation domain resulting from a phase modulation satisfying a Talbot condition (e.g., in the Fourier-dual domain). In this view, consider a discrete signal x_n, consisting of a sequence of phase levels periodic in the running index n with period q. It can be shown that its DFT pair is given by

$$
\begin{aligned}
x_n \equiv e^{i\theta_n} &= e^{i\sigma_\phi c} \exp\left(i\pi\sigma_\phi \frac{s}{q} n^2\right) \xrightarrow{\text{DFT}} \\
X_m \equiv e^{i\Theta_m} &= \sqrt{q} \exp\left(-i\pi\sigma_\phi \frac{p(1+qe_q)}{q} m^2\right),
\end{aligned}
\tag{2.31}
$$

where $\sigma_\phi = \pm 1$ is simply the sign of the phase pattern, and both n and m are restricted to the integers $0, ..., q-1$ [126, 137, 139, 140, 141]. The integer factors s,p and q are related by

$$
sp = (1 + qe_q) \pmod{2q},
\tag{2.32}
$$

where e_q represents the parity of the integer q, such that $e_q = 0$ when q is even and $e_q = 1$ when q is odd [139]. The constant phase factor $e^{-i\sigma_\phi c}$ is given by

$$
\begin{aligned}
e^{-i\sigma_\phi c} &= \left(\frac{s}{q}\right) e^{i\sigma_\phi \frac{\pi}{4}(q-1)} = \left(\frac{p}{q}\right) e^{i\sigma_\phi \frac{\pi}{4}(q-1)} \quad (q \text{ odd}), \\
e^{-i\sigma_\phi c} &= \left(\frac{q}{s}\right) e^{-i\sigma_\phi \frac{\pi}{4} s} = \left(\frac{q}{p}\right) e^{-i\sigma_\phi \frac{\pi}{4} p} \quad (q \text{ even}).
\end{aligned}
\tag{2.33}
$$

It is worth noting that this phase factor does not alter the shape of the phase sequence, so is not needed in practice. Thus, eq. 2.31 allows us to compute the resulting phase sequence at a fractional Talbot plane. For reference, table 2.2 lists the different values of p for a given s and q. The subject of the phase relations that arise in the Talbot effect has significantly evolved in recent years, and is still an active area of research to uncover further insights into the dynamics of the Talbot images as they evolve through the carpet.

From this discussion, one could therefore argue that the Talbot effect is fundamentally a discrete phenomenon. As mentioned above, this allows to apply a phase modulation in steps rather than in a continuous fashion. Furthermore, the discrete formalism presented here sheds light on the inherent periodicity of the Talbot phases, resulting in the fact that only a finite set of different phase values

		p									
		1	**2**	**3**	**4**	**5**	**6**	**7**	**8**	**9**	**10**
q	**2**	1		3		1		3		1	
	3	4	2		4	2		4	2		4
	4	1		3		5		7		1	
	5	6	8	2	4		6	8	2	4	
	6	1				5		7			
	7	8	4	12	2	10	6		8	4	12
	8	1		11		13		7		9	
	9	10	14		16	2		4	8		10
	10	1		7				3		9	
	11	12	6	4	14	20	2	8	18	16	10

Table 2.2 – Values of the integer s, for corresponding p and q values.

need to be implemented in practice, in contrast to the 'infinite' phase sequence of a continuous phase modulation such as GVD[6]. This is particularly useful for temporal phase modulation, where it is difficult to have arbitrarily long and deep quadratic modulation, limited by the maximum phase swing achievable with electro-optic PM or XPM. It is instead much more convenient to use a radio-frequency (RF) arbitrary waveform generator (AWG), where discrete phase levels can be digitally programmed, and then fed to an electro-optic PM. On the other hand, a continuous spectral phase filter is typically much more convenient than a discrete spectral phase filter, since devices that exhibit large amounts of GVD are relatively easy to design, whereas practical discrete phase filters would require high spectral resolution and would be difficult to reconfigure. In conclusion, there is some form of equivalence between continuous and discrete phase filtering, and when discussing periodic waveforms, the difference is rather unnoticeable because the individual waveforms are usually too narrow to experience any significant dispersion.

[6]Indeed, the periodic nature of the GVD was previously noticed and used to describe a family of equivalent continuous filters [144].

Chapter 3

Talbot Amplification

Talbot amplification of periodic waveforms was first demonstrated in 2014 by Reza Maram on pulse trains in the temporal domain [145]. Hugues Guillet de Chatellus then demonstrated it shortly after in the spatial domain with noiseless amplification of periodic images in 2017 [146, 147], and Luis Romero Cortés demonstrated it in the spectral domain with frequency combs in 2018 [148]. In all contexts, Talbot amplification showed interesting noise mitigation properties, unlike the deterioration caused by conventional active amplification methods, as discussed in Chapter 1. In a so-called Talbot amplifier, the phase operations rely on the phase coherence of the SUT, such that the amplification process leaves random, incoherent noise virtually untouched. This is due to the fact that such noise has rapid intensity and phase variations, such that the phase relation required for Talbot amplification is not satisfied. On the other hand, the coherent SUT is amplified, such that it is possible to recover waveforms heavily distorted by incoherent noise. Interestingly, the idea behind Talbot amplification is closely related to the Talbot Array Illuminator (TAI), a concept that was first shown in the spatial domain by Lohmann in 1988 [118]. Historically, TAI were first employed in the spatial domain as a means to convert a uniform plane wave into many concentrated spots of light of equal intensity, with very little energy loss in the conversion. Its purpose was to provide an array of microstructures with light beams, for example, to supply power to optical parallel processors, or for integrated circuit pattern illumination, possible both in 1D or 2D [118]. More recently, TAI have been used for CW-to-pulse conversion [149] and for both temporal [150] and spectral [151] invisibility cloaking. In the context of image distortion, the TAI's self-healing properties [152] and robustness to defects on gratings [153, 154] have been discussed, however TAIs were never exploited in the context of waveform amplification. Furthermore, although amplification factors up to 27 have been shown on periodic signals in ref. [145], most demonstrations of Talbot amplifiers and TAIs have been limited to factors below 5, due to a combination of the fact that the Talbot phases were not very well understood, due to experimental complexity, and also simply by lack of need for higher amplification factors.

Employing the mathematics described in section 2.3 and using state-of-the-art, yet commercially available components, I show here how the TAI concept can be adapted for amplification of arbitrary signals, alleviating the requirement for periodicity. In particular, when applied in the time domain, the Temporal Talbot Array Illuminator (T-TAI) scheme is suited for noise mitigation of narrowband signals (Chapter 4), whereas in the frequency domain, the Spectral Talbot Array Illuminator (S-TAI) is suited for noise mitigation of broadband signals (Chapter 5). In both cases, amplification factors near 30 are demonstrated, corresponding to the highest amplification ever reached in Talbot amplifiers, which allows for unique noise mitigation capabilities.

3.1 Talbot amplification of periodic waveforms

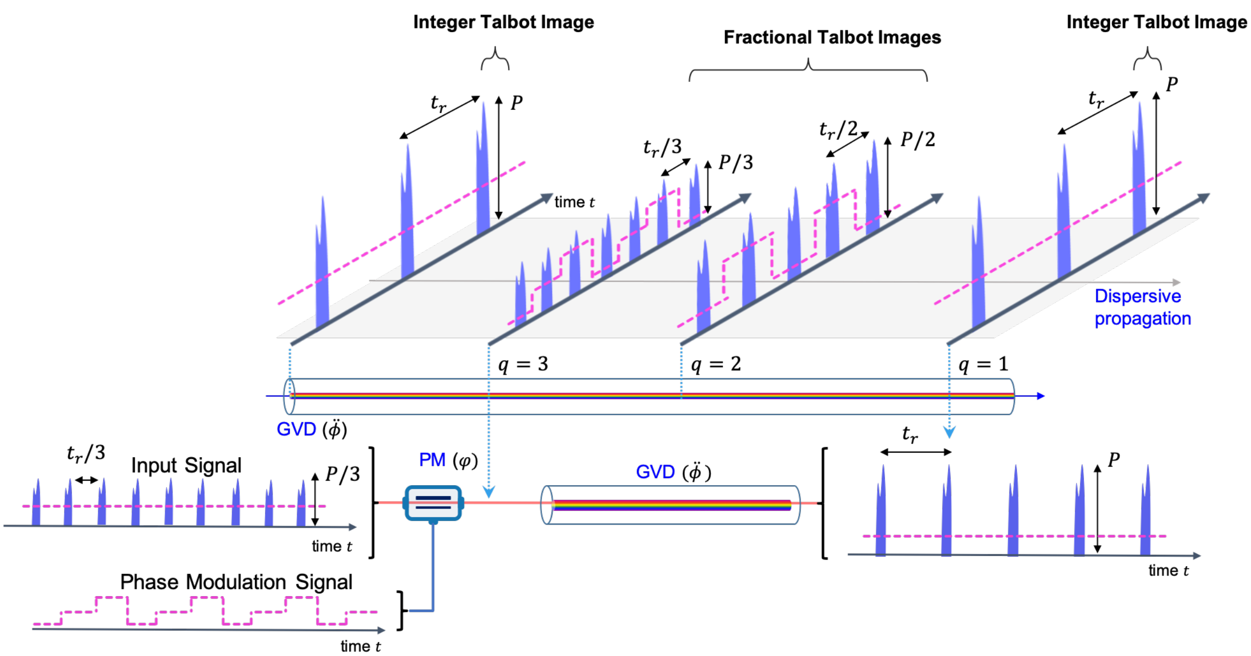

Fig. 3.1 – Talbot amplification of periodic waveforms consists of imposing the phase of a fractional Talbot image, which followed by dispersion, leads to the coherent summation of q peaks. In this figure, this is illustrated by having the signal at $q = 3$ as the input signal, where the phase is imposed using a PM, and then reaching the next integer Talbot image by dispersive propagation.

The easiest way to grasp the concept behind Talbot amplification is unquestionably by visualizing the dynamics within the Talbot Carpet. To briefly summarize, a temporal pulse train propagating through a certain amount of dispersion $\ddot{\phi}$ is modelled by a spectral phase modulation according to the dispersive propagator, eq. 2.19. On the Talbot carpet, this corresponds to a transformation from the initial image at $\ddot{\phi} = 0$ to $\ddot{\phi} = \ddot{\phi}_{p,q}$, where p and q are the integers from the Talbot condition for dispersive propagation (eq. 2.25). The resulting temporal Talbot image will thus have a period and peak power reduced by a factor q, and it will exhibit a specific phase sequence as discussed in chapter 2.3.

Now, if we instead considered this fractional image as an input waveform, and made it propagate through a further amount of dispersion as to reach the next integer Talbot image, we would recover an amplified waveform with lower periodicity. This is the essence of temporal Talbot amplification, as depicted in Fig. 3.1; given an input signal with an initially flat phase, we can impose on it the phase relation of a fractional Talbot image using an electro-optic Phase Modulator (PM). By then making this waveform propagate through a specific amount of Group Velocity Dispersion (GVD), it will reach a integer Talbot image with a period and power increased by a factor q, resulting in the passive amplification of the individual waveform by coherent addition, at the cost of a lower periodicity.

This process can be described in further details by analyzing the process through the dynamics of the spectral modes of the signal. In Fig. 3.2 (a), we start with a periodic train of pulses with a flat phase, as indicated by the equal phase value of each spectral components. We then modulate the temporal phase of each pulse according to a Talbot condition, shown in Fig. 3.2 (b) for $q = 2$. This causes the spectral modes to split due to the lower frequency period of the imposed phase pattern. This step effectively corresponds to the spectral Talbot effect. These modes display a phase variation which also follows a Talbot condition. Finally, the spectral modes are realigned by dispersive propagation, resulting in the coherent addition of q pulses, see Fig. 3.2 (c). This realignment is precisely due to the fact that the resulting phase variation following the first phase modulation (i.e, 3.2 (b)) can be calculated exactly using the mathematics from section 2.3. Thus, the second phase modulation (3.2 (c)) is chosen to align the spectral modes by compensating the induced phase.

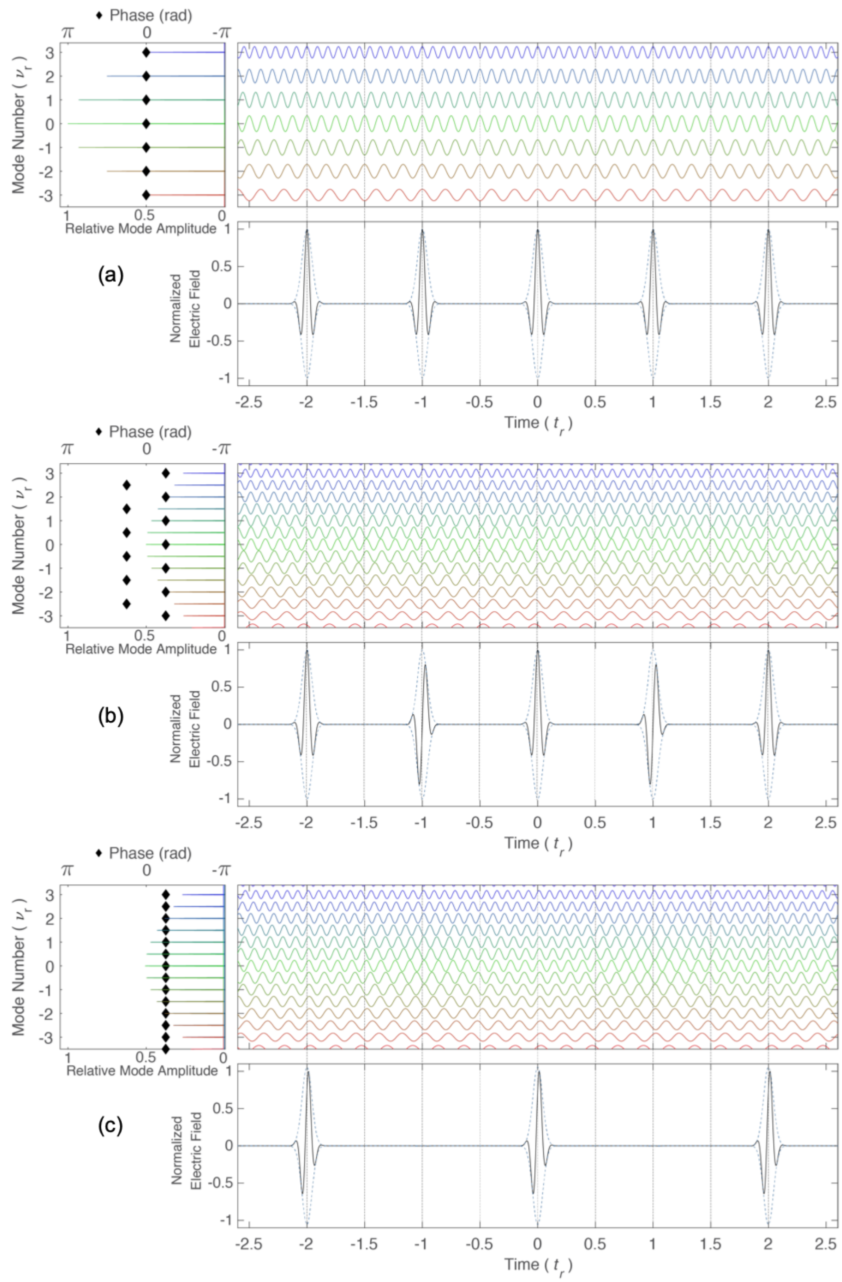

Fig. 3.2 – Mode dynamics in periodic Talbot amplification. (a) The input signal consists of a periodic train of pulses with constant phase. (b) Phase modulation according to a Talbot condition for a given q will cause each spectral modes to separate into q modes, here shown for $q = 2$. These newly formed modes also exhibit a phase satisfying a (possibly different) Talbot condition. (c) Dispersive propagation by the proper amount will cause the spectral modes to realign, causing coherent summation of q pulses.

Alternatively, it is possible to generalize the concept of Talbot amplification using a reasoning purely based on concepts derived from the Talbot effect. In the interest of clarity, I will describe the principle of Talbot amplification for temporal waveforms, however, one must keep in mind that a

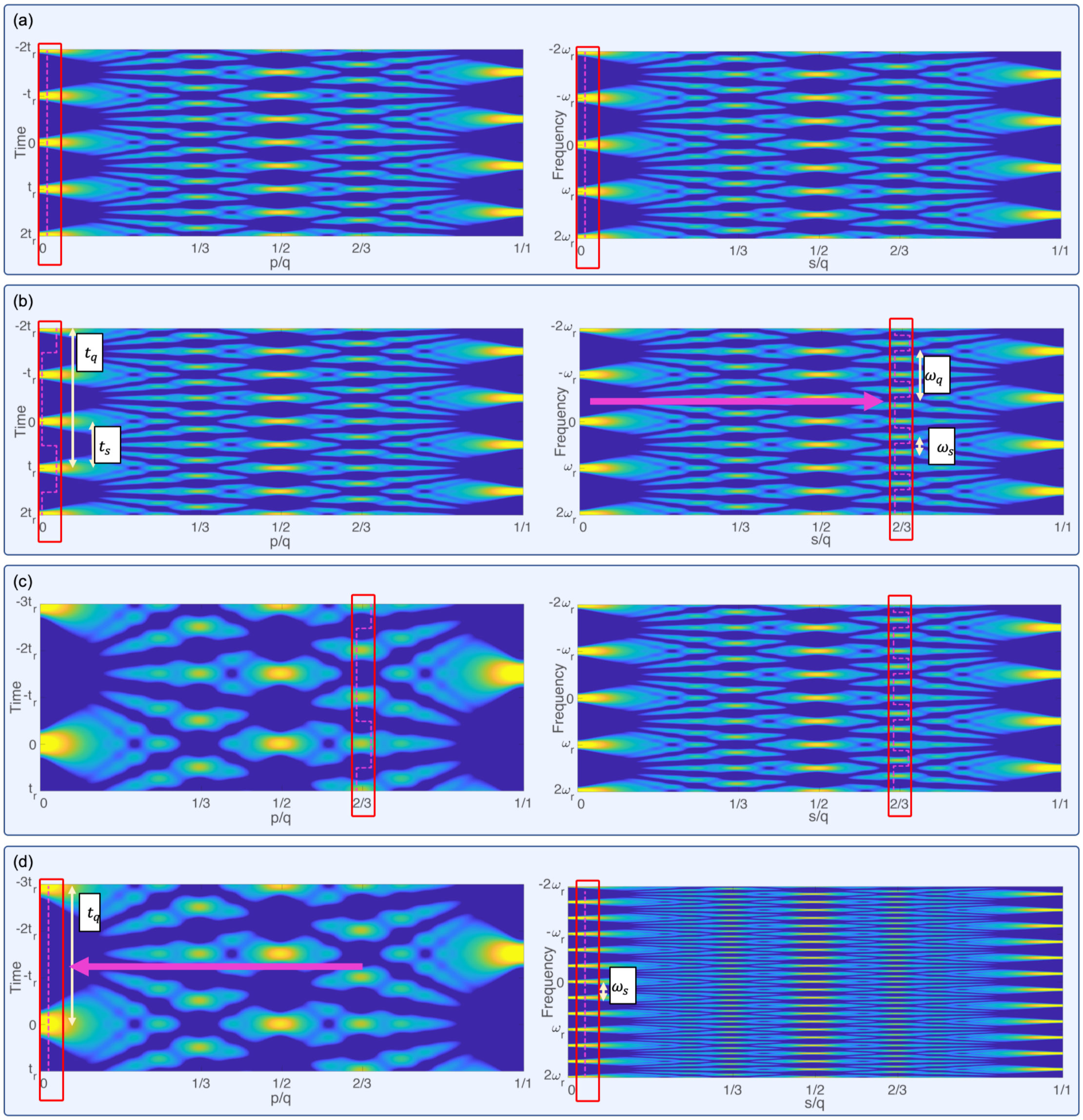

Fig. 3.3 – Steps for Talbot amplification viewed in both domains simultaneously. (a) We start with a periodic signal with a flat phase in both domains, such that both images correspond to an integer Talbot image. (b) We modulate the phase of the temporal signal according to a Talbot condition with a sequence of length q. This shifts the spectral waveform to a fractional Talbot image which has a spectral period reduced by a factor q (i.e., Spectral Talbot effect). (c) Since the temporal signal now has a phase variation, it is no longer an Integer Talbot image. We may say it is transposed to a different Talbot carpet where the Integer image has a period q times bigger, such that the signal is assigned to its proper fractional Talbot image, in terms of period length and phase sequence. (d) Finally, by compensating the spectral phase acquired by the spectral Talbot image, it becomes the integer Talbot image of a Talbot carpet, and the temporal Talbot image is shifted to an integer Talbot image, such that q pulses are coherently summed.

similar reasoning can be carried out to any other domain, as described in section 2.2.3. The general reasoning relies on three basic postulates:

1. Only the fundamental Talbot images have a flat phase. In this case, the periodicity of the signal in the observation domain is related to the periodicity of its Fourier-dual image are related exactly by their inverse (i.e., $\omega_r = 2\pi/t_r$).

2. All higher-order Talbot images exhibit a phase in the form of a Talbot condition in both Fourier domains, and these phase sequences are DFT pairs of each other [139]. Thus, given a q-periodic phase sequence of length $t_q = qt_s$, where t_s is the temporal duration of a single phase level, it will be associated with a unique phase sequence of length $\omega_q = q\omega_s$, where ω_s is the spectral extend of a single phase level. These phase sequences are related by eq. 2.31, and their durations are Fourier inverses of each other, $\omega_s = 2\pi/t_q$ and $\omega_q = 2\pi/t_s$.

3. All higher-order (or fractional) Talbot images with a phase sequence of length q belong to a Talbot carpet whose fundamental image has a period q times bigger. Thus, all fractional Talbot images satisfy $t_r = qt_s = t_q$ ($\omega_r = q\omega_s = \omega_q$).

Keeping these postulates in mind, the Talbot amplification can be described step by step in both Fourier domains simultaneously as follows, graphically presented in Fig. 3.3:

a) We start with a transform limited waveform (flat phase), with temporal period t_r spectral period ω_r.

b) The temporal phase is modulated following a Talbot condition. As an example, this is done in Fig. 3.3 (b) with $p = 2$ and $q = 3$, resulting in a phase modulation signal of length $t_q = 3t_s$, where $t_s = t_r$. This shifts the Fourier-dual image along the carpet, as indicated by the pink arrow, reducing the spectral period and intensity profile by an amount $q = 3$. A phase sequence of length $q = 3$ with $s = 2$ is induced in this waveform, as detailed in section 2.3, and we have $\omega_q = 3\omega_s = \omega_r$ (per postulate 2).

c) Although the resulting Fourier-domain function still belongs to the same initial Talbot carpet, since it satisfies $\omega_q = \omega_r$, the temporal waveform now belongs to a Talbot carpet where the fundamental Talbot image has a period $q = 3$ times bigger (per postulate 3).

d) The phase in the Fourier-dual domain is compensated by spectral phase filtering according to the conjugate of the induced phase. This makes both domains reach a fundamental Talbot image. In particular, the image in the temporal domain is shifted to a new location on the Talbot carpet, as shown by the pink arrow, such that its period is increased by q.

Experimentally, step (b) of Fig. 3.3 can be done by imposing a Talbot phase relation on the pulse train using an electro-optic Phase Modulator (PM). Step (d) then corresponds to the subsequent dispersive propagation of said signal through an amount of dispersion corresponding the conjugate of the induced phase, causing the coherent summation of q temporal waveforms. In practice, spectral phase filtering is conveniently achieved by dispersive propagation through a Linearly-Chirped Fiber Bragg Grating (LCFBG). An important practical consideration for spectral phase filtering is that higher dispersion values typically result in higher losses and/or higher experimental complexity. Thus, in order to minimize the required amount of dispersion, the design equations are usually kept such that $p = 1$ (considering that the condition with the integer p is applied via GVD). This then sets the integer $s = 1 + qe_q$, such that we have the design equations

$$\ddot{\phi} = \sigma_\phi \frac{2\pi}{\omega_r^2}\frac{1}{q}; \qquad \varphi_n = \sigma_\phi \pi \frac{1 + qe_q}{q} n^2, \tag{3.1}$$

where $\sigma_\phi = \pm 1$ and $n = 0, ..., q-1$ is a periodic index for the temporal pulses. Note that here, both phase modulations have the same sign, since the applied GVD is conjugate to the induced phase (eq. 2.31).

For a desired amplification factor, the design equations are not unique, as one could reach either an exact or an inverted integer Talbot image. This degree of flexibility allows for other expressions of the phase modulation signals by choosing different combinations of the phase factors p and s, corresponding to different amounts of GVD and different temporal phase modulation signals. Furthermore, it is generally not necessary to return to a fundamental Talbot image. Indeed, in step (d), one could choose a different phase modulation pattern which would instead reach another fractional Talbot image. This concept has been exploited for fractional averaging of repetitive waveforms [155] and arbitrary repetition-rate control of periodic pulse trains [156].

3.2 The Talbot array illuminator

As mentioned above, Talbot amplification of periodic waveforms showed convincing noise mitigation abilities [145, 146, 147, 148]. Although periodic waveforms find application in a wide variety of fields, this strict requirement for the waveform to be periodic imposes a significant limitation for its

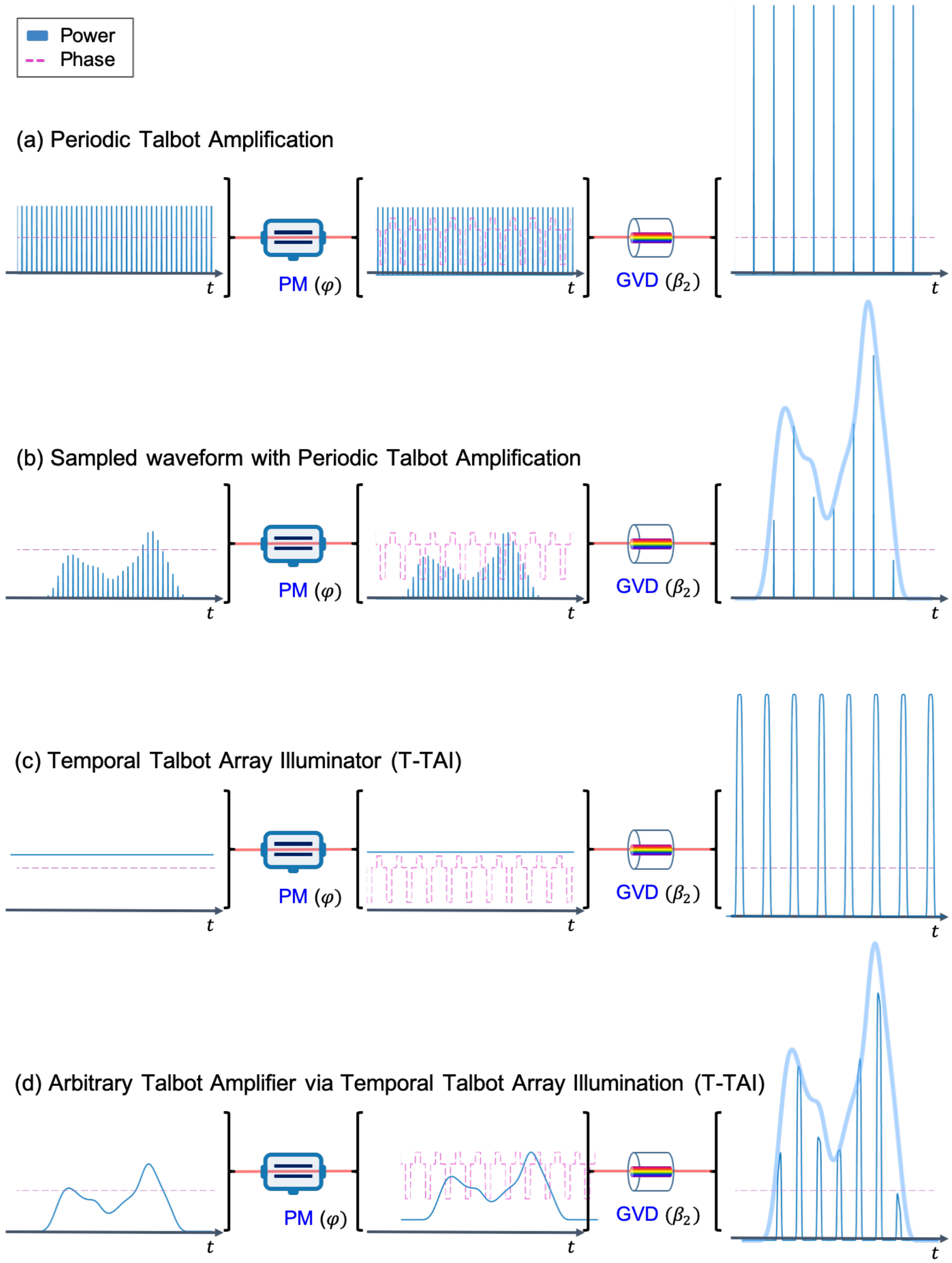

Fig. 3.4 – Principle for noiseless amplification of arbitrary waveforms. (a) Periodic Talbot amplification enables noiseless amplification of the individual pulses of a periodic waveform. (b) This could be adapted for arbitrary signals by sampling them with a pulse train. However, this method is inefficient since an important part of the signal is discarded. (c) a Temporal Talbot Array Illuminator (T-TAI) allows to convert a CW signal into a pulse train. (d) The T-TAI can be employed for efficient noiseless amplification of arbitrary waveforms. Note that the phase manipulations are the same in all cases.

application on arbitrary waveforms. To circumvent this requirement of periodicity, one approach could be to simply apply the Talbot amplification scheme on a sampled version of the arbitrary signal, as illustrated in Fig. 3.4 (b). Indeed, this approach seems suitable for processing aperiodic

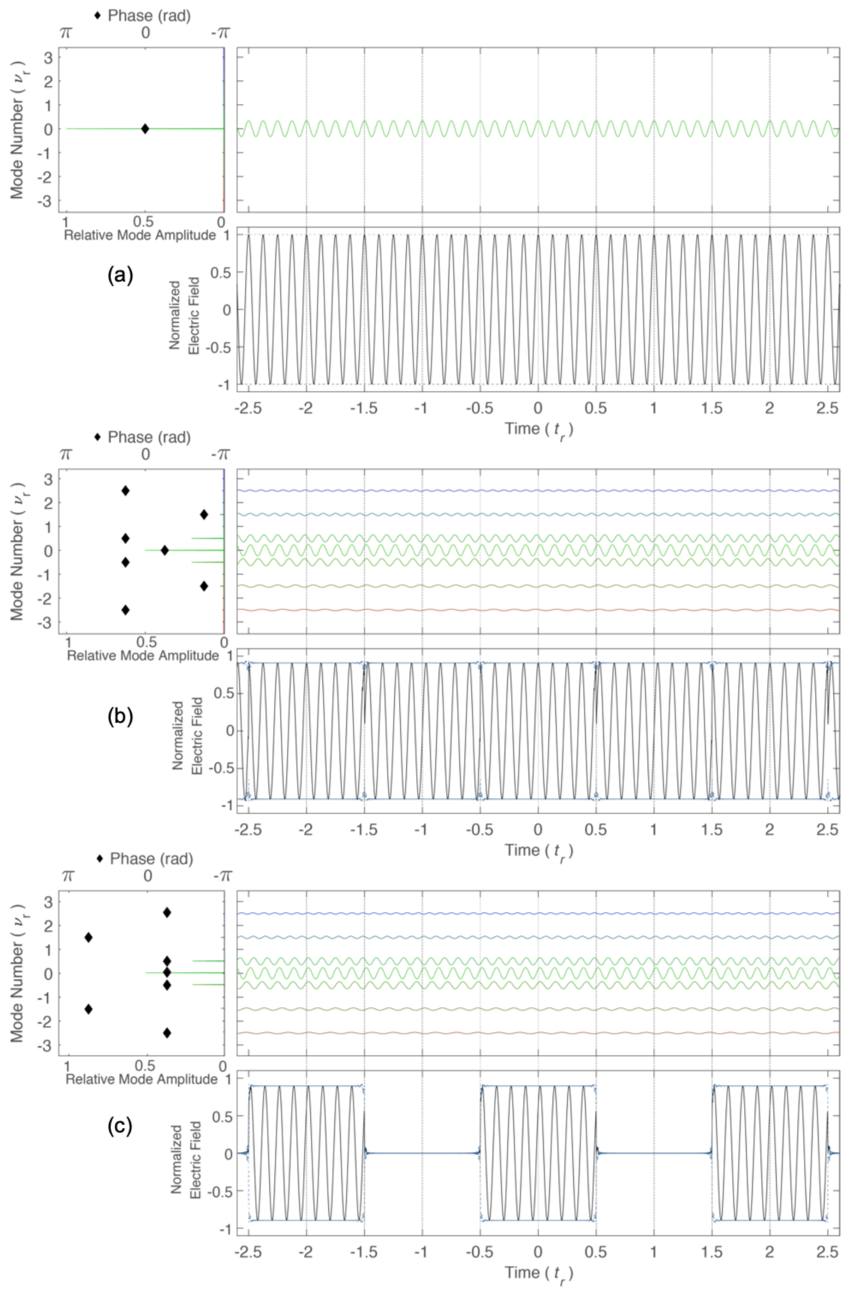

Fig. 3.5 – Mode dynamics of a TAI. (a) We start with a CW signal as an input signal. (b) The signal is phase modulated according to a Talbot condition, with $p, q = 1, 2$. This causes the CW to split in different modes, exhibiting a spectral phase comprised of both the induced Talbot phases and the sinc phase. (c) The spectral Talbot phases are compensated, causing the modes to align, effectively redistributing the energy into separate pulses. Note that the leftover phase is due to the sinc envelope, and that each temporal representation is normalized to show the phase of the carrier signal. Thus, the intensity increase by a factor $q = 2$ of the waveform in (c) is not shown here.

signals. However, the sampling stage itself is very inefficient, since a large part of the signal's energy is discarded.

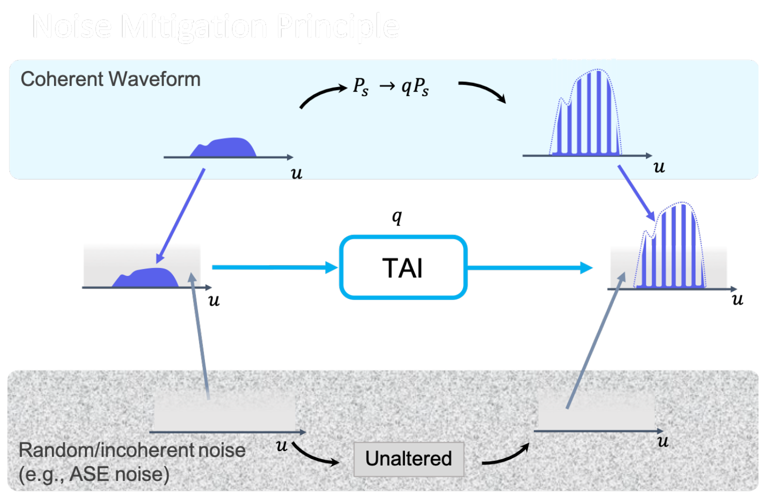

Fig. 3.6 – Noise mitigation principle of the TAI. A signal completely buried under noise can be recovered using a TAI since it acts only on the coherent part of the signal. Thus the SUT is redistributed into a series of peaks which have an envelope following the initial signal. The same process can be applied either in the temporal (T-TAI) or spectral domain (S-TAI).

On the other hand, a Temporal Talbot Array Illuminator (T-TAI) allows to efficiently convert a continuous wave (CW) signal into a periodic pulse train (see Fig. 3.4). The concept behind a TAI consists of imposing a periodicity on an aperiodic waveform via the phase modulation. Subsequent dispersive propagation then leads to a redistribution of the energy into discrete peaks. The process can be view by modal decomposition, depicted in Fig. 3.5. Effectively, the phase modulation causes the CW to split into various modes, with an envelope given by a sinc function[1], and the following dispersive propagation causes these modes to align, creating an array of square pulses.

The key finding of this thesis was the realization that the TAI preserve the shape of an input waveform through the envelope of the peaks, as depicted in Fig. 3.4 (d). Thus, all the energy of the waveform is maintained, ideally performing a lossless sampling process on the analog waveform. The idea is similar in spirit to a regular TAI, except that here we exploit for the first time its noise mitigation capabilities by using the TAI on information-bearing waveforms, enabling unprecedented noisy signal recovery. As illustrated in Fig. 3.6, the process relies on phase coherence of the signal to be processed. Thus, since incoherent noise, such as the ASE noise produced by EDFAs, consists of rapid fluctuations in both amplitude and phase, it is left virtually unaltered by the passive amplification process. On the other hand, the SUT is amplified into a series of peaks, and sufficient amplification allows for the signal to be recovered from the peaks. In practice, the effect of the TAI when applied to the temporal or spectral domain has very different properties. As shown in chapter 4, when applied to the temporal domain (referred to as temporal Talbot array illuminator, T-TAI),

[1] $\mathrm{sinc} = \frac{\sin(x)}{(x)}$ is the Fourier pair of the rect(x) function, where rect(x) $= 1$ for $x < 1/2$ and zero otherwise [92]. Since the phase sequence is applied in a discrete fashion, the Fourier transform of a CW modulated by Talbot phases is a sinc function. The lobes of this function have an alternating $\pi/2$ phase variation.

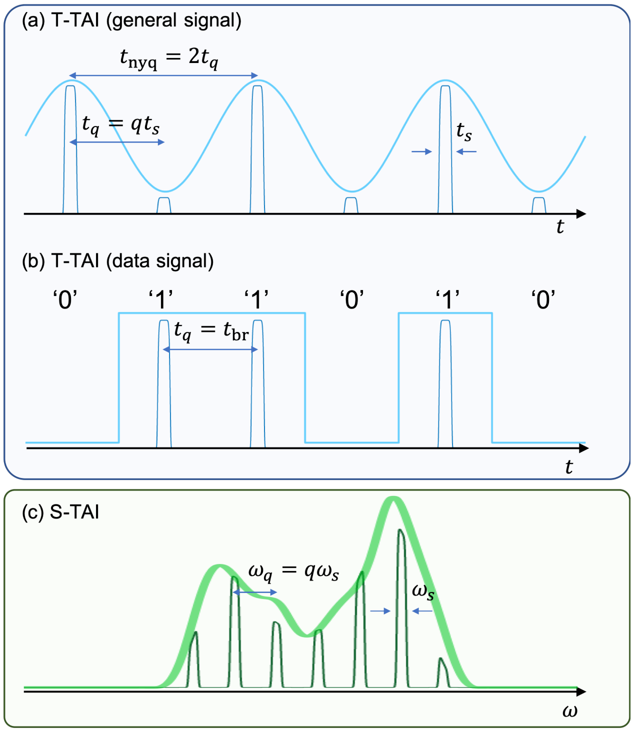

Fig. 3.7 – Nyquist sampling criterion, for (a) an arbitrary temporal signal, (b) a data signal in the temporal domain, and (c) an arbitrary spectrum.

this method offers unique noise mitigation for narrowband signals [AC1, AC2, AC3], a difficult feat to achieve in photonic systems. On the other hand, when applied to the spectral domain (referred to as spectral Talbot array illuminator, S-TAI), it is possible to mitigate noise contained within the bandwidth of the signal itself [AC4, AC5, AC6]. This so-called in-band noise has been the subject of research for many years, and the novel solution using the TAI to mitigate in-band noise in broadband signals is described in chapter 5.

The information contained within the input waveform is preserved as long as the output peaks satisfy the Nyquist sampling criterion with respect to the input waveform [92], as with any sampling process[2]. Therefore, given a SUT which has its sharpest temporal variations with temporal resolutions t_{nyq}, corresponding to frequencies $\nu_{\text{nyq}} = 1/t_{\text{nyq}}$, then the TAI needs to be designed such that the output peak separation t_q is at least twice as short as the fastest variations, $t_q < 2t_{\text{nyq}}$, as shown in Fig. 3.7 (a). In the context of data signals, the duration of a phase sequence t_q must be equal or shorter than a single bit period. If t_q is shorter than a single bit period, then the ratio of the bit duration to t_q must be integral, yielding an integer amount of output peaks per bit (see Fig. 3.7 (b)). In the case of the S-TAI, the same Nyquist sampling criterion applies, except for the spectral waveform rather than the temporal waveform (see Fig. 3.7 (c)). Thus the output

[2]The Nyquist sampling criterion describes the minimum sampling rate necessary to recover the information contained in a given waveform.

spectral peaks spacing ω_q must be small enough to sample the spectrum of the waveform properly. Effectively, this means that the S-TAI has an inherent limitation to process signals extending over a long temporal duration, which require a very fine spectral resolution. On the other hand, since the S-TAI can operate over very broad spectral regions, the S-TAI is intrinsically suited to process broad waveforms. Note that in both cases, the Nyquist criterion must be satisfied for the phase variation of the input signal signal as well as for the amplitude variations. The specific limitations for each case are treated in more detail in the following section.

3.3 Arbitrary signal amplification and noise mitigation

This section describes the specific implementation of both the T-TAI and S-TAI along with their associated limitations. Here we assume that a continuous quadratic phase filtering scheme is applied in the spectral domain. As noted in chapter 2.3 for periodic Talbot amplification, the use of a continuous phase modulation in one of the two domains is nearly identical to the use of discrete phase modulation schemes in both domains. On the other hand, when the technique is extended to aperiodic waveforms as in the TAI, the difference is small, but noticeable in simulations. While there is no published work on this at the moment, the implications of a continuous phase modulation scheme versus a purely discrete scheme is a timely subject that will surely be documented in the close foreseeable future.

Furthermore, the following discussion assumes that an AWG is used to provide the phase modulation pattern to an electro-optic PM. As discussed below, the maximum sampling rate of the AWG turns out to be an important limitation of the system. It should however be noted that if higher sampling rates are required, alternative methods may be chosen for the temporal phase modulation, allowing a smaller t_s. For example, one may resort to the use of an RF synthesizer. This allows for higher effective sampling rate, since certain Talbot phases can be approximated by a sinusoid. This approach however limits the amplification factors to about 4-5 [157][AC4]. Alternatively, one may also use XPM-based approaches to apply the phase modulation [158, 159], and it is theoretically possible to reach high amplification factors by shaping the optical waveform to the desired Talbot phase. This specific implementation is currently an active area of research, and could potentially alleviate the limitation caused by the sampling rate of AWGs, at the cost of the higher complexity associated with nonlinear optics approaches.

3.3.1 Temporal implementation

The implementation of a T-TAI is similar to that of a periodic temporal Talbot amplifier, except that now the phase modulation equations are designed for a *virtual* period. This virtual period coincides with the width of the output peaks, dictated by the duration t_s of a single phase modulation level. These peaks are in turn separated by $t_q = qt_s$. As discussed with eq. 3.1, the dispersion is usually kept at a minimum, such that the design equations for a T-TAI are

$$\varphi(t) = \sum_{l=0}^{q-1} \mathrm{rect}(t - lt_s)\sigma_\phi \frac{1 + qe_q}{q} \pi l^2 \qquad\qquad \ddot{\phi} = \sigma_\phi \frac{t_s^2}{2\pi} \frac{q}{1}, \tag{3.2}$$

where the temporal phase modulation is applied periodically, and the function $\mathrm{rect}(t) = 1$ for $|t| < 1/2$, and zero otherwise. Note that the temporal phase modulation is applied first, followed by dispersive propagation. Typically, high amplification factors are desired, such that the T-TAI is designed to have the integer q as high as possible. A high amplification factor poses a requirement on the amplitude resolution of the phase modulation signal, which is given by the bit resolution of the AWG. Considering the 8-bit resolution of the employed AWGs, this was not considered to be a significant issue. However, all experiments have shown an unexpected upper limit on the amplification factor near $q = 30$. It would thus be informative to further investigate the impact of the AWG resolution on the amplification factor, since the reason for this limitation near $q = 30$ is currently not well understood.

As mentioned above, the T-TAI's ability to process rapidly varying signals, such as high bandwidth data signals, is ultimately limited by the maximum sampling rate and bandwidth of the employed AWG. As illustrated in figure 3.7 (a), the phase modulation sequence length must satisfy the Nyquist rate with respect to the SUT to avoid the loss of information in the sampling process. Considering that state-of-the-art AWGs have sampling rates in the range of $\nu_{AWG} \approx 50$ to 100 GS/s, and that amplification factors of at least $q \approx 10$ are needed for interesting noise mitigation effects, this set the maximum bit rate of processable data signals to $\nu_{AWG}/q \approx 5$ to 10 GS/s, or general analog signals with bandwidths up to $\nu_{\mathrm{Nyq}} = \nu_{AWG}/(2q) \approx 2.5$ to 5 GHz.

On the other hand, the T-TAI's ability to yield sampled signals with large output peaks t_s with broad temporal separations t_q is limited by the maximum amount of available dispersion. Wider output peaks could be required in applications where lower bandwidth electronics which cannot manipulate fast signals in the tens of GHz range are employed. As previously mentioned, fiber optic cables can be used to achieve large amounts of dispersion, but this requires propagation through several hundreds of km of fiber, resulting in very high losses. For example, ref. [145] showed amplification by a factor $q = 27$ using a high dispersion value of $|\ddot{\phi}| \approx 10,200$ ps^2 equivalent to about 470 km of fiber, which caused 70 dB of insertion loss, such that no net gain (input-to-output gain) was observed. Therefore, LCFBGs are favoured for high dispersion values, and commercially available LCFBGs offer values of $|\ddot{\phi}| \approx 12,750$ ps^2 with as little as 2 dB of loss. Assuming a T-TAI implemented with such a dispersion value and an amplification factor $q = 10$, peaks with a width of $t_s = \sqrt{2\pi\ddot{\phi}/q} \approx 90$ ps at a rate of $\sim$1.1 GHz ($t_q \approx 0.9$ ns) can be generated.

Finally, the unique ability of the T-TAI to function regardless of the carrier signal of the signal can be noticed from the absence of a wavelength dependence in equations 3.2. The limitation of the T-TAI in this regards depends solely on the flatness of the employed components over the operation bandwidth. Electro-optic PMs can be made with a flat response over the entire C+L bands (1530 nm to 1625 nm), and LCFBGs can also be made to function over such wide bands.

3.3.2 Spectral implementation

The S-TAI is implemented with similar design equations, except that the module operates in a reversed order, i.e., spectral phase filtering followed by temporal phase modulation. This process yields a spectrum which is a sampled and amplified version of the input, composed of spectral peaks of width ω_s, separated by ω_q. The design equations in this case are given by

$$\ddot{\phi} = \sigma_\phi \frac{2\pi}{\omega_s^2}\frac{1}{q} \qquad \varphi(t) = \sum_{l=0}^{q-1} \mathrm{rect}(t - lt_s)\sigma_\phi \frac{1 + qe_q}{q}\pi l^2. \tag{3.3}$$

In this case, the limitations are somewhat "inverted"; to process a spectral with finer spectral resolution, corresponding to signals with longer temporal durations, the limitations are ultimately caused by the need for large dispersion values. In this case, the S-TAI needs to be designed such that the spectral peak separation ω_q is small enough to satisfy the nyquist rate with respect to those finer spectral variations (see Fig. 3.7 (c)), thereby increasing the value of $\ddot{\phi}$ in eq. 3.3. Thus, assuming a dispersion value of $|\ddot{\phi}| \approx 12,750$ ps^2 and an amplification factor $q = 10$, the S-TAI would give output peaks with a width $\omega_s/2\pi = \sqrt{1/(2\pi\ddot{\phi}q)} \approx 1.1$ GHz, separated by a spectral period $\omega_q/2\pi \approx 11$ GHz. Since finer spectral features corresponds to longer temporal signals, this minimum spectral sampling period allows to process signals with maximum temporal durations of about 910 ps to avoid any loss about the SUT.

On the other hand, cases where a wide spectral peak separation ω_q is needed will be limited by the maximum sampling rate of the AWG, since larger ω_q demand for shorter sampling periods t_s in eq. 3.3. Therefore, considering AWG sampling rates near $50 - 100$ GS/s, this results in maximum spectral peak separations of about $\omega_q/(2\pi) = 1/t_s = \nu_{AWG} = 50 - 100$ GHz.

Finally, as with the T-TAI, the S-TAI has no fundamental limitation on the wavelength range it can operate, once again only limited by the operation bandwidth of the employed components.

Chapter 4

Noise Mitigation of Narrowband Signals

We may interpret the T-TAI as performing an operation akin to a sliding average directly in the analog temporal domain, resulting from the coherent summation of the signal into discrete bins of width t_s, separated by t_q. As shown below, this implementation offers a very simple and practical way to implement a narrowband filter without the issues associated with the typical narrowband filtering schemes mentioned above. Here, we show results of the T-TAI with high amplification factors up to 28.5, allowing a net gain of 5.42. This high amplification factor enables the retrieval of a signal completely buried under noise, independently of the central frequency of the signal. This is followed by a detailed comparative analysis of the proposed scheme versus a 5 GHz narrowband filter on low frequency sinusoids. Such a filter corresponds to the best performance of commercially available filters, and our results show concrete evidence of the superior performance of the T-TAI versus such a filter. This section finishes with a practical demonstration of the noise mitigation capabilities of the T-TAI on data signals with bit rates varying from the Mb/s to Gb/s range, with metrics commonly used in the telecommunications industry to accurately establish the various advantages of the T-TAI approach. The results presented in this Chapter were reported in [AC1, AC2, AC3].

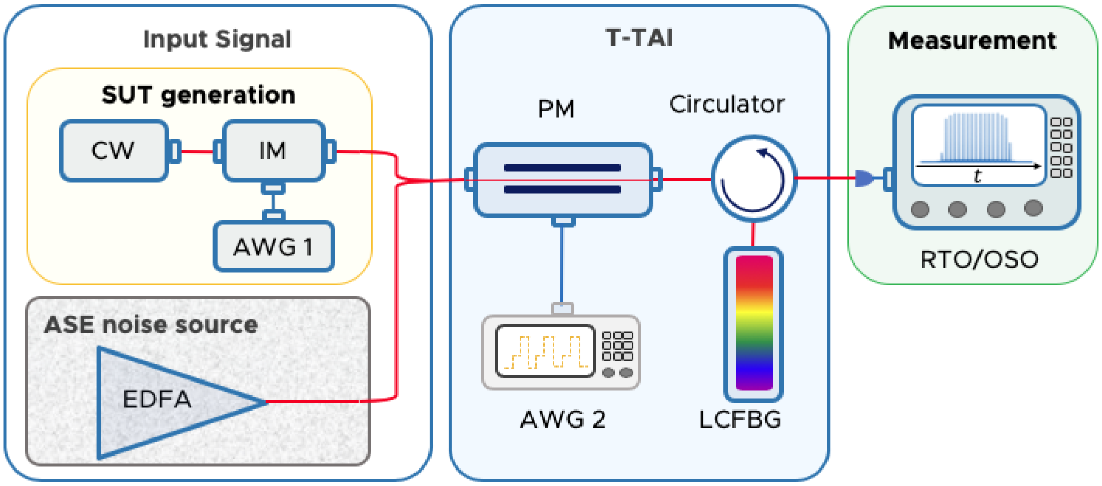

Fig. 4.1 – Experimental setup for the T-TAI. CW: Continuous Wave, IM: Intensity Modulator, AWG: Arbitrary Waveform Generator, EDFA: Erbium-Doped Fiber Amplifier, PM: Phase Modulator, LCFBG: Linearly Chirped Fiber Bragg Grating, RTO: Real-Time Oscilloscope, OSO: Optical Sampling Oscilloscope

4.1 Experimental setup

The experimental setup used for the experiments described in this chapter is shown in Fig. 4.1. The optical signal was first generated by a CW laser operating at 1551 nm, unless otherwise stated. This signal was then carved by an electro-optic Mach-Zender Intensity Modulator (IM) driven by a radio-frequency (RF) arbitrary waveform generator (AWG) in order to generate the Signal Under Test (SUT). For noise mitigation experiments, this signal was combined with amplified spontaneous emission (ASE) noise generated by a high power Erbium-Doped Fiber Amplifier (EDFA), in order to lower the Signal-to-Noise Ratio (SNR) of the SUT, thus defining the input signal. This prepared signal is then processed by the T-TAI module, which consisted of a 40 GHz bandwidth electro-optic Phase Modulator (PM) driven by a high-speed RF-AWG where the Talbot phases were programmed, followed by a Linearly-Chirped Fiber Bragg Grating (LCFBG) for the dispersive propagation, with either $D = -2076$ ps/nm or $D = -10,000$ ps/nm, depending on the experiments. Note that dispersive LCFBG work in a reflective configuration, so a circulator is required to re-route the optical signal. The resulting signal was then recorded, using either a 50 GHz photodetector (Finisar) connected to a 28 GHz bandwidth oscilloscope (Agilent Infinuum DSO-X 92804), or a 400 GHz bandwidth optical sampling oscilloscope (OSO) to measure eye the diagrams of data signals. For the comparative studies, the T-TAI module was replaced by the corresponding BandPass Filter (BPF). For results consisting of both a BPF and the T-TAI, the BPF was placed first, followed by the T-TAI.

4.2 Employed metrics

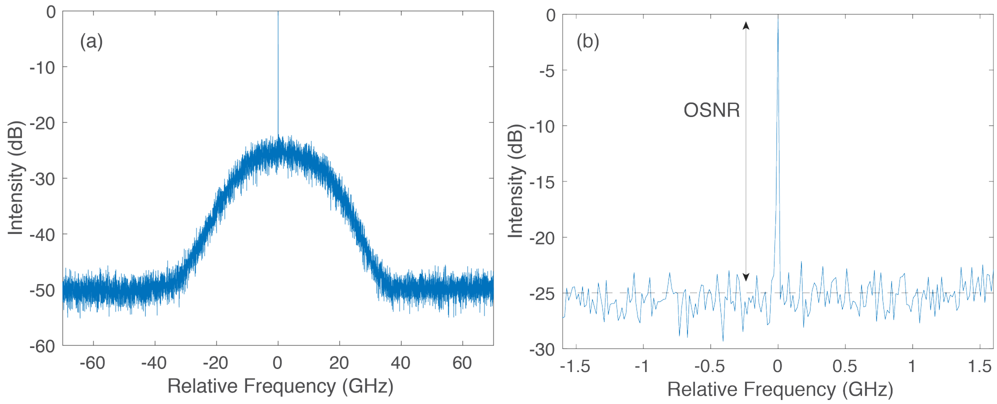

Fig. 4.2 – OSNR calculation. a) The spectrum of the ASE noise generated by two cascaded EDFA had a 3-dB FWHM of 28 GHz. b) The OSNR is measured by comparing the power of the carrier signal to that of the noise in the vicinity of the carrier wavelength.

To quantify the amount of noise present in a given signal, two different noise metrics are employed. In some cases, the SNR is used, which is simply defined as the overall power of the signal divided by the power of the noise, measured at the input of processing module using a power meter. Thus, this metrics considers the total amount of optical power, regardless of wavelength. The second noise metrics is the Optical Signal-to-Noise Ratio (OSNR), often employed in optical telecommunication. This metrics is defined as the ratio of the power of the signal to that of the ASE noise level

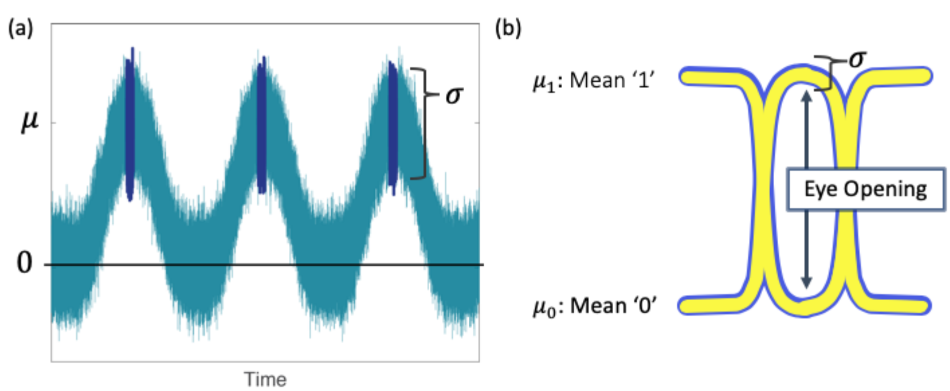

Fig. 4.3 – (a) Definition of the Variation Reduction Factor (VRF). The VRF is defined as the ratio of the coefficient of variation (CV) of the output of a given noise mitigation process to that of the input. In turn, the coefficient of variation is defined as the standard of deviation σ divided by the mean value μ, taken near the peak of each crest, $\mathrm{CV} = \sigma/\mu$, such that a very weak and noisy signal would have a high CV. Thus, an effective noise mitigation scheme would have a low $\mathrm{VRF} = \mathrm{CV}_{\mathrm{out}}/\mathrm{CV}_{\mathrm{in}} = \frac{\sigma_{\mathrm{out}}}{\sigma_{\mathrm{in}}} \frac{\mu_{\mathrm{in}}}{\mu_{\mathrm{out}}}$. (b) Illustration of the eye opening as a metrics for signal quality, defined as $E_o = (\mu_1 - 3\sigma_1) - (\mu_0 + 3\sigma_0)$.

adjacent to the signal, interpolated into the SUT's bandwidth [160, 161]. Thus, it is an estimate of the noise contained within the bandwidth of the signal, as illustrated in Fig. 4.2.

To quantify the signal quality for a waveform of arbitrary shape, two metrics are employed: the Variation Reduction Factor (VRF) and the Squared Pearson Correlation Coefficient (SPCC). The VRF is defined as the ratio of the Coefficient of Variation (CV) of the output waveform to the input waveform. The CV is in turn defined as the standard deviation σ divided by the mean value μ, taken near the peaks of a signal [145] (see Fig. 4.3 (a) for further details on this definition). Thus, an effective noise mitigation scheme would lead to a low VRF, indicating a decrease in the CV by the processing module.

The SPCC is also employed to investigate the behaviour of the noise mitigation schemes. It is widely recognize as a relevant criterion to indicate the SNR improvement of a filtering process [162], and is given by the square of the well-known Pearson correlation coefficient ρ, which is defined as the normalized cross-correlation between two signals x and y,

$$\text{SPCC} = \rho^2(x, y) = \frac{E^2[xy]}{\sigma_x^2 \sigma_y^2}, \tag{4.1}$$

where $E[xy]$ is the cross-correlation between signals x and y with variance $\sigma_x^2 = E[x^2]$, $\sigma_y^2 = E[y^2]$. The SPCC can be used as a cost function for the optimization of a filtering process, and gives an indication of the strength of the linear relationship between two random variables. If $\rho^2(x, y) = 0$, then x and y are said to be uncorrelated, whereas the closest the value of $\rho^2(x, y)$ is to 1, the stronger is the correlation between these variables.

Finally, to quantify the signal quality of data waveforms, the high level amplitude, extinction ratio, and eye height are employed, which are all metrics commonly used for performance monitoring in optical telecommunications. These metrics are typically extracted by the eye diagram, Fig. 4.3 (b), which is generated by stacking the individual bits on top of each other, indicating the clarity and state of the data signal over a certain time duration. The high level amplitude is simply defined as the mean value μ_1 of the high '1' logical bits, where the signal is adjusted such that the mean low '0' value μ_0 is set to 0. The extinction ratio is given by the ratio of the mean '1' value μ_1 to that of the '0' value μ_0 with no adjustments. The eye height E_o is defined as $E_o = (\mu_1 - 3\sigma_1) - (\mu_0 + 2\sigma_0)$,

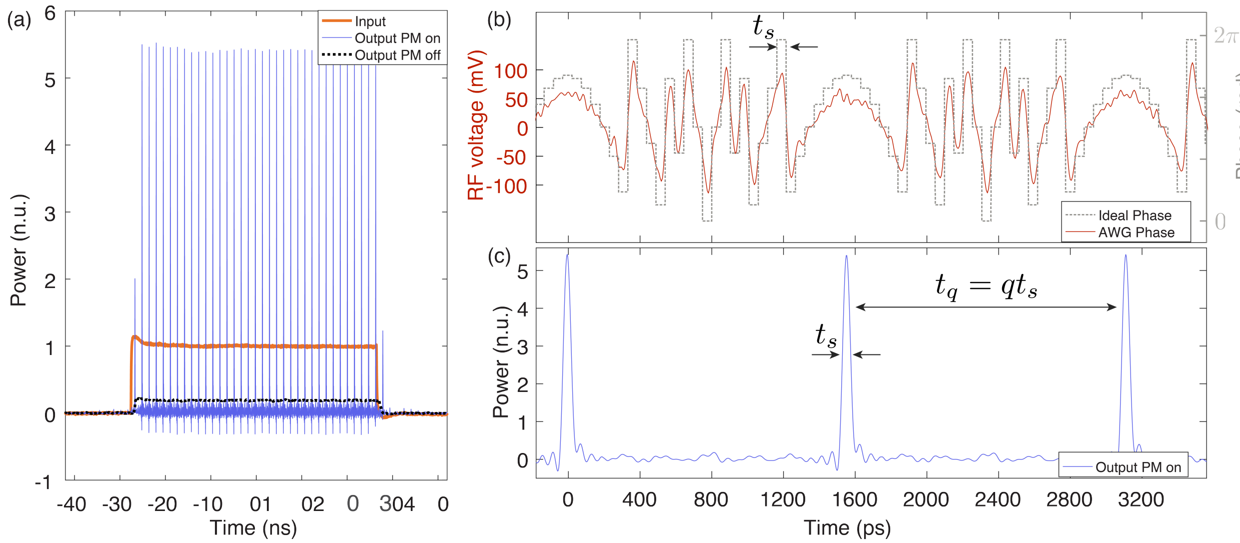

Fig. 4.4 – Experimental demonstration of the T-TAI. (a) The measured amplification factor of 28.5 is measured by comparing the value at the peaks of the TAI (blue trace) vs the signal with the phase modulation turned off (black dotted line). When comparing against the input signal (orange trace), measured at the point right before the Talbot amplifier, the system shows an input to output gain (net gain) of 5.42. All values are given normalized to the value of the input signal. (b) The ideal phase pattern (gray) and measured RF voltage (red), generated at a sampling rate given by the inverse of a single phase level period t_s. (c) The T-TAI produces peaks of width t_s, separated by t_q.

where σ is the standard deviation of the corresponding level, and thus gives an indication of the opening of the eye diagram, as the name clearly indicates.

4.3 Amplification of arbitrary waveforms

To demonstrate the high amplification that can be achieved using the T-TAI, we first apply the scheme on a 54 ns square pulse, depicted in Fig. 4.4. The amplification factor was designed with $q = 30$ and a peak width $t_s = 51.5$ ps, resulting in a peak separation of $t_q = qt_s = 1.56$ ns. The measured amplification was by a factor of 28.5, with a measured peak width $t_s = 47$ ps and peak separation $t_q = 1.53$ ns, in close agreement with the expected values. Note that this measured amplification factor does not account for the insertion loss of the system. Indeed, by turning the phase modulation signal on or off and comparing the signal at the output of the T-TAI module, we are able to directly see the effect of the of the Talbot amplifier. To measure the net gain of our system, we may instead compare the amplified signal to the signal at the input of the amplifier. This therefore takes into consideration the insertion loss from the electro-optic phase modulator and the LCFBG, evaluated at about 7.3 dB, and a net amplification of 5.4 is measured. One should however consider that the insertion loss of such system could realistically be decreased to 3-4 dB

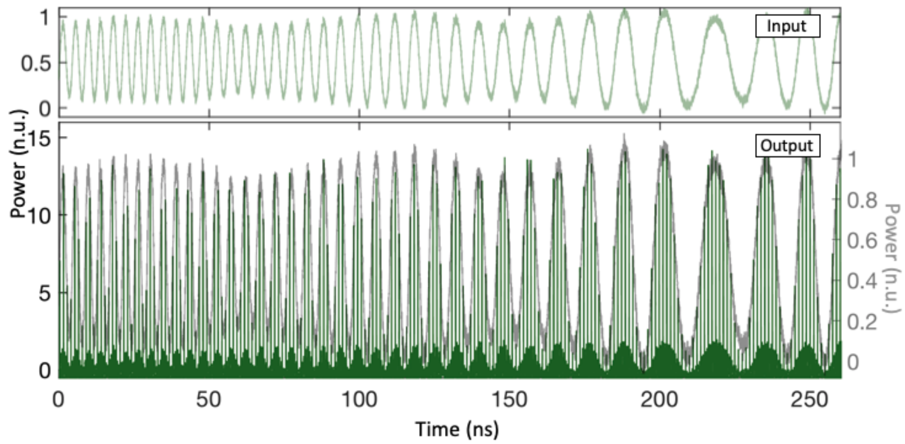

Fig. 4.5 – Experimental demonstration of the amplification of a chirped waveform, from 50 to 250 MHz. The top graph shows the signal with the phase modulation turned off. The bottom graph shows the output, with the input scaled by the measured amplification factor.

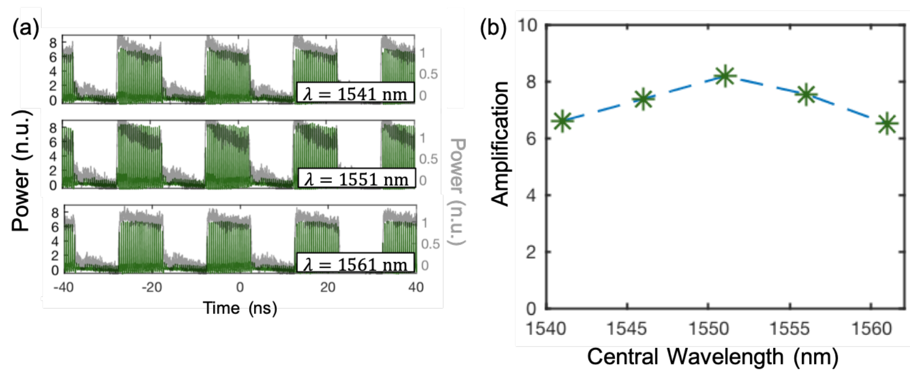

Fig. 4.6 – Wavelength dependence. The T-TAI's wavelength dependence is only due to the operation bandwidth of the employed components. The amplification factor was designed to be 10. The measured amplification factor shows a small dependence over the wavelength shown.

(2 dB for the modulator and 1-2 dB for the LCFBG) by judicious care in assembling the required components.

To show that this concept indeed works well for arbitrary shapes, Fig. 4.5 shows the amplification of a more complicated waveform, namely a chirped sinusoid, with a frequency varying linearly from 50 to 250 MHz. The design parameters in this case were $q = 20$, $t_s = 63.3$ and $t_q = 1.27$ ns, while the measured values were $q = 15.1$, $t_s = 75$ ps and $t_q = 1.25$ ns. The unique ability of the T-TAI to operate regardless of the central wavelength of the signal is demonstrated by Fig. 4.6. Indeed, this particularity of the presented method is of paramount importance due to the issues mentioned above with respect to any drift in central wavelength of a given signal when a bandpass filtering scheme is employed. Furthermore, it allows the T-TAI to process signals of unknown central frequency.

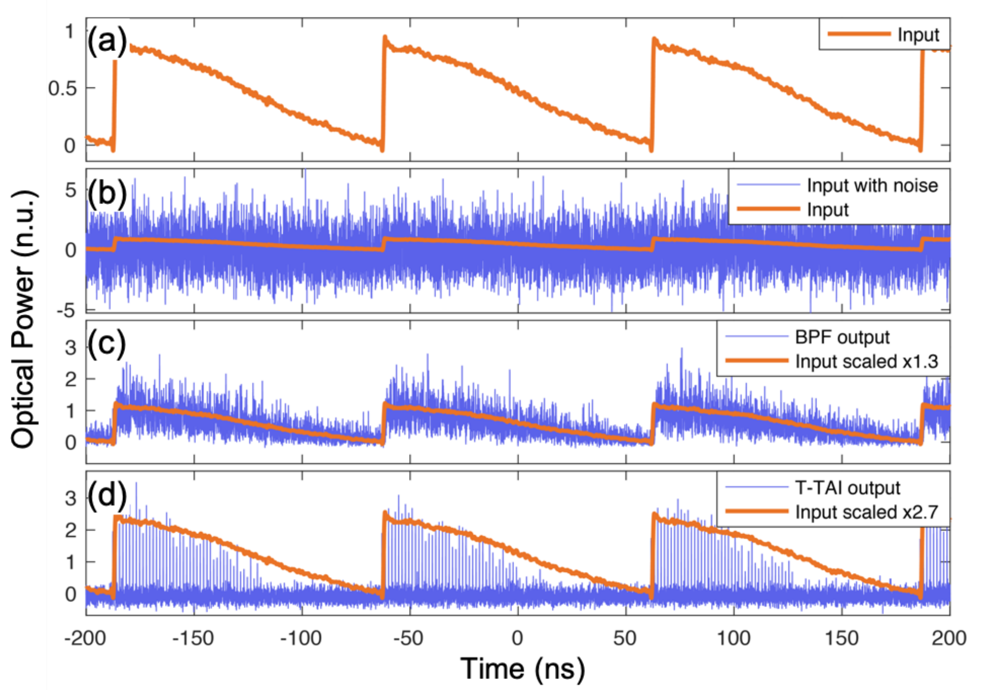

Fig. 4.7 – Recovery of a 8 MHz ramp from noise using a bandpass filter (BPF) and Talbot Array Illuminator (T-TAI). All values are normalized to the value of the signal with the phase modulation turned off. The observed discrepancies in the low amplitude parts of the signal are due to the limited resolution of the oscilloscope which is unable to sample each output peaks appropriately.

4.4 Ultra narrowband noise mitigation

We first demonstrated the narrowband filtering properties of the T-TAI by recovering a 8 MHz ramp waveform and comparing its performance against a 512 pm (62 GHz) bandwidth BPF, using the same T-TAI design parameters as Fig. 4.4. The input signal had an average optical power of -14.14 dB, as measured by a power meter, and it was combined with broadband ASE noise with a power of 4.78 dB, resulting in a SNR $= P_S/P_N = -18.92$ dB, such that the SUT was completely buried under noise. As illustrated in Fig. 4.7, the advantage of the T-TAI to perform simultaneous amplification and noise mitigation is visually apparent; indeed, the inevitable insertion loss associated with any bandpass filter leads to a decrease of the signal power.

To further document the performance of the T-TAI, we prepared a second set of experiments with low frequency sinusoids (see Fig. 4.8). In this case, the BPF had a narrow pass band of 5 GHz, corresponding to narrowest passband typically achieved in commercial narrowband optical filters. In order to maximize the amount of generated ASE noise near the signal bandwidth, the output

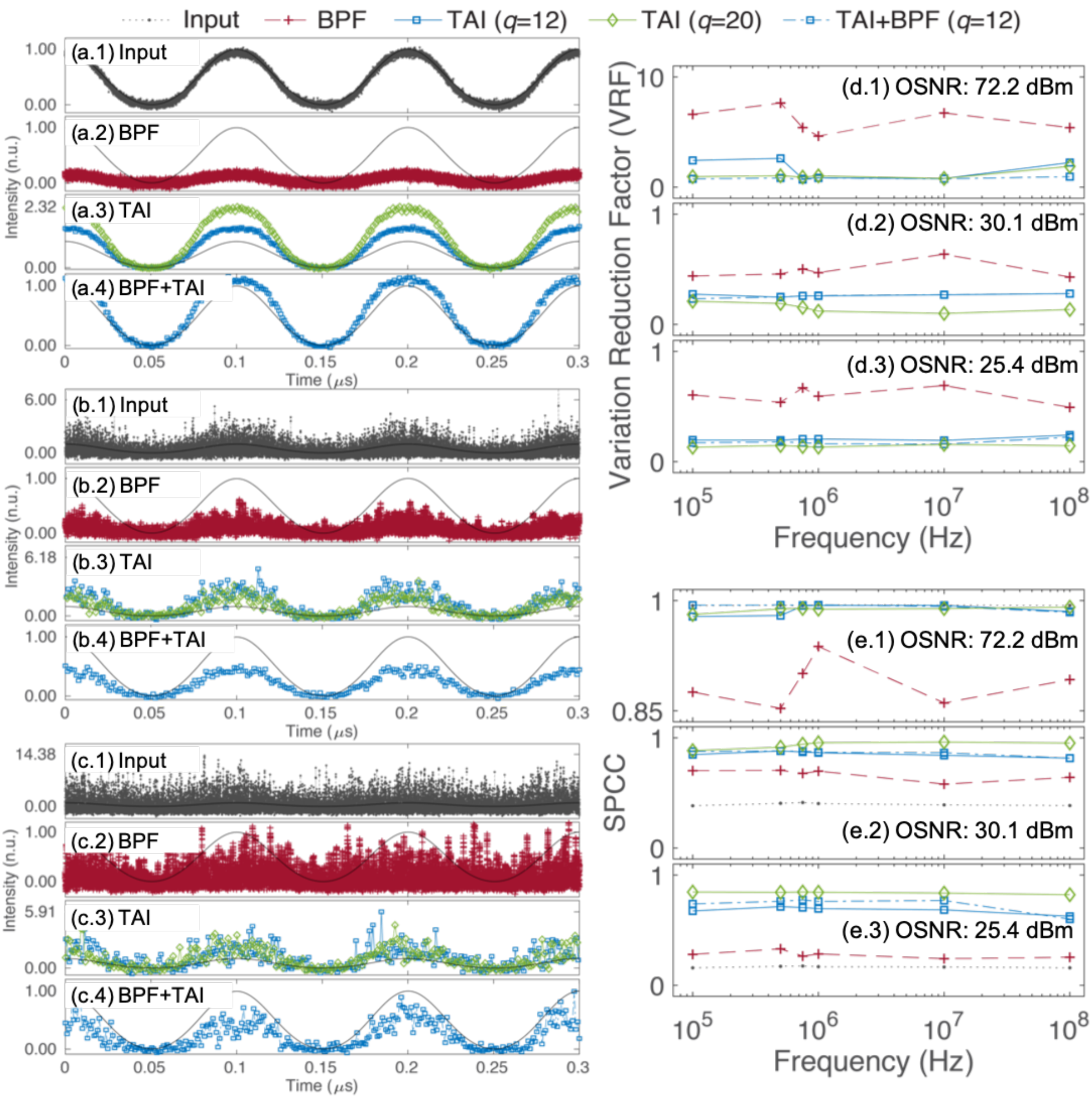

Fig. 4.8 – Results on the recovery of a 2.9 dBm, 10 MHz tone using different noise mitigation configurations, namely OSNRs of (a) 72.2 dBm, (b) 30.1 dBm and (c) 25.4 dBm. (d-e) Extracted metrics demonstrating the performance of the noise mitigation schemes on single tones.

of an EDFA with no input signal was filtered to a 3 dB bandwidth of about 28 GHz, and then fed to second EDFA (see Fig. 4.2 (a)). Three different levels of noise were injected into the system to test the proposed scheme, namely noise injections of 0 dBm, 5.6 and 11.4 dBm. In all cases, the carrier signal had a power of 2.9 dBm at the input, resulting in OSNRs of 72.2 dBm, 30.1 dBm and 25.4 dBm, respectively. Note that whereas the SNR defined above was taken as simply the ratio of the signal over the noise using the values measured by a power meter, here the OSNR is defined by taking the ratio of the peak power of the carrier signal to that of the noise near the same wavelength, as described in section 4.2, in accordance with conventions used in optical communications.

To recover the signal processed by the T-TAI, the signal is recorded using the detector and real-time oscilloscope mentioned above, and then the value at each peak is interpolated digitally (i.e., the analog signal is reconstructed from the discrete TAI samples). We then tested for four different noise mitigation configurations: using the BPF alone, a T-TAI with $q = 12$, $t_s = 82.5$ ps and $t_q = 990$ ps, a T-TAI with $q = 20$, $t_s = 64.1$ ps and $t_q = 1.282$ ns, and the BPF followed by the T-TAI with $q = 12$. From Fig. 4.8 (a), we can already see the important advantage offered by the simultaneous amplification caused by the Talbot approach, whereas the BPF has an unavoidable considerable insertion loss. As the OSNR is degraded, the signal is visually less noisy for the TAI cases compared to the BPF, showing the superior noise mitigation performance of the T-TAI in addition to the simultaneous amplification.

To objectively asses the performance of the noise mitigation schemes, the SPCC and VRF are determined for each case, depicted in Fig. 4.8 (d) and (e), respectively. The VRF for high SNR case, Fig. 4.8 (d.1), depends only on the change in the mean value of the peaks of the sinusoids, since in this case, $\sigma_{\text{out}} \approx \sigma_{\text{in}}$. Therefore, the lower performance of the BPF is accounted simply by its associated insertion loss. Indeed, this confirms that for an input signal with low noise, bandpass filtering actually leads to a degradation of the signal as indicated by a VRF>1. However, even as the amount of injected noise is increased, the noise mitigation approaches using a TAI maintain a higher performance in terms of signal recovery measured by a lower VRF, indicating a more effective noise mitigation process.

For each noise mitigation configuration shown in Fig. 4.8 (a)-(c), the SPCC was calculated by taking a digitally filtered version of the input with high SNR as a reference. For all cases in Fig. 4.8 (e), we can see that the T-TAI recovers a signal that is more faithful to the reference compared to the BPF, as indicated by a SPCC closer to 1. In particular, the option using both a bandpass filter and a T-TAI with $q = 12$ yields better results than if they are used on their own, but yet this configuration is not as beneficial as using the T-TAI alone with $q = 20$. Note that this metric is independent of any scaling in the amplitude, such that it strictly depends on the relative noise content of the signal. Thus, this figure indicates that the T-TAI has a true noise mitigation advantage in addition to the simultaneous passive amplification, and that a T-TAI with higher amplification factors should be favoured instead of employing a combination of BPF with a TAI of lower amplification factor.

4.5 Noise mitigation of random data signals

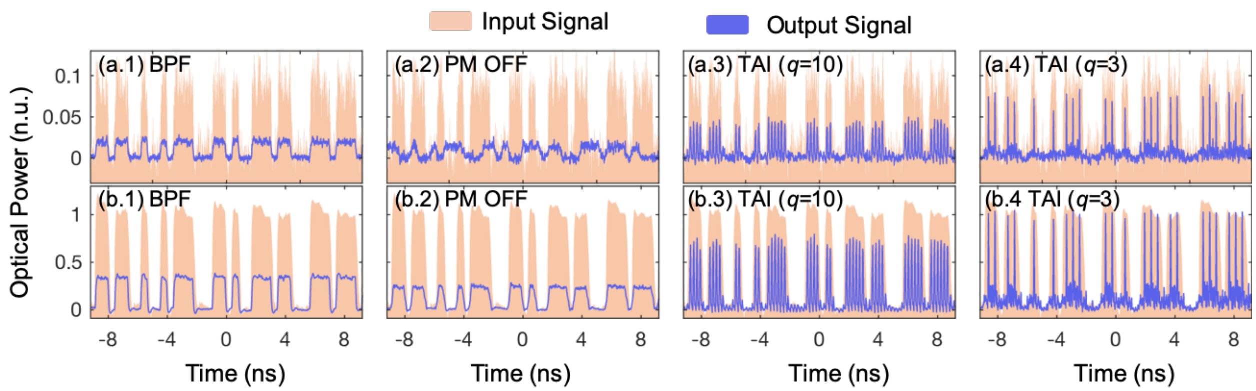

Fig. 4.9 – T-TAI on data signals, with varying amplification factors $q = 3$ and $q = 10$. The input signal is shown in orange for every case, with SNR values of (a) -5.71 dB and (b) 6.5 dB. The PM off cases are measured at the output of the Talbot Amplifier with the phase modulation turned off, indicating the insertion loss of the system.

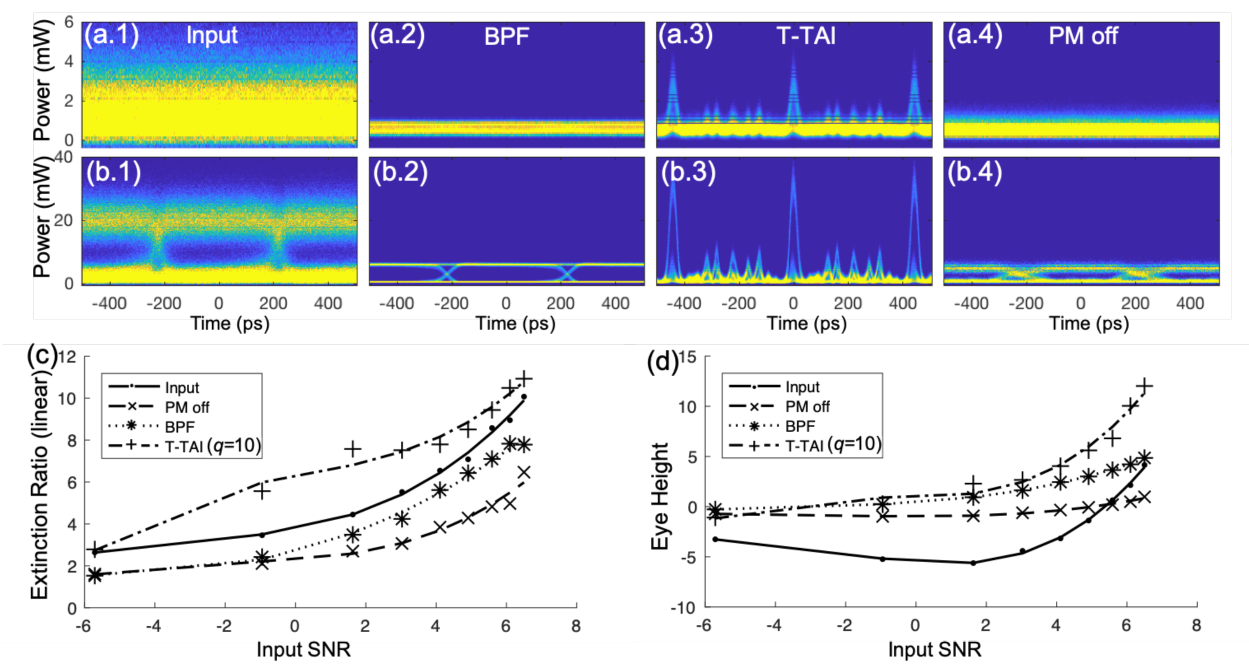

Fig. 4.10 – Eye diagram analysis. The TAI shows improved performance due to the simultaneous amplification, as demonstrated by the extracted metrics. In particular, the Eye Height (d) shows that the T-TAI recovers signal for efficiently than a BPF, with a steeper increase as a function of SNR.

To test the performance of the TAI with a concrete example, we demonstrate its capabilities on a range of different non-return-to-zero (NRZ) data signals, a data signal format commonly used in optical telecommunications. In this case, the phase modulation signal must be aligned with the SUT in order to reach the expected amplification. The data signal is thus converted to a series of peaks by the T-TAI, as depicted in Fig. 4.9 on a 2.27 Gb/s data signal (bit period of 440.6 ps, bandwidth of 66 pm). The setup was prepared for either one or two peaks per bit, corresponding to design parameters of $q = 10$, $t_s = 44.06$ ps and $t_q = 440.6$ ps, and of $q = 3$, $t_s = 73.43$ ps and $t_q = 220.3$ ps, respectively. Since both configurations use the same dispersive line (LCFBG with $D = -2076$ ps/nm, equivalent to 120 km of SMF fiber), the system could be switched between these two configurations by simply changing the phase modulation signal programmed in the AWG. The BPF used in this experiment had a bandpass of 112 pm (13 GHz). As discussed previously, the T-TAI allows to simultaneously amplify the signal while reducing the noise distortion, as demonstrated by the higher peak values achieved in the T-TAI cases. To gain further insight in the quality of these results, we used an optical sampling oscilloscope (OSO) to retrieve the eye diagram from the data signals shown in Fig. 4.9, which is obtained by stacking each bit period on top of each other. From the eye diagrams shown in Fig. 4.10 (a)-(b), we can recovery the extinction ratio and eye height, shown in Fig. 4.10 (c) and (d), respectively. As demonstrated by both metrics, the T-TAI approach has a key advantage due to simultaneous amplification and noise mitigation process.

Finally, to demonstrate the ultra-narrowband filtering capabilities of the T-TAI on data signals, we compared its performance to the same 5 GHz fixed BPF used above on low frequency sinusoids, here for data signals with data rates of 19.5 Mb/s and 195 Mb/s. In this case, the TAI was configured such that $q = 20$, $t_s = 64.1$ ps and $t_q = 1.28$ ns, yielding 40 peaks per bit for the 19.5 Mb/s data signal and 4 peaks per bit for the 195 Mb/s data signal (see Fig. 4.11 (a)-(b)). As in Fig. 4.8, the values at each peak are interpolated in order to recover the processed signal. The high level amplitude, eye opening and SPCC are then extracted from the measured data signals, for the same three different OSNR levels shown above (see Fig. 4.11 (c,d,e)). Note that here, the high level amplitude and eye opening are extracted directly from the data signal rather than the eye diagram. In practically all cases, the TAI approaches show a significantly higher performance than using the BPF alone. Since the high level is mostly an indication of amplitude level, the T-TAI alone evidently shows the highest performance since it does not have the insertion loss associated with the BPF. On the other hand, for noise-sensitive metrics such as the eye opening and the SPCC,

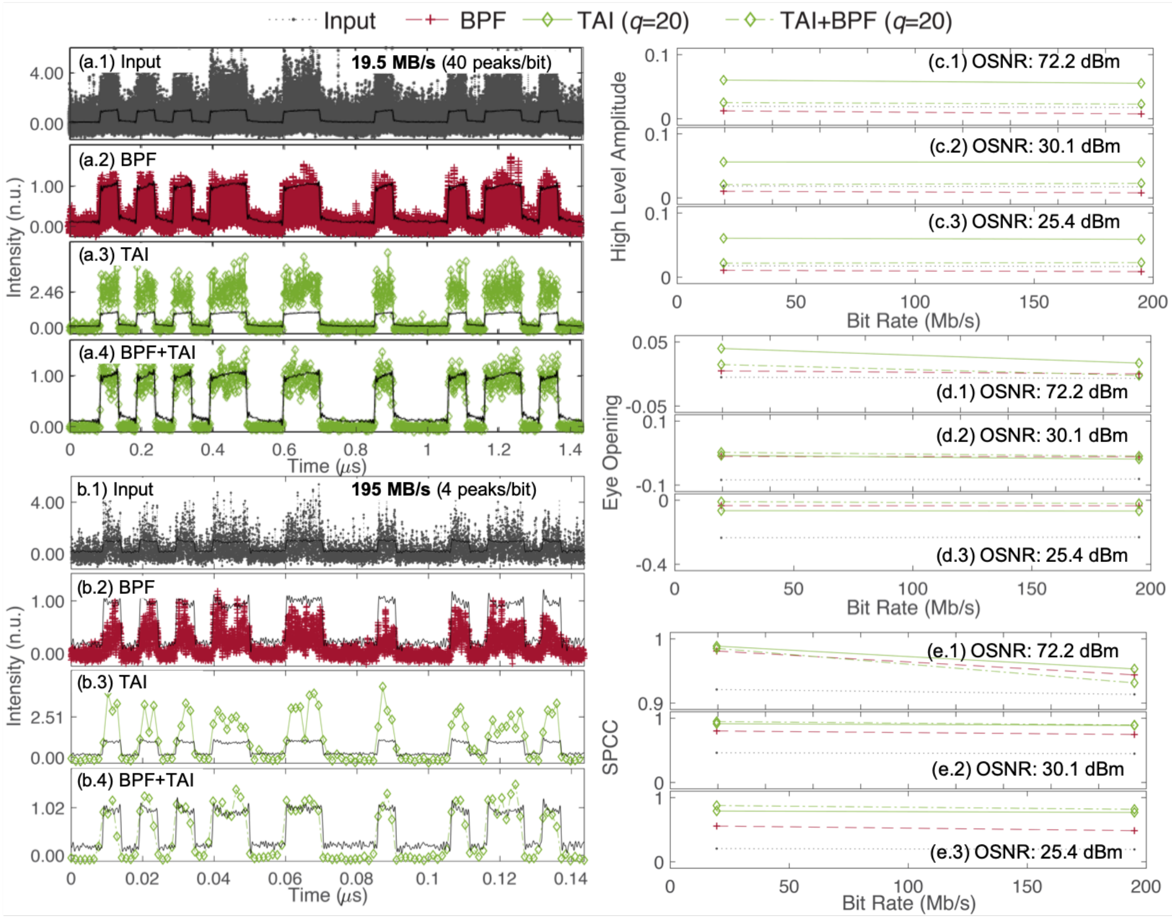

Fig. 4.11 – Extracted metrics demonstrating the performance of the noise mitigation schemes on data signals.

we can see that at low levels of noise, the T-TAI alone shows the best results, but as the noise is increased, the combination of BPF and T-TAI dominates. This observation is in agreement with the conclusions drawn from Fig. 4.8.

Chapter 5

Noise Mitigation of Broadband Signals

The S-TAI can be seen as performing a similar process as the T-TAI shown in chapter 4, but in the spectral domain rather than the temporal domain. Therefore, the S-TAI enables a lossless sampling process of the spectrum of the waveform rather than of its temporal representation, leading to a noise mitigation process directly in the spectral domain. The main advantage, of paramount importance, is that this approach allows to recover a signal that is buried under in-band noise. Thus, it can recover a signal that could not be recovered using typical bandpass filtering schemes. This key contribution is truly significant for the field of signal processing, since it allows to recover signals that may not be recovered by any other means. The potential of the S-TAI is first demonstrated by amplification up to a factor of of 28.8. The versatility of the proposed scheme is then demonstrated by processing spectra of varying shapes, central frequency, and bandwidth. This is followed by the extraction of a signal covered under high amounts of in-band noise. Finally, the single shot nature of the S-TAI is experimentally demonstrated using frequency-to-time mapping in order to show real-time, single shot recovery of signals completely buried under in-band noise. The results presented in this Chapter were reported in [AC4, AC5, AC6].

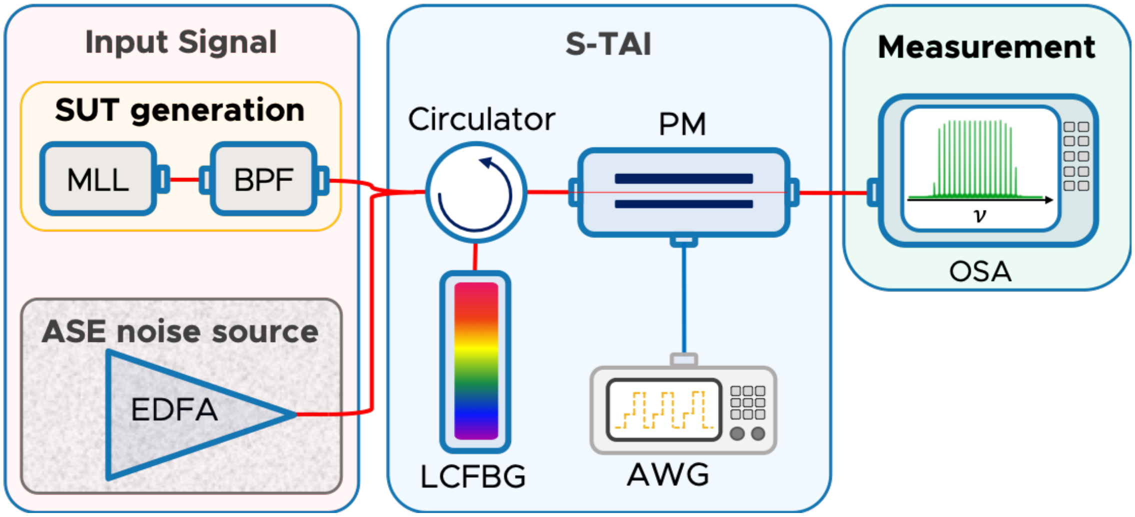

Fig. 5.1 – Experimental setup for the S-TAI. The use of an OSA to capture the waveform simplifies the setup and allows for a high spectral resolution, except that multiple copies of the SUT must by captured in order to reconstruct the spectrum. Therefore, it allows to demonstrate high amplification and recovery from noise, but it is not a single-shot measurement. MLL: Mode Locked Laser, BPF: BandPass Filter, AWG: Arbitrary Waveform Generator, EDFA: Erbium-Doped Fiber Amplifier, PM: Phase Modulator, LCFBG: Linearly Chirped Fiber Bragg Grating, OSA: Optical Spectrum Analyzer.

5.1 Amplification and recovery of arbitrary spectra

5.1.1 Experimental Setup

The experimental setup for demonstration of high spectral amplification using the S-TAI is depicted in Fig. 5.1. The signal was first generated by a mode locked laser (MLL) filtered to the desired bandwidth. The employed MLL was a frequency comb with a repetition rate of 250 MHz [163], decimated down to a repetition rate of 10 MHz to avoid any interference between neighbouring pulses. The generated SUT was then combined with the ASE noise produced by an EDFA for noise mitigation experiments. The signal was then processed by the S-TAI, consisting of a LCFBG with a dispersion $D = -10,000$ ps/nm or $D = -2,076$ ps/nm, followed by a 40 GHz electro-optic Phase Modulator (PM), driven by a Radio-Frequency (RF) Arbitrary Waveform Generator (AWG). The processed waveform is then detected on an Optical Spectrum Analyzer (OSA).

5.1.2 Experimental results

To demonstrate the potential for high amplification of a broadband waveform, we designed the S-TAI for amplification by a factor of $q = 32$ ($\nu_q = 44.8$ GHz and $\nu_s = 1.4$ GHz) on a 400 GHz

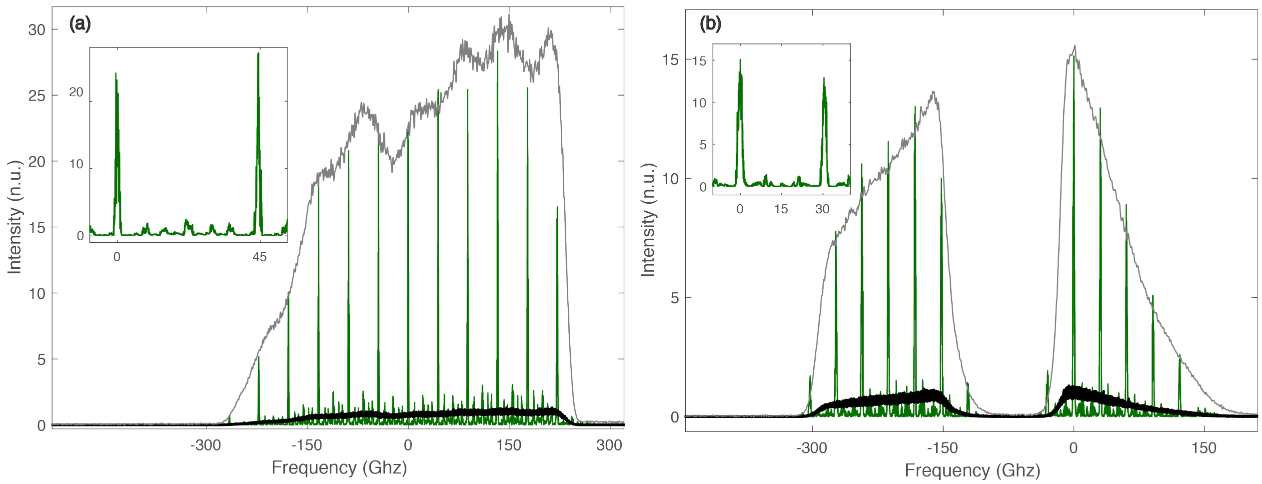

Fig. 5.2 – Basic demonstration of the S-TAI, for (a) a high amplification of 28.8 and (b) reconfigurable spectral resolution.

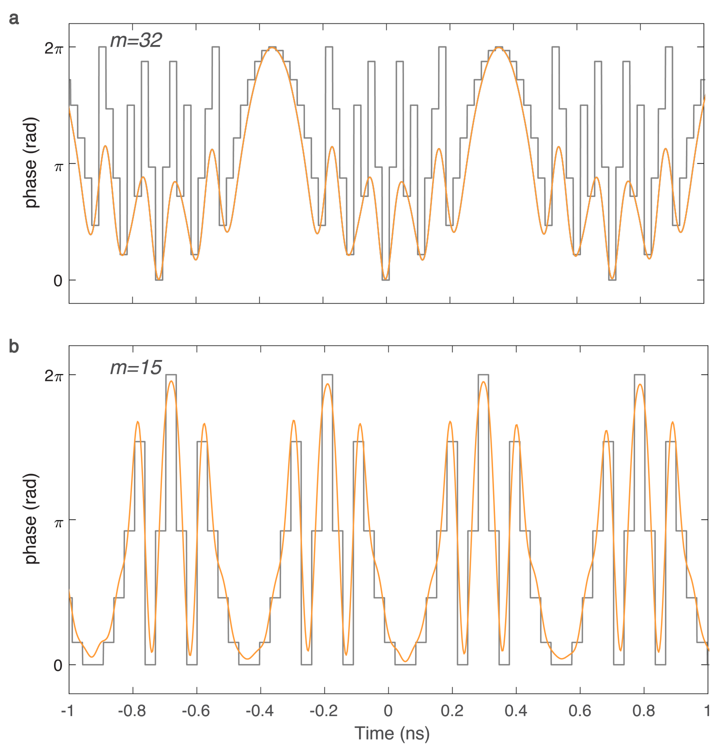

Fig. 5.3 – RF phase pattern for the S-TAI, with the ideal phases (gray) and measured RF voltage of the AWG signal (orange), normalized to 2π, shown for both the (a) $m = 32$ case and the (b) $m = 15$ case. Note that the discrepancy in the $m = 32$ case is due to the limited bandwidth of the employed oscilloscope which was unable to properly resolve the features of the RF signal.

at FWHM broadband waveform, as shown by the intensity measurement in Fig. 5.2 (a), using the temporal phase depicted in Fig. 5.3 (a). The output waveform had a measured amplification of factor of 29.1, a peak separation $\nu_q = 44.4$ Ghz and peak width $\nu_s = 1.6$ GHz. Using the same components, we then reconfigured our system for an amplification factor $q = 15$ by simply programming a different phase pattern into the AWG (see Fig. 5.3 (b)). This allowed to process a more complicated waveform due to the higher spectral resolution resulting from the smaller peak

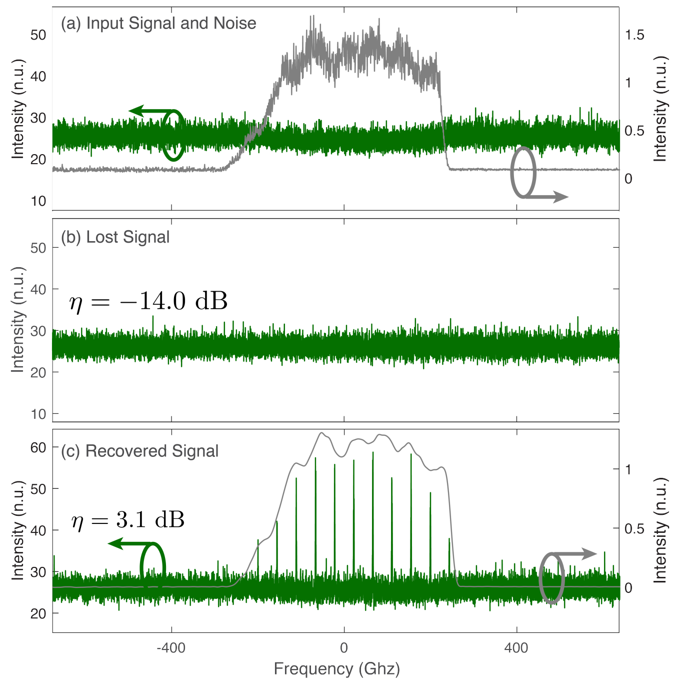

Fig. 5.4 – Recovery of a signal from in-band noise. a) a weak signal with a peak power of $P_S = 1$ n.u. (gray) is combined with $P_N = 25$ n.u. of ASE noise (green), as measured near the location of each output S-TAI peak. b) the signal is totally buried in noise, with a visibility of $\eta = 10\log_{10}(P_S/P_N) = -14dB$. c) The visibility of the signal is increased by a factor of 17.1 dB using the S-TAI, effectively recovering the input waveform. Note that all values are normalized to the value of the input waveform, shown on a linear scale.

separation $\nu_q = 30.1$ GHz, with associated peak width $\nu_s = 2$ GHz. The resulting signal shown in Fig. 5.2 (b) was measured to have an amplification factor $q = 14.4$ with $\nu_q = 30.3$ GHz and $\nu_s = 2.2$ GHz, in close agreement with the expected values. This underlines the advantage of the S-TAI to function regardless of central frequency, bandwidth or shape, proving the versatility of this method for processing different waveforms with virtually no prior knowledge about it.

To demonstrate the unique noise mitigation property capabilities of the TAI, we injected a large amount of ASE noise into the SUT (Fig. 5.4). We may quantify the detectability of the signal under test (SUT) by defining the visibility η as the mean of the ratio of the power P_S of the SUT to that of the noise P_N injected by the EDFA, measured near the location of each output TAI peaks, relative to the noise floor of the SUT:

$$\eta = 10\log_{10}(P_S/P_N). \tag{5.1}$$

The prepared input noisy signal was thus undetectable, with a visibility of -14.0 dB. Using the same parameters as in Fig. 5.2 a), with $q = 30$, the high performance of the S-TAI allowed for an increase of the visibility by 17.1 dB, significantly more than an order of magnitude. The output waveform could then be adequately measured, accurately depicting a sampled version of the original SUT. The S-TAI's ability to function regardless of central frequency and bandwidth

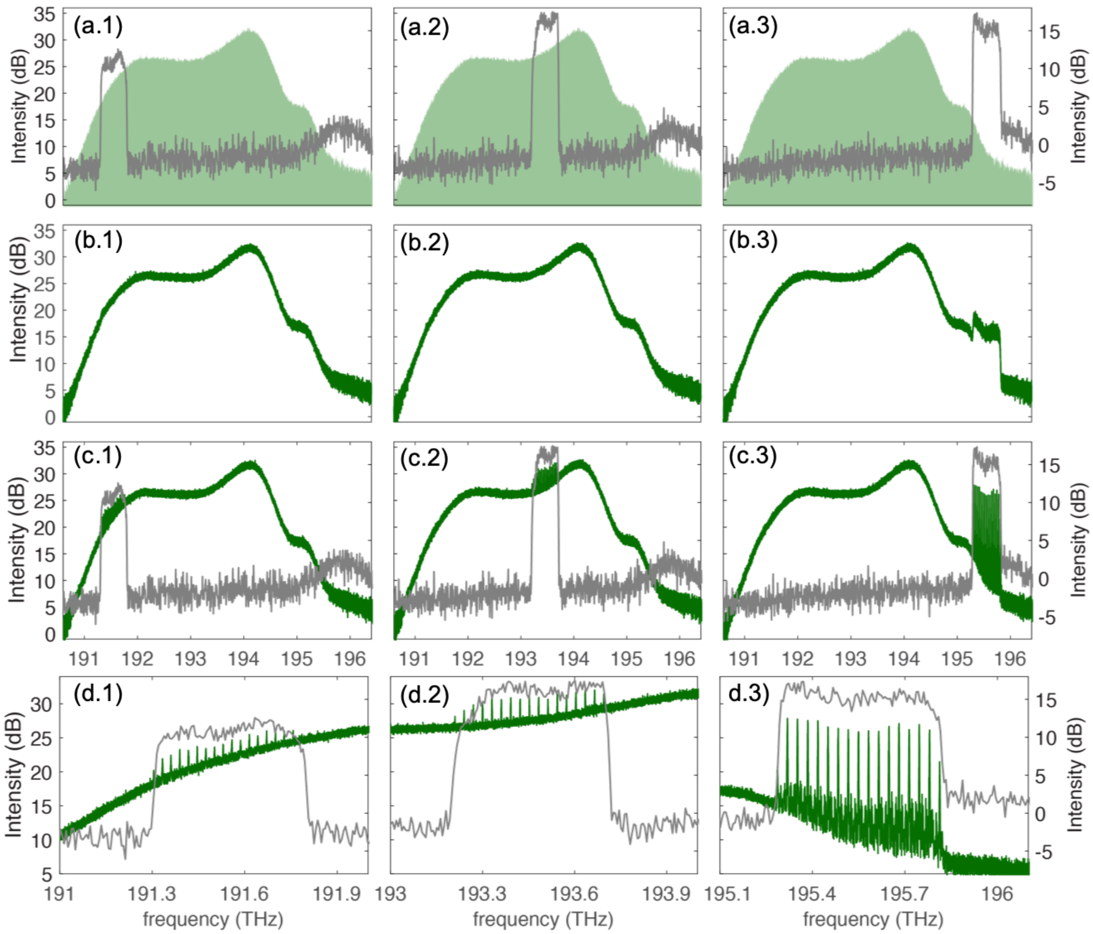

Fig. 5.5 – S-TAI for varying central frequency, with a bandwidth of 446 GHz, centered at 1) 191.5 THz, 2) 193.5 THz and 3) 195.6 THz. (a) a weak signal is generated, such that when combined with the noise, (b) it is buried under in-band noise and undetectable. (c,d) Using the same S-TAI configuration as 5.2 (b), with $q = 15$, these signals are recovered with visibility improvements of 1) 13.12, 2) 14.4 and 3) 9.8 dB.

is further demonstrated by Figs 5.5 and 5.6, showing the recovery of various signal buried under in-band noise.

5.2 Single-shot spectral measurements

5.2.1 Experimental Setup

In order to measure the spectra of the signals of interest in a single-shot, real-time fashion, the OSA was replaced by a Real-Time Optical Fourier Transform (RT-OFT) system, consisting of a LCFBG, an optical detector and an oscilloscope (Fig. 5.7). By propagating a waveform through a total amount of total dispersion $\ddot{\phi}$, it is possible to perform a Fourier transform directly in the

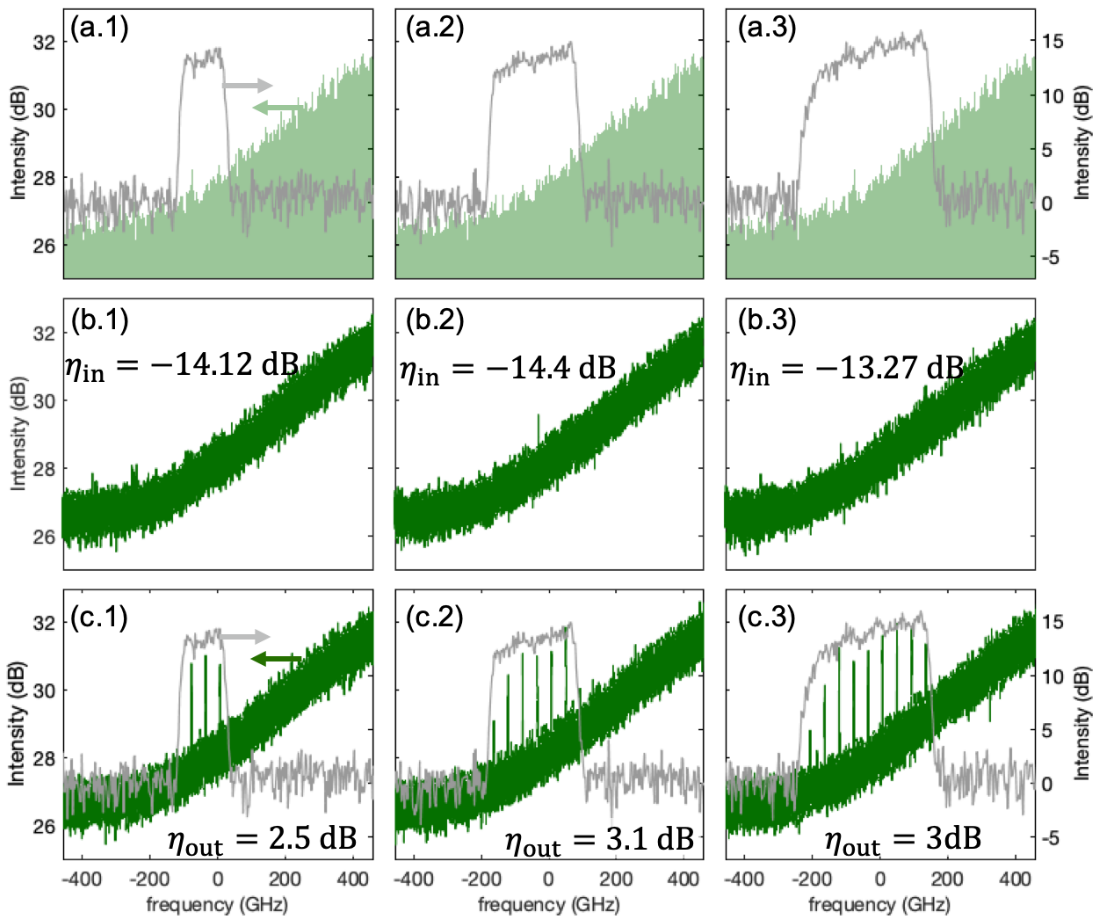

Fig. 5.6 – S-TAI for varying bandwidths, with a central frequency of 193.5 THz and bandwidths of a) 126.7 GHz, 2) 244.3 GHz and 3) 493 GHz. (a) a weak signal is generated, such that when combined with the noise, (b) it is buried under in-band noise and undetectable. (c) Using the same S-TAI configuration as 5.2 (b), with $q = 15$, these signals are recovered with visibility improvements of 1) 16.62, 2) 17.5 and 3) 16.27 dB.

temporal domain, analogous to the spatial phenomenon of Fraunhofer diffraction. In particular, the angular frequency ω of a signal can be mapped directly onto the time domain, in a real time fashion, according to the mapping equation

$$\omega = \frac{t_r}{\ddot{\phi}_0} \tag{5.2}$$

Where t_r is the retarded time, taken relative to the center of the propagating waveform [108, 110]. This was implemented using a LCFBG with total second-order dispersion $D = -10,000$ ps/nm (Proximion) allowing for a mapping of 12.4 GHz per ns, and the waveform was captured with a 50

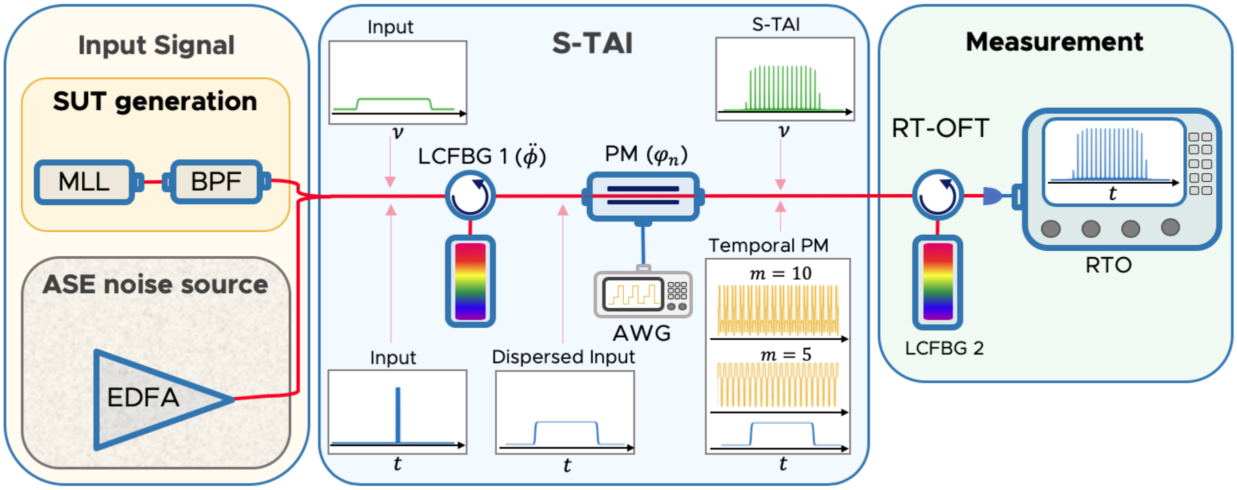

Fig. 5.7 – Experimental setup for the single-shot measurement of the S-TAI. This is done by mapping the spectrum of the waveform directly in the time domain using frequency-to-time mapping by dispersive propagation. Each step of the process is shown in the insets for clarity, showing the signal in the spectral domain (green) and the temporal domain (blue), along with the applied RF signal from the AWG (yellow).

GHz photodetector (PD) (Finisar) connected to a 28 GHz real-time oscilloscope (RTO) (Agilent). The LCFBG used to perform the S-TAI had a second-order dispersion value $D = -2,076$ ps/nm.

5.2.2 Experimental results

The real-time optical Fourier transformation by dispersion-based frequency to time mapping allowed to prove that the S-TAI could be used on aperiodic or isolated waveforms. As depicted in Fig. 5.8, the spectra could be analyzed individually as they reached the detector. In particular, broadband waveforms with a FWHM bandwidth of 400 GHz were generated at a rate of 10 MHz with a relatively high SNR, as depicted in Fig. 5.8 (a.1). The insertion loss caused by the S-TAI module can be seen by measuring the signal at the output of the S-TAI with the phase modulation turned off (Fig. 5.8 (a.2)). The amplification can then be seen from the envelope of the S-TAI peaks by turning on the driving signal on the AWG, proving that it functions in a single-shot manner and in real time, thus applicable to isolated or randomly occurring events (see Fig. 5.8 (a.3)). For this experiment, the S-TAI was designed with $m = 10$, $\nu_s = 2.5$ GHz, and $\nu_m = 24.8$ GHz, The detected waveform had a lower amplification factor than expected of about 6.0, with $\nu_s = 5.1$ GHz, and $\nu_m = 24.6$ GHz, due to limited available dispersion, thus causing a non-optimal spectral representation, as well due to the limited temporal resolution of the oscilloscope.

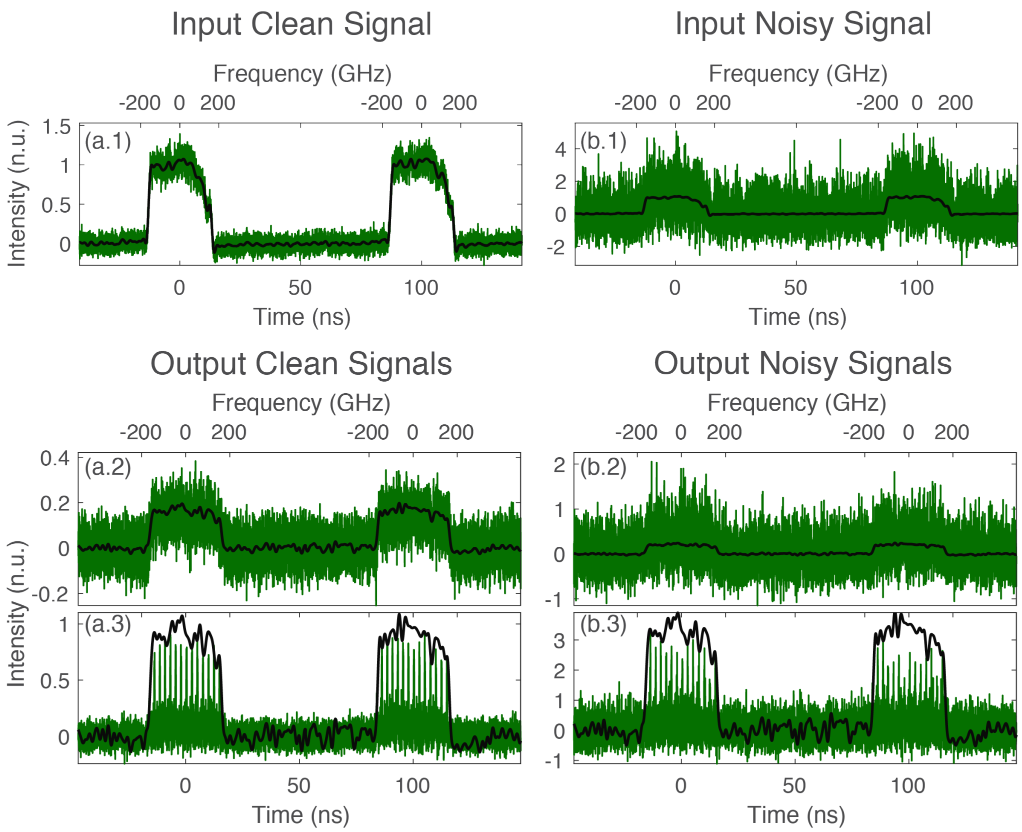

Fig. 5.8 – Real-time, single-shot recovery of signals buried under in-band noise. The spectrum of the incoming waveforms were detected using dispersion-based frequency to time mapping. (a) amplification of relatively clean input waveform using the TAI, showing the value at (a.1) the input, measured at the point before the T-TAI module, (a.2) the output with the phase modulation turned off, indicating the insertion loss of the system, and (a.3) the amplified S-TAI waveform, with the phase modulation turned on. (b) By increasing the amount of noise injected into the system, we could reach a point where (b.1) the signal was buried under noise such that no information about it could be retrieved, as shown in (b.2). By activating the phase modulation signal, shown in (b.3), the S-TAI focused the signal into peaks where the signal was present, such that the signal can now be detected, allowing for real-time detection of subnoise signals in a single-shot manner.

Finally, to show the real-time, single-shot in-noise mitigation capabilities of the S-TAI, a large amount of noise was injected into the signal, such that the SUT was almost entirely buried under in-band noise, as shown by Fig. 5.8 (b.1) and (b.2). By activating the phase modulation driving signal, it is now possible to recover the SUT from the envelope of the S-TAI peaks depicted in Fig. 5.8 (b.3). Thus, we demonstrated the recovery of undetectable isolated single waveforms buried under in-band noise on the fly as they reached the S-TAI, without requiring the specific time of arrival of each pulse. This is a significant advantage as it relieves the constraints on synchronization, which may be a serious important obstacle for the detection of signals caused by randomly occurring events.

Chapter 6

Conclusion and Outlook

The framework presented in this thesis describes a novel method for noise mitigation of arbitrary signals, offering a simple and effective solution to long-standing problems in the field of optical signal processing. It provides a universal solution for the detection of signals of vastly different nature, namely narrowband and broadband signals, by targeting the specific difficulties associated with their respective noise mitigation processes. The ability to effectively amplify a signal while reducing its relative noise content allows for the detections of signals that would be difficult to perceive otherwise due to their low energy content or deterioration due to noise. Furthermore, the fact that the proposed method works in a single-shot manner, without resorting to any kind of digital post-processing, and with practically no prior information about the waveform of interest, makes it suitable for a vast range of applications, including sensing, metrology, telecommunications, spectroscopy and many more.

Furthermore, it is important to note that although all reported results were done in the optical domain, the proposed scheme could theoretically be applied to any wave system. Indeed, the manipulations required to implement a Talbot amplifier (i.e., Dispersion and phase modulation) are common to practically any oscillatory system. Since the issues concerning narrowband and broadband signal noise mitigation concern virtually all areas of science and engineering to a certain degree, it would be interesting to further investigate its implementation in other media. This would include different regions of the electromagnetic spectrum, such as radio-waves, microwaves, mm-waves, X-rays, etc., as well as other physical mechanisms, including plasmonics and acoustics, amongst others. One should also keep in mind that the proposed method could be exploited for intents other than noise mitigation, such as for narrow pulse generation or spectral shaping, leaving a plethora of opportunities to be explored.

6.1 Future work

As a general conclusion, this section presents future lines of work concerning the theoretical or practical implementation of the noiseless amplifier presented in this thesis.

6.1.1 Development towards higher amplification factors

The performance of the noise mitigation process presented in this thesis relies on reaching high amplification factors. Thus, appreciable noise mitigation is achieved when factors of at least $q = 10$ are achieved, but the most impressive performances result from amplification factors above 20. Although there is no fundamental limitation on the maximum amplification factor that can be reached with a Talbot amplifier, experiments have so-far been limited to factors near $q = 30$. As mentioned in Chapter 3, one potential avenue would be to further investigate the impact of the bit resolution of the employed AWG. Alternatively, the non-ideal response of the dispersive line may also have an impact. Since the performance of a Talbot amplifier is so closely linked with the amplification factor, further investigation into much higher factors, on the order of $q = 100$ or more, would allow to extract signals buried under even higher amounts of noise.

6.1.2 Signal phase recovery

The Talbot amplifier developed in this thesis should theoretically preserve any phase information contained in the input waveform, so long as the peaks satisfy the usual sampling theorem with respect to the shape of the phase. Thus, it should be possible to extract the full field information, allowing to completely reconstruct the waveform in both the time and frequency domains. For the T-TAI, this could lead to interesting application with complex modulation formats often used in telecommunications, such as Quadrature Amplitude Modulation (QAM) signals. Concerning the S-TAI, the recovery of the full complex field would allow to reconstruct waveforms with very high temporal resolution in the sub-picosecond range.

6.1.3 Application to spatial images

This research line would be a return to the early application of the TAI in the spatial domain. However, as mentioned in Chapter 3, spatial TAI were never used in the context of noise mitigation or amplification of spatial images. Thus it would be a natural extension of the work to conceive an apparatus consisting of a phase mask and diffractive propagation for denoising spatial images. This could find interesting applications in imaging by conceiving a signal enhancement device that can conveniently be added on to any camera.

6.1.4 On-chip integration

On-chip integration is the ultimate step of the development of any signal processing scheme, as it allows the concept to be conveniently included in a practical instrument where large components cannot be used, for example, in the detection system of a satellite or drone. Considering that the employed components in the work presented here are quite bulky, the proposed scheme would need to be packaged into a small device for widespread application. In particular, the RF AWG needed to supply the phase modulation pattern can be heavy and very expensive (up to 500k USD or more). It should be possible to design the pattern generator specifically for the required Talbot phases, which would greatly reduce its size, cost and power consumption. Fortunately, the development of integrated phase modulators has been the subject of much research in recent years, such that integrated phase modulators with bandwidths in excess of 100 GHz are now available[164]. On the other hand, the development of on-chip broadband dispersive lines or spectral phase masks with high spectral resolution remains elusive [165, 166, 167]. Such elements have been sought after for a long time as they would allow for integrated methods for many other signal processing operations, such as pulse shaping and dispersion compensation [168, 169, 170, 171, 172] . Thus, the starting point for any Talbot-based integrated amplifier should first consist of the development of an efficient spectral phase filtering device.

6.1.5 Further investigation of the Talbot phases

Significant insight into the nature of the phases involved in the Talbot effect have been gained in recent years [137, 139]. The formalism put forward by these authors shows a simple form for the relation between the Talbot phases between Fourier domains. However, the symmetry between these phases could be taken one step further by modifying the presented mathematical derivation, such as to avoid the $(1 + qe_q)$ factor. This factor arises from the truncation of the phase sequence to a range from 0 to $q - 1$. Indeed, if the sequence is instead truncated from 0 to $2q - 1$, reflecting the periodicity of the carpet, then the $(1 + qe_q)$ factor can be omitted, leading to the DFT pair

$$\begin{aligned} x_n \equiv e^{i\theta_n} = e^{i\sigma_\phi c} \exp\left(i\pi\sigma_\phi \frac{s}{q} n^2\right) \xrightarrow{\text{DFT}} \\ X_m \equiv e^{i\Theta_m} = \sqrt{q} \exp\left(-i\pi\sigma_\phi \frac{p}{q} m^2\right). \end{aligned} \tag{6.1}$$

Similarly, if the n index is taken from $-\infty$ to $+\infty$, this factor can also be omitted.

Another interesting subject for investigation concerning the form of the Talbot phases concerns the equivalence between a discrete and a continuous phase modulation. As discussed in section 2.3, the form of the phase modulation has little impact for periodic signals, but this impact is more noticeable when it comes to continuous, aperiodic waveform, such as those encountered in the TAI. Further investigation on this subject could also lead to a deeper insight into the noise mitigation principle of the TAI.

6.1.6 Application to low-photon signals and quantum information processing

As mentioned above, the proposed technique relies only on common wave manipulations, and thus could find application in virtually all wave systems. A particularly interesting application for the Talbot amplifier would be to investigate its potential for quantum systems. A relatively simple quantum platform where the passive amplification scheme could be readily investigated is the low photon regime, including single-photons or entangled-photons systems. Indeed, measurements on quantum waveforms face difficulties due to the long integration time required to reconstruct a wavefunction from single photon detection events. Thus, it is common for low photon experiments to extend over many hours or even several days to complete a given measurement. This is not only impractical in an experimental context, but also limits the potential application of quantum optics to commercial or technological sectors where measurements are expected to be completed in a time on the order of milliseconds or less. Thus, the use of the passive amplification scheme proposed here would allow to drastically reduce the integration time of few photon measurements. This would have a direct impact in the field of quantum information [173], which includes research on quantum computing [174, 175] and ultra-secure communication [176]. However, the enhancement of single photon detectors using a Talbot amplifier would also extend far outside of the field of quantum information, leading to a measurable impact in distinct fields such as in clinical medical procedures [177, 178], biomedical imaging [179, 13, 180], for ranging and sensing applications including LiDAR (Light Imaging And Ranging) [181, 182, 183, 184, 185, 186, 187], non-line of sight imaging [188], light-in-flight imaging [58], fluorescence-lifetime spectroscopy [189, 190], single molecule detection [191], DNA sequencing [192], as well as astronomical ground and satellite-based observation [193, 194], amongst many others.

Associated Publications in International Conferences

[AC1] B. Crockett, L. Romero Cortés, and J. Azaña, "Denoising Amplification of Arbitrary Optical Waveforms by Linear Coherent Energy Redistribution," in *Advanced Photonics 2018 (BGPP, IPR, NP, NOMA, Sensors, Networks, SPPCom, SOF)* (Zurich, Switzerland, 2018), SpW2G.3.

[AC2] B. Crockett, L. Romero Cortés, and J. Azaña, "Noise Mitigation of Random Data Signals Through Linear Temporal Sampling Based on the Talbot Effect," in *2019 Optical Fiber Communications Conference and Exhibition (OFC)* (San Diego, USA, 2019), M1B.2.

[AC3] B. Crockett, L. Romero Cortés, and J. Azaña, "Noise Mitigation of Narrowband Optical Signals Through Lossless Sampling," in *2019 European Conference on Optical Communication (ECOC)* (Dublin, Ireland, 2019), Tu.2.C.4.

[AC4] B. Crockett, L. Romero Cortés, and J. Azaña, "On-the-fly Recovery of Arbitrary Waveforms from In-band Noise by Linear Coherent Spectral Energy Re-distribution," in *Conference on Lasers and Electro-Optics (2018)* (San José, USA, 2018), SF3N.7.

[AC5] B. Crockett, L. Romero Cortés, S. R. Konatham, and J. Azaña, "On-the-fly Spectral Noise Mitigation through Passive Amplification and Sampling," in *2019 Photonics North (PN)* (Montréal, Canada, 2019).

[AC6] B. Crockett, L. Romero Cortés, S. R. Konatham, and J. Azaña, "Single-shot Subnoise Signal Recovery by Coherent Spectral Energy Redistribution," in *Conference on Lasers and Electro-Optics (2019)* (San José, USA, 2019), JW2A.71.

Other Contributions to International Conferences

[OC1] S. Kaushal, D. Onori, B. Crockett, and J. Azaña, “Passive All-optical Flat-Top Filter using Multimode Waveguide Bragg Gratings in Silicon,” in *2019 24th OptoElectronics and Communications Conference (OECC) and 2019 International Conference on Photonics in Switching and Computing (PSC)* (Fukuoka, Japan, 2019), WP4–E9.

[OC2] S. R. Konatham, B. Crockett, L. Romero Cortés, and J. Azaña, “On-the-fly Continuous Time Varying Frequency Filtering of Broadband Microwave Signals,” in *2019 European Conference on Optical Communication (ECOC)* (Dublin, Ireland, 2019), Tu.2.C.3.

[OC3] D. Onori, B. Crockett, A. Samani, D. V. Plant, and J. Azaña, “0–40 GHz-Tunable RF Receivers on Chip exploiting a Noise-Cancelling Architecture and a Silicon Photonic Modulator,” in *2019 Optical Fiber Communications Conference and Exhibition (OFC)* (San Diego, USA, 2019), Tu3l.1.

Patent

[P1] B. Crockett, L. Romero Cortés, and J. Azaña, “Method and system for denoising amplification of a signal,” US Provisional Patent.

References

[1] A. R. Liddle and M. Cortês, "Cosmic Microwave Background Anomalies in an Open Universe," Physical Review Letters **111** (2013).

[2] R. A. Battye and A. Moss, "Evidence for Massive Neutrinos from Cosmic Microwave Background and Lensing Observations," Physical Review Letters **112** (2014).

[3] A. J. Levan, N. R. Tanvir, S. B. Cenko *et al.*, "An Extremely Luminous Panchromatic Outburst from the Nucleus of a Distant Galaxy," Science **333**, 199–202 (2011).

[4] P. G. Pérez-González, A. Cava, G. Barro *et al.*, "SHARDS: AN OPTICAL SPECTRO-PHOTOMETRIC SURVEY OF DISTANT GALAXIES," The Astrophysical Journal **762**, 46 (2013).

[5] P.-A. Duc, J.-C. Cuillandre, E. Karabal *et al.*, "The ATLAS3D project – XXIX. The new look of early-type galaxies and surrounding fields disclosed by extremely deep optical images," Monthly Notices of the Royal Astronomical Society **446**, 120–143 (2015).

[6] D. Brinks, R. Hildner, E. M. H. P. van Dijk *et al.*, "Ultrafast dynamics of single molecules," Chem. Soc. Rev. **43**, 2476–2491 (2014).

[7] E. Goulielmakis, Z.-H. Loh, A. Wirth *et al.*, "Real-time observation of valence electron motion," Nature **466**, 739–743 (2010).

[8] C. DeCusatis, *Handbook of Fiber Optic Data Communication: A Practical Guide to Optical Networking* (Elsevier Science, 2013).

[9] F. Xiao, J. E. Farrell, P. B. Catrysse, and B. Wandell, "Mobile Imaging: The big challenge of the small pixel," in *IS&T/SPIE Electronic Imaging*, B. G. Rodricks and S. E. Süsstrunk, eds. (San Jose, CA, 2009), 72500K.

[10] S. V.Vaseghi, *Advanced Digital Signal Processing and Noise Reduction* (2000), john wiley & sons ltd ed.

[11] G. Vasilescu, *Electronic Noise and Interfering Signals*, Signals and Communication Technology (Springer, 2005).

[12] S. Weiss, "Fluorescence Spectroscopy of Single Biomolecules," Science **283**, 1676–1683 (1999).

[13] N. G. Horton, K. Wang, D. Kobat *et al.*, "In vivo three-photon microscopy of subcortical structures within an intact mouse brain," Nature Photonics **7**, 205–209 (2013).

[14] A. Raman, "On the Signal Processing Operations in LIGO signals," 2018 IEEE Global Conference on Signal and Information Processing (GlobalSIP) 1086–1090 (2018).

[15] V. A. Galievsky, A. S. Stasheuski, and S. N. Krylov, "Improvement of LOD in Fluorescence Detection with Spectrally Nonuniform Background by Optimization of Emission Filtering," Analytical Chemistry **89**, 11122–11128 (2017).

[16] A. Demir, "Noise analysis for optical fiber communication systems," in *ICCAD-2003. International Conference on Computer Aided Design (IEEE Cat. No.03CH37486)* (IEEE, San Jose, CA, USA, 2003), 441–445.

[17] S. L. Olsson, H. Eliasson, E. Astra, M. Karlsson, and P. A. Andrekson, "Long-haul optical transmission link using low-noise phase-sensitive amplifiers," Nature Communications **9** (2018).

[18] M. Mazalkova, "The Laser Satellites Communications and Laser Noises," **7**, 10 (2008).

[19] V. Ataie, D. Esman, B. P.-P. Kuo, N. Alic, and S. Radic, "Subnoise detection of a fast random event," Science **350**, 1343–1346 (2015).

[20] S. Bottacchi, *Noise and Signal Interference in Optical Fiber Transmission Systems* (John Wiley & Sons, Ltd, Chichester, UK, 2008).

[21] W. K. Wootters and W. H. Zurek, "A single quantum cannot be cloned," Nature **299**, 802–803 (1982).

[22] C. M. Caves, "Quantum limits on noise in linear amplifiers," Physical Review D **26**, 1817–1839 (1982).

[23] A. Zavatta, J. Fiurášek, and M. Bellini, "A high-fidelity noiseless amplifier for quantum light states," Nature Photonics **5**, 52–60 (2010).

[24] Z. Tong, C. Lundström, P. A. Andrekson *et al.*, "Towards ultrasensitive optical links enabled by low-noise phase-sensitive amplifiers," Nature Photonics **5**, 430–436 (2011).

[25] D. Levandovsky, M. Vasilyev, and P. Kumar, "Amplitude squeezing of light by means of a phase-sensitive fiber parametric amplifier," Optics Letters **24**, 984 (1999).

[26] W. Imajuku, A. Takada, and Y. Yamabayashi, "Low-noise amplification under the 3 dB noise figure in high-gain phase-sensitive fibre amplifier," Electronics Letters **35**, 1954–1955 (1999).

[27] S. L. I. Olsson, B. Corcoran, C. Lundstrom *et al.*, "Phase-Sensitive Amplified Transmission Links for Improved Sensitivity and Nonlinearity Tolerance," Journal of Lightwave Technology **33**, 710–721 (2015).

[28] J. Sabines-Chesterking, R. Whittaker, S. K. Joshi *et al.*, "Sub-Shot-Noise Transmission Measurement Enabled by Active Feed-Forward of Heralded Single Photons," Physical Review Applied **8** (2017).

[29] D. F. Walls, "Squeezed states of light," Nature **306**, 141–146 (1983).

[30] C. M. Caves, "Quantum-mechanical noise in an interferometer," Physical Review D **23**, 1693–1708 (1981).

[31] Z. Tong and S. Radic, "Low-noise optical amplification and signal processing in parametric devices," Advances in Optics and Photonics **5**, 318 (2013).

[32] J. Capmany, B. Ortega, and D. Pastor, "A tutorial on microwave photonic filters," Journal of Lightwave Technology **24**, 201–229 (2006).

[33] J. Capmany and D. Novak, "Microwave photonics combines two worlds," Nature Photonics **1**, 319–330 (2007).

[34] A. Agarwal, T. Banwell, and T. K. Woodward, "Optically Filtered Microwave Photonic Links for RF Signal Processing Applications," Journal of Lightwave Technology **29**, 2394–2401 (2011).

[35] L. Li, X. Yi, S. Song *et al.*, "Microwave Photonic Signal Processing and Sensing Based on Optical Filtering," Applied Sciences **9**, 163 (2019).

[36] J. Yao, "Microwave Photonics," Journal of Lightwave Technology **27**, 314–335 (2009).

[37] R. Kaur and S. Dewra, "Performance Evaluation of Passive Optical Network Using Different Modulation Formats," Journal of Optical Communications **37** (2016).

[38] J. G. V. Teixeira, I. T. Leite, S. Silva, and O. Frazão, "Advanced fiber-optic acoustic sensors," Photonic Sensors **4**, 198–208 (2014).

[39] H. Guo, G. Xiao, N. Mrad, and J. Yao, "Fiber Optic Sensors for Structural Health Monitoring of Air Platforms," Sensors **11**, 3687–3705 (2011).

[40] G. Wild and S. Hinckley, "Acousto-Ultrasonic Optical Fiber Sensors: Overview and State-of-the-Art," IEEE Sensors Journal **8**, 1184–1193 (2008).

[41] O. M. Moreschi, "Convenient filtering techniques for LIGO strain of the GW150914 event," Journal of Cosmology and Astroparticle Physics **2019**, 032–032 (2019).

[42] A. S. Daryoush, "RF and Microwave Photonic techniques in biomedical applications," in *2009 IEEE Sarnoff Symposium* (2009), 1–6.

[43] P. Damborsky, J. vitel, and J. Katrlik, "Optical biosensors," Essays In Biochemistry **60**, 91–100 (2016).

[44] P. F. McManamon, "Review of ladar: A historic, yet emerging, sensor technology with rich phenomenology," Optical Engineering **51**, 060901 (2012).

[45] C. V. Poulton, A. Yaacobi, D. B. Cole *et al.*, "Coherent solid-state LIDAR with silicon photonic optical phased arrays," Optics Letters **42**, 4091 (2017).

[46] J. Capmany, B. Ortega, and D. Pastor, "Fibre optic bandpass filter with subpicometre bandwidth using a fibre grating and two fibre Fabry-Perot filters," Electronics Letters **33**, 1970–1972 (1997).

[47] J. Capmany, J. Mora, I. Gasulla *et al.*, "Microwave Photonic Signal Processing," Journal of Lightwave Technology **31**, 571–586 (2013).

[48] M. Burla, B. Crockett, L. Chrostowski, and J. Azaña, "Ultra-high Q multimode waveguide ring resonators for microwave photonics signal processing," (IEEE, 2015), 1–4.

[49] J. Yao, “Photonics to the Rescue: A Fresh Look at Microwave Photonic Filters,” IEEE Microwave Magazine **16**, 46–60 (2015).

[50] X. Yi, S. Song, S. X. Chew *et al.*, “Optical Filtering Techniques for Microwave Photonics,” in *Asia Communications and Photonics Conference 2016* (OSA, Wuhan, 2016), AS3G.5.

[51] S. Song, S. X. Chew, X. Yi, L. Nguyen, and R. A. Minasian, “Tunable Single-Passband Microwave Photonic Filter Based on Integrated Optical Double Notch Filter,” Journal of Lightwave Technology **36**, 4557–4564 (2018).

[52] S. Hu, L. Li, X. Yi, and C. Yu, “Ultraflat Widely Tuned Single Bandpass Filter Based on Stimulated Brillouin Scattering,” IEEE Photonics Technology Letters **26**, 1466–1469 (2014).

[53] W. T. Wang, J. G. Liu, W. H. Sun *et al.*, “Widely tunable single bandpass microwave photonic filter based on Brillouin-assisted optical carrier recovery,” Optics Express **22**, 29304 (2014).

[54] D. Marpaung, B. Morrison, M. Pagani *et al.*, “Low-power, chip-based stimulated Brillouin scattering microwave photonic filter with ultrahigh selectivity,” Optica **2**, 76 (2015).

[55] B. J. Eggleton, C. G. Poulton, P. T. Rakich, M. J. Steel, and G. Bahl, “Brillouin integrated photonics,” Nature Photonics (2019).

[56] M. Pelusi, T. Inoue, and S. Namiki, “Carrier to Noise Ratio Improvement by Brillouin Amplification for 64-QAM Coherent Communications,” in *Optical Fiber Communication Conference (OFC) 2019* (OSA, San Diego, California, 2019), M1B.7.

[57] Y. Liu, D. Marpaung, A. Choudhary, and B. J. Eggleton, “Lossless and high-resolution RF photonic notch filter,” Optics Letters **41**, 5306 (2016).

[58] G. Gariepy, N. Krstajić, R. Henderson *et al.*, “Single-photon sensitive light-in-fight imaging,” Nature Communications **6** (2015).

[59] O. Wada, “Femtosecond all-optical devices for ultrafast communication and signal processing,” New Journal of Physics **6**, 183–183 (2004).

[60] C. C. Chan, *Optical Performance Monitoring* (Academic House, 2010).

[61] C. Dorrer, “High-speed measurements for optical telecommunication systems,” IEEE Journal of Selected Topics in Quantum Electronics **12**, 843–858 (2006).

[62] A. Miller, D. Reid, and D. Finlayson, *Ultrafast Photonics* (CRC Press, 2019).

[63] T. H. Hankins, J. S. Kern, J. C. Weatherall, and J. A. Eilek, “Nanosecond radio bursts from strong plasma turbulence in the Crab pulsar,” Nature **422**, 141–143 (2003).

[64] W. van Straten and M. Bailes, “DSPSR: Digital Signal Processing Software for Pulsar Astronomy,” Publications of the Astronomical Society of Australia **28**, 1–14 (2011).

[65] J. A. Eilek and T. H. Hankins, “Radio emission physics in the Crab pulsar,” Journal of Plasma Physics **82** (2016).

[66] L. G. Spitler, P. Scholz, J. W. T. Hessels *et al.*, “A repeating fast radio burst,” Nature **531**, 202–205 (2016).

[67] E. Petroff, J. W. T. Hessels, and D. R. Lorimer, “Fast radio bursts,” The Astronomy and Astrophysics Review **27** (2019).

[68] J. R. Lakowicz and B. R. Masters, “Principles of Fluorescence Spectroscopy, Third Edition,” Journal of Biomedical Optics **13**, 029901 (2008).

[69] D. G. Ouzounov, T. Wang, M. Wang *et al.*, “In vivo three-photon imaging of activity of GCaMP6-labeled neurons deep in intact mouse brain,” Nature Methods **14**, 388–390 (2017).

[70] H. Maki, T. Toda, S. Sakti, G. Neubig, and S. Nakamura, “EEG signal enhancement using multi-channel wiener filter with a spatial correlation prior,” in *2015 IEEE International Conference on Acoustics, Speech and Signal Processing (ICASSP)* (IEEE, South Brisbane, Queensland, Australia, 2015), 2639–2643.

[71] J. Benesty, *Noise Reduction in Speech Processing*, no. v. 2 in Springer Topics in Signal Processing (Springer, Dordrecht ; London ; New York, 2009).

[72] N. Upadhyay and A. Karmakar, “Speech Enhancement using Spectral Subtraction-type Algorithms: A Comparison and Simulation Study,” Procedia Computer Science **54**, 574–584 (2015).

[73] B. Ergen, “Signal and Image Denoising Using Wavelet Transform,” in *Advances in Wavelet Theory and Their Applications in Engineering, Physics and Technology*, D. Baleanu, ed. (InTech, 2012).

[74] J. Dron, F. Bolaers, and l. Rasolofondraibe, “Improvement of the sensitivity of the scalar indicators (crest factor, kurtosis) using a de-noising method by spectral subtraction: Application to the detection of defects in ball bearings,” Journal of Sound and Vibration **270**, 61–73 (2004).

[75] I. S. Bozchalooi and M. Liang, “A joint resonance frequency estimation and in-band noise reduction method for enhancing the detectability of bearing fault signals,” Mechanical Systems and Signal Processing **22**, 915–933 (2008).

[76] R. Walden, “Analog-to-digital converter survey and analysis,” IEEE Journal on Selected Areas in Communications **17**, 539–550 (1999).

[77] J. Wang, J. Ma, P. Yuan *et al.*, “In-Band Noise Filtering via Spatio-Spectral Coupling,” Laser & Photonics Reviews **12**, 1700316 (2018).

[78] M. Vasilyev, “Matched filtering of ultrashort pulses,” Science **350**, 1314–1315 (2015).

[79] D. Esman, V. Ataie, B. P.-P. Kuo, N. Alic, and S. Radic, “Subnoise Signal Detection and Communication,” Journal of Lightwave Technology **34**, 5214–5219 (2016).

[80] D. J. Esman, V. Ataie, B. P.-P. Kuo *et al.*, “Detection of Fast Transient Events in a Noisy Background,” Journal of Lightwave Technology **34**, 5669–5674 (2016).

[81] D. J. Griffiths, *Introduction to Electrodynamics* (Pearson, Boston, 2013), fourth edition ed.

[82] M. S. Chapman, C. R. Ekstrom, T. D. Hammond *et al.*, “Near-field imaging of atom diffraction gratings: The atomic Talbot effect,” Physical Review A **51**, R14–R17 (1995).

[83] L. Deng, E. W. Hagley, J. Denschlag *et al.*, “Temporal, Matter-Wave-Dispersion Talbot Effect,” Physical Review Letters **83**, 5407–5411 (1999).

[84] J. Ruostekoski, B. Kneer, W. P. Schleich, and G. Rempe, “Interference of a Bose-Einstein condensate in a hard-wall trap: From the nonlinear Talbot effect to the formation of vorticity,” Physical Review A **63** (2001).

[85] F. Saif, “Talbot effect with matter waves,” Laser Physics **22**, 1874–1878 (2012).

[86] X.-B. Song, H.-B. Wang, J. Xiong *et al.*, “Experimental Observation of Quantum Talbot Effects,” Physical Review Letters **107** (2011).

[87] M. R. Dennis, N. I. Zheludev, and F. J. García de Abajo, “The plasmon Talbot effect,” Optics Express **15**, 9692 (2007).

[88] Y. Yu, D. Chassaing, T. Scherer, B. Landenberger, and H. Zappe, “The Focusing and Talbot Effect of Periodic Arrays of Metallic Nanoapertures in High-Index Medium,” Plasmonics **8**, 723–732 (2013).

[89] A. Berezovski, W.-X. Tang, and W. Wan, “Elastic wave Talbot effect in solids with inclusions,” Mechanics Research Communications **60**, 21–26 (2014).

[90] A. French, *Vibrations and Waves*, M.I.T. Introductory Physics Series (Taylor & Francis, 1971).

[91] D. Griffiths, *Introduction to Quantum Mechanics*, Pearson International Edition (Pearson Prentice Hall, 2005).

[92] A. V. Oppenheim, A. S. Willsky, and S. H. Nawab, *Signals & Systems* (Prentice-Hall, Inc., Upper Saddle River, NJ, USA, 1996).

[93] G. Agrawal, *Nonlinear Fiber Optics*, Optics and Photonics (Elsevier Science, 2013).

[94] “Corning® SMF-28® Ultra Optical Fiber,” (2014).

[95] K. O. Hill, Y. Fujii, D. C. Johnson, and B. S. Kawasaki, “Photosensitivity in optical fiber waveguides: Application to reflection filter fabrication,” Applied Physics Letters **32**, 647–649 (1978).

[96] R. Kashyap, *Fiber Bragg Gratings* (Elsevier, 1999).

[97] C.-H. Wang, L. R. Chen, and P. W. E. Smith, “Analysis of chirped-sampled and sampled-chirped fiber Bragg gratings,” Applied Optics **41**, 1654 (2002).

[98] B. Kolner, “Space-time duality and the theory of temporal imaging,” IEEE Journal of Quantum Electronics **30**, 1951–1963 (Aug./1994).

[99] B. H. Kolner and M. Nazarathy, “Temporal imaging with a time lens,” Optics Letters **14**, 630 (1989).

[100] R. W. Boyd, *Nonlinear Optics* (Elsevier, 2003).

[101] B. Saleh and M. Teich, *Fundamentals of Photonics*, Wiley Series in Pure and Applied Optics (Wiley, 2007).

[102] E. Treacy, “Optical pulse compression with diffraction gratings,” IEEE Journal of Quantum Electronics **5**, 454–458 (1969).

[103] M. Karpiński, M. Jachura, L. J. Wright, and B. J. Smith, "Bandwidth manipulation of quantum light by an electro-optic time lens," Nature Photonics **11**, 53–57 (2017).

[104] M. T. Kauffman, W. C. Banyai, A. A. Godil, and D. M. Bloom, "Time-to-frequency converter for measuring picosecond optical pulses," Applied Physics Letters **64**, 270–272 (1994).

[105] J. Azaña, "Time-to-frequency conversion using a single time lens," Optics Communications **217**, 205–209 (2003).

[106] J. Azaña, N. K. Berger, B. Levit, and B. Fischer, "Spectral Fraunhofer regime: Time-to-frequency conversion by the action of a single time lens on an optical pulse," Applied Optics **43**, 483 (2004).

[107] C. R. Fernández-Pousa, "Temporal resolution limits of time-to-frequency transformations," Optics Letters **31**, 3049 (2006).

[108] T. Jannson, "Real-time Fourier transformation in dispersive optical fibers," Optics Letters **8**, 232 (1983).

[109] M. A. Muriel, J. Azaña, and A. Carballar, "Real-time Fourier transformer based on fiber gratings," Optics Letters **24**, 1 (1999).

[110] J. Azaña, "Real-Time Optical Spectrum Analysis Based on the Time–Space Duality in Chirped Fiber Gratings," IEEE JOURNAL OF QUANTUM ELECTRONICS **36**, 10 (2000).

[111] H. Talbot, "LXXVI. Facts relating to optical science. No. IV," The London, Edinburgh, and Dublin Philosophical Magazine and Journal of Science **9**, 401–407 (1836).

[112] T. Jannson and J. Jannson, "Temporal self-imaging effect in single-mode fibers," Journal of the Optical Society of America **71**, 1373 (1981).

[113] J. Azaña and M. A. Muriel, "Temporal Talbot effect in fiber gratings and its applications," Applied Optics **38**, 6700 (1999).

[114] J. Azaña and M. Muriel, "Temporal self-imaging effects: Theory and application for multiplying pulse repetition rates," IEEE Journal of Selected Topics in Quantum Electronics **7**, 728–744 (July-Sept./2001).

[115] J. Azaña, "Spectral Talbot phenomena of frequency combs induced by cross-phase modulation in optical fibers," Optics Letters **30**, 227 (2005).

[116] J. Azaña and H. Guillet de Chatellus, "Angular Talbot effect," Physical Review Letters **112** (2014).

[117] J. M. Kim, I. H. Cho, S. Y. Lee *et al.*, "Observation of the Talbot effect using broadband hard x-ray beam," Optics Express **18**, 24975 (2010).

[118] A. W. Lohmann, "An array illuminator based on the Talbot-effect," Optik **79**, 41–45 (1988).

[119] D. Pudo, M. Depa, and L. R. Chen, "Single and Multiwavelength All-Optical Clock Recovery in Single-Mode Fiber Using the Temporal Talbot Effect," Journal of Lightwave Technology **25**, 2898–2903 (2007).

[120] A. Malacarne and J. Azaña, “Analysis of amplitude fluctuation and timing jitter performance of spectrally periodic Talbot filters for optical pulse rate multiplication,” Optics Express **19**, 15339 (2011).

[121] L. Chen and D. Pudo, “Simple estimation of pulse amplitude noise and timing jitter evolution through the temporal Talbot effect,” Optics Express **15**, 6351 (2007).

[122] D. Pudo, C. R. Fernandez-Pousa, and L. R. Chen, “Timing Jitter Transfer Function in the Temporal Talbot Effect,” IEEE Photonics Technology Letters **20**, 496–498 (2008).

[123] C. R. Fernández-Pousa, F. Mateos, L. Chantada *et al.*, “Timing jitter smoothing by Talbot effect I Variance,” Journal of the Optical Society of America B **21**, 1170 (2004).

[124] C. R. Fernández-Pousa, F. Mateos, L. Chantada *et al.*, “Timing jitter smoothing by Talbot effect II Intensity spectrum,” Journal of the Optical Society of America B **22**, 753 (2005).

[125] P. A. Andrekson, “Linear propagation of optical picosecond pulse trains over oceanic distances,” Optics Letters **18**, 1621 (1993).

[126] S. Matsutani and Y. Ônishi, “Wave-Particle Complementarity and Reciprocity of Gauss Sums on Talbot Effects,” arXiv:math-ph/0207011 (2002).

[127] G. Forte, A. Lencina, M. Tebaldi, and N. Bolognini, “Self-imaging by a volume grating,” Optics Communications **284**, 2494–2499 (2011).

[128] J. L. Hall, “Nobel Lecture: Defining and measuring optical frequencies,” Reviews of Modern Physics **78**, 1279–1295 (2006).

[129] I. Coddington, N. Newbury, and W. Swann, “Dual-comb spectroscopy,” Optica **3**, 414 (2016).

[130] S. A. Diddams, L. Hollberg, and V. Mbele, “Molecular fingerprinting with the resolved modes of a femtosecond laser frequency comb,” Nature **445**, 627–630 (2007).

[131] T. Steinmetz, T. Wilken, C. Araujo-Hauck *et al.*, “Laser Frequency Combs for Astronomical Observations,” Science **321**, 1335–1337 (2008).

[132] J. Pfeifle, V. Brasch, M. Lauermann *et al.*, “Coherent terabit communications with microresonator Kerr frequency combs,” Nature Photonics **8**, 375–380 (2014).

[133] M. Kues, C. Reimer, J. M. Lukens *et al.*, “Quantum optical microcombs,” Nature Photonics **13**, 170–179 (2019).

[134] S. A. Diddams, “The evolving optical frequency comb [Invited],” Journal of the Optical Society of America B **27**, B51 (2010).

[135] R. Maram and J. Azaña, “Spectral self-imaging of time-periodic coherent frequency combs by parabolic cross-phase modulation,” Optics Express **21**, 28824 (2013).

[136] J. Caraquitena, M. Beltrán, R. Llorente, J. Martí, and M. A. Muriel, “Spectral self-imaging effect by time-domain multilevel phase modulation of a periodic pulse train,” Optics Letters **36**, 858 (2011).

[137] L. Romero Cortés, H. Guillet de Chatellus, and J. Azaña, “On the generality of the Talbot condition for inducing self-imaging effects on periodic objects,” Optics Letters **41**, 340 (2016).

[138] J. Caraquitena, Z. Jiang, D. E. Leaird, and A. M. Weiner, "Tunable pulse repetition-rate multiplication using phase-only line-by-line pulse shaping," Optics Letters **32**, 716 (2007).

[139] C. R. Fernández-Pousa, "On the structure of quadratic Gauss sums in the Talbot effect," Journal of the Optical Society of America A **34**, 732 (2017).

[140] J. Hannay and M. Berry, "Quantization of linear maps on a torus-fresnel diffraction by a periodic grating," Physica D: Nonlinear Phenomena **1**, 267–290 (1980).

[141] M. V. BERRY, S. KLEIN, H. H. W. Physics, and B. BS, "Integer, fractional and fractal Talbot effects," 26.

[142] K. Ireland and M. Rosen, *A Classical Introduction to Modern Number Theory*, Graduate Texts in Mathematics (Springer, 1990), 2nd ed.

[143] M. R. Schroeder, *Number Theory in Science and Communication: With Applications in Cryptography, Physics, Digital Information, Computing, and Self-Similarity* (Springer, Berlin, 2009), 5th ed.

[144] J. Azaña and S. Gupta, "Complete family of periodic Talbot filters for pulse repetition rate multiplication," Optics Express **14**, 4270 (2006).

[145] R. Maram, J. Van Howe, M. Li, and J. Azaña, "Noiseless intensity amplification of repetitive signals by coherent addition using the temporal Talbot effect," Nature Communications **5** (2014).

[146] H. G. de Chatellus, L. R. Cortés, and J. Azaña, "Passive amplification of periodic 2D images through self-imaging," in *Imaging and Applied Optics 2016* (OSA, Heidelberg, 2016), MW1G.2.

[147] L. Romero Cortés, A. Deville, M. Seghilani *et al.*, "Enhanced restoration of faulty images by Talbot amplification," in *Imaging and Applied Optics 2017 (3D, AIO, COSI, IS, MATH, pcAOP)* (OSA, San Francisco, California, 2017), IW4E.2.

[148] L. Romero Cortés, R. Maram, H. Guillet de Chatellus, and J. Azaña, "Subnoise Detection and Passive Amplification of Frequency Combs through Customized Coherent Spectral Energy Redistribution," Physical Review Applied **9** (2018).

[149] C. R. Fernández-Pousa, R. Maram, and J. Azaña, "CW-to-pulse conversion using temporal Talbot array illuminators," Optics Letters **42**, 2427 (2017).

[150] J. M. Lukens, D. E. Leaird, and A. M. Weiner, "A temporal cloak at telecommunication data rate," Nature **498**, 205–208 (2013).

[151] L. Romero Cortés, M. Seghilani, R. Maram, and J. Azaña, "Full-field broadband invisibility through reversible wave frequency-spectrum control," Optica **5**, 779 (2018).

[152] A. W. Lohmann and J. A. Thomas, "Making an array illuminator based on the Talbot effect," Applied Optics **29**, 4337 (1990).

[153] L. M. Sanchez-Brea and F. J. Torcal-Milla, "Near-field diffraction of gratings with surface defects," Applied Optics **49**, 2190 (2010).

[154] Y. Lu, C. Zhou, and H. Luo, "Talbot effect of a grating with different kinds of flaws," Journal of the Optical Society of America A **22**, 2662 (2005).

[155] L. Romero Cortés, R. Maram, and J. Azaña, "Fractional averaging of repetitive waveforms induced by self-imaging effects," Physical Review A **92** (2015).

[156] R. Maram, L. Romero Cortés, J. van Howe, and J. Azaña, "Energy-Preserving Arbitrary Repetition-Rate Control of Periodic Pulse Trains Using Temporal Talbot Effects," Journal of Lightwave Technology **35**, 658–668 (2017).

[157] J. Nuño, C. Finot, and J. Fatome, "Linear sampling and magnification technique based on phase modulators and dispersive elements: The temporal lenticular lens," Optical Fiber Technology **36**, 125–129 (2017).

[158] J. Nuño, M. Gilles, M. Guasoni, C. Finot, and J. Fatome, "All-optical sampling and magnification based on XPM-induced focusing," Optics Express **24**, 24921 (2016).

[159] J. Nuño, M. Gilles, M. Guasoni *et al.*, "40 GHz pulse source based on cross-phase modulation-induced focusing in normally dispersive optical fibers," Optics Letters **41**, 1110 (2016).

[160] T. T. Ng, J. L. Blows, M. Rochette *et al.*, "In-band OSNR and chromatic dispersion monitoring using a fibre optical parametric amplifier," Optics Express **13**, 5542 (2005).

[161] D. Kilper, R. Bach, D. Blumenthal *et al.*, "Optical Performance Monitoring," Journal of Lightwave Technology **22**, 294–304 (2004).

[162] J. Benesty, J. Chen, and Y. Huang, "On the Importance of the Pearson Correlation Coefficient in Noise Reduction," IEEE Transactions on Audio, Speech, and Language Processing **16**, 757–765 (2008).

[163] "Optical Frequency Combs | Menlo Systems," https://www.menlosystems.com/products/optical-frequency-combs/.

[164] C. Wang, M. Zhang, X. Chen *et al.*, "Integrated lithium niobate electro-optic modulators operating at CMOS-compatible voltages," Nature **562**, 101–104 (2018).

[165] C. Madsen, G. Lenz, A. Bruce *et al.*, "Integrated all-pass filters for tunable dispersion and dispersion slope compensation," IEEE Photonics Technology Letters **11**, 1623–1625 (1999).

[166] B. Eggleton, A. Ahuja, P. Westbrook *et al.*, "Integrated tunable fiber gratings for dispersion management in high-bit rate systems," Journal of Lightwave Technology **18**, 1418–1432 (2000).

[167] J. O. Kjellman, R. Stabile, and K. A. Williams, "Broadband Giant Group Velocity Dispersion in Asymmetric InP Dual Layer, Dual Width Waveguides," Journal of Lightwave Technology **35**, 3791–3800 (2017).

[168] Z. Jiang, D. E. Leaird, and A. M. Weiner, "Line-by-line pulse shaping control for optical arbitrary waveform generation," 9 (2005).

[169] J. Azaña, L. K. Oxenløwe, E. Palushani *et al.*, "In-Fiber Subpicosecond Pulse Shaping for Nonlinear Optical Telecommunication Data Processing at 640 Gbit/s," International Journal of Optics **2012**, 1–16 (2012).

[170] Z. Jiang, C.-B. Huang, D. E. Leaird, and A. M. Weiner, "Spectral line-by-line pulse shaping for optical arbitrary pulse-train generation," Journal of the Optical Society of America B **24**, 2124 (2007).

[171] J. M. Lukens, O. Odele, C. Langrock *et al.*, "Generation of biphoton correlation trains through spectral filtering," Optics Express **22**, 9585–9596 (2014).

[172] Q. Xie, H. Zhang, and C. Shu, "Programmable Schemes on Temporal Waveform Processing of Optical Pulse Trains," Journal of Lightwave Technology 1–1 (2019).

[173] R. H. Hadfield, "Single-photon detectors for optical quantum information applications," Nature Photonics **3**, 696–705 (2009).

[174] M. A. Nielsen and I. L. Chuang, *Quantum Computation and Quantum Information* (Cambridge University Press, Cambridge, 2010), 10th ed.

[175] C. Reimer, S. Sciara, P. Roztocki *et al.*, "High-dimensional one-way quantum processing implemented on d-level cluster states," Nature Physics (2018).

[176] H.-K. Lo, M. Curty, and K. Tamaki, "Secure quantum key distribution," Nature Photonics **8**, 595–604 (2014).

[177] Y. Zheng, H. Yang, H. Wang *et al.*, "Fluorescence-guided surgery in cancer treatment: Current status and future perspectives," Annals of Translational Medicine **7** (2019).

[178] F. Mettler and M. Guiberteau, *Essentials of Nuclear Medicine Imaging E-Book* (Elsevier Health Sciences, 2011).

[179] E. Roncali and S. R. Cherry, "Application of Silicon Photomultipliers to Positron Emission Tomography," Annals of Biomedical Engineering **39**, 1358–1377 (2011).

[180] A. T. Eggebrecht, S. L. Ferradal, A. Robichaux-Viehoever *et al.*, "Mapping distributed brain function and networks with diffuse optical tomography," Nature Photonics **8**, 448–454 (2014).

[181] J. Hecht, "Lidar for Self-Driving Cars," Optics and Photonics News **29**, 26–33 (2018).

[182] C. Wu, W. Xing, L. Xia, H. Huang, and C. Xu, "Receiver performance characteristics of single-photon lidar in a strong background environment," Applied Optics **58**, 102 (2019).

[183] A. Kirmani, D. Venkatraman, D. Shin *et al.*, "First-Photon Imaging," Science **343**, 58–61 (2014).

[184] G. Buller and A. Wallace, "Ranging and Three-Dimensional Imaging Using Time-Correlated Single-Photon Counting and Point-by-Point Acquisition," IEEE Journal of Selected Topics in Quantum Electronics **13**, 1006–1015 (2007).

[185] M. A. Albota, R. M. Heinrichs, D. G. Kocher *et al.*, "Three-dimensional imaging laser radar with a photon-counting avalanche photodiode array and microchip laser," Applied Optics **41**, 7671 (2002).

[186] J. S. Massa, A. M. Wallace, G. S. Buller, S. J. Fancey, and A. C. Walker, "Laser depth measurement based on time-correlated single-photon counting," Optics Letters **22**, 543 (1997).

[187] A. Swatantran, H. Tang, T. Barrett, P. DeCola, and R. Dubayah, "Rapid, High-Resolution Forest Structure and Terrain Mapping over Large Areas using Single Photon Lidar," Scientific Reports **6** (2016).

[188] M. Buttafava, J. Zeman, A. Tosi, K. Eliceiri, and A. Velten, "Non-line-of-sight imaging using a time-gated single photon avalanche diode," Optics Express **23**, 20997 (2015).

[189] B. R. Masters, "Fluorescence Lifetime Spectroscopy and Imaging: Principles and Applications in Biomedical Diagnostics," Journal of Biomedical Optics **19**, 109901 (2014).

[190] D.-U. Li, J. Arlt, J. Richardson *et al.*, "Real-time fluorescence lifetime imaging system with a 32 × 32 013μm CMOS low dark-count single-photon avalanche diode array," Optics Express **18**, 10257 (2010).

[191] R. Zhang, Y. Zhang, Z. C. Dong *et al.*, "Chemical mapping of a single molecule by plasmon-enhanced Raman scattering," Nature **498**, 82–86 (2013).

[192] B. McNally, A. Singer, Z. Yu *et al.*, "Optical recognition of converted DNA nucleotides for single-molecule DNA sequencing using nanopore arrays," Nano letters **10**, 2237–2244 (2010).

[193] J. K. Adelman-McCarthy, M. A. Agüeros, S. S. Allam *et al.*, "The Sixth Data Release of the Sloan Digital Sky Survey," The Astrophysical Journal Supplement Series **175**, 297–313 (2008).

[194] N. M. Batalha, "Exploring exoplanet populations with NASA's Kepler Mission," Proceedings of the National Academy of Sciences **111**, 12647–12654 (2014).